UNIVERSITY OF OKLAHOMA

GRADUATE COLLEGE

INTEGRATED GEOPHYSICAL STUDIES OF THE FORT WORTH BASIN (TEXAS), HARNEY BASIN (OREGON), AND SNAKE RIVER PLAIN (IDAHO)

A DISSERTATION

SUBMITTED TO THE GRADUATE FACULTY

in partial fulfillment of the requirements for the

Degree of

DOCTOR OF PHILOSOPHY

By

MURARI KHATIWADA
Norman, Oklahoma
2013

INTEGRATED GEOPHYSICAL STUDIES OF THE FORT WORTH BASIN (TEXAS), HARNEY BASIN (OREGON), AND SNAKE RIVER PLAIN (IDAHO)

A DISSERTATION APPROVED FOR THE
CONOCOPHILLIPS SCHOOL OF GEOLOGY AND GEOPHYSICS

BY

_____
Dr. G. Randy Keller, Chair

_____
Dr. Kurt J. Marfurt

_____
Dr. May Yuan

_____
Dr. Jamie Rich

_____
Dr. Benjamin J. Drenth

This dissertation is dedicated to my father, who taught me the value of determination towards achieving goals, to my mother for teaching me the essence of hard work and to my beloved wife for her endless support and selflessness during this study.

Acknowledgements

I would like to express my deepest gratitude to my supervisor Dr. G. Randy Keller, Professor in geology and geophysics department, University of Oklahoma and Director, the Oklahoma Geological Survey. Without, your suggestions, guidance, and unwavering continuous support during these four years, this work would not have come to this form. Thank you for believing in me during this research and continuously funding me during these years. The knowledge and motivation you shared will be lifetime tonics for me. My sincere thanks go to Dr. Kurt J. Marfurt for his invaluable guidance and suggestions during my PhD. I would also like to thank my committee members Dr. May Yuan, Dr. Jamie Rich, Dr. Benjamin J. Drenth, and Dr. Deepak Devegowda for their continuous support and cooperation.

Many thank to Marathon Oil Company for providing 3D seismic data for the Fort Worth Basin. USGS, PACES, and EarthScope EARS were the free online data resources. Without these data, this dissertation would never exist. Special thanks to Dr. Hersh Gilbert for making receiver function data available of the western US. I used FMTOMO package by Dr. Nick Rawlinson for tomographic modeling. He also helped to interpret some tomographic result and provided with extra codes that helped in the tomographic inversion process. I am cordially thankful to him.

I am much obliged to NSF and ConocoPhillips School of Geology and Geophysics (CPSGG) for the funding. SEG, Anadarko Petroleum, ConocoPhillips, OU, Geological Society of Oklahoma City, Aubra Tilley, Charles C. McBurney, and Cleo Cross provided personal scholarships during these years. Many thanks to BP America

for giving me chance to gain hand on experiences through summer internship opportunity. I am also thankful to CPSGG staffs for their support and guidance.

I am grateful to Dr. Kevin Crain, Dr. Tim Kwiatkowski, Stephan Holloway, and Galen Kaip for all sorts of technical supports as well as help during field works. Special thanks go to Dr. Vikram Jairam for helping collecting gravity data in the field and helping me run MATLAB codes and tide correction programs. I appreciate the time and help form my colleagues Xiao Xu, Christopher Toth, Atish Roy, Nabanita Gupta, Hamed Alrefaee, Jon Buening and Jefferson Chang while running different software, and proofreading my writing.

I would like to thank Jefferson, Gaurang, Rachel, Sam, Vikram, Steve, Kevin, Travis, Mark, Nick, and Calvin for their help in collecting gravity data in Oregon. Dr. Spencer Wood and Lee Liberty from Boise State University were helpful during the fieldwork in Idaho.

I owe my deepest gratitude and heartfelt devotion to my family. Thank you to my father, mother, and all family members for those long distant calls and chats during these years. Though you reside thousands of miles away from me, you and your prayers have always shown me a right path towards the progress.

Last but not the least, to my dearest wife Yamuna and lovely daughter Khusi, without your support, patience, diligence, smiles, and endless love, that has filled my life with joy, this work would have been incomplete. Words will not be enough to express my feeling towards you. I owe this dissertation to you.

Table of Contents

List of Tables

Chapter 2: Integrated geophysical imaging of the upper crustal features in the Harney Basin, southeast Oregon

List of Figures

Chapter 1: A window into the Proterozoic: integrating 3D seismic, gravity, and magnetic data to image sub-basement structures in the southeast Fort Worth Basin

Abstract

Geophysical methods such as seismic, gravity, magnetics, electric, and electromagnetics are capable of identifying subsurface features but each has a different spatial resolution. Although, each of these methods are stand-alone tools and have produced wonderful and reliable results for decades to solve geological problems, integrating geophysical results from these different methods with geological and geospatial data, adds an extra dimension towards solving geological problems. Integration techniques also involve comparing and contrasting the structural and tectonic evolution of geological features from different tectonic and geographic provinces. I employed 3D and 2D seismic data, passive seismic data, and gravity and magnetic data in three studies and integrated these results with geological, and geospatial data. Seismic processing, and interpretation, as well as filtering techniques applied to the potential filed data produced many insightful results. Integrated forward models played an important role in the interpretation process.

The three chapters in this dissertation are stand-alone separate scientific papers. Each of these chapters used integrated geophysical methods to identify the subsurface features and tectonic evolution of the study areas. The study areas lie in the southeast Fort Worth Basin, Texas, Harney Basin, Oregon, and Snake River Plain, Idaho.

The Fort Worth Basin is one of the most fully developed shale gas fields in North America. With the shallow Barnett Shale play in place, the Precambrian basement remains largely unknown in many places with limited published work on the basement structures underlying the Lower Paleozoic strata. In this research, I show how the basement structures relate to overlying Paleozoic reservoirs in the Barnett Shale and

Ellenburger Group. I used high quality, wide-azimuth, 3D seismic data near the southeast fringe of the Fort Worth Basin. The seismic results were integrated with gravity, magnetic, well log, and geospatial data to understand the basement and sub-basement structures in the study area. Major tectonic features including the Ouachita thrust-fold belt, Lampasas arch, Llano uplift, and Bend arch surround the southeast Fort Worth Basin. The effects of these tectonic units in the basement were imaged in form of faulted and folded basement and sub-basement layers. Euler deconvolution and integrated forward gravity modeling were employed to extend the interpretations beyond the 3D seismic survey into a regional context.

The Harney Basin is a relatively flat lying depression in the northeast portion of the enigmatic High Lava Plains volcanic province in eastern Oregon. In addition to the High Lava Plains active source seismic data, I also employed gravity, magnetic, digital elevation, geologic maps, and other geospatial data in this integrated study. I generated an upper crustal 3D seismic tomographic model of the Harney Basin and surrounding area using the active source seismic data. I then integrated it with gravity, magnetic, and geologic data to produce a geophysical model of the upper crustal structure, which reveals that the basin reaches as deep as 6 km in the central areas. I observed two major caldera shaped features within the basin. These calderas reveal seismic low velocity areas along with low gravity and magnetic anomalies. I interpreted the extent of these calderas with the help of integrated geophysical results. I propose a nested caldera complex in the northern Harney Basin and another caldera in the southern part.

The Snake River Plain is an arcuate-shaped topographic low that lies in southern Idaho. This rifted valley is filled by large volume of mafic magma with numerous

exposures of silicic volcanic centers. The scientific discussion on the structural complexities and evolution of the Snake River Plain and the role of extension in its formation has been going on for decades. Similarly, high gravity and magnetic anomalies are associated with the Snake River Plains, and their possible causes are still the subject of many studies. Numerous recent passive seismic studies specifically focus on the deep mantle structures of the Eastern Snake River Plain. However, crustal scale studies in the Western Snake River Plains are limited. In this research, I used gravity and magnetic data in the area and integrated the results with seismic, geospatial data, and receiver function results. I identified the major differences and similarities in the structures and tectonics of the Western and Eastern Snake River Plain based on the gravity and magnetic anomalies. With the help of processed receiver function results, 2D seismic refraction and reflection data, interpreted well logs, and geospatial data, I generated 2D gravity models across the Western Snake River Plain. A mid-crustal mafic intrusion is the main reason for high gravity anomaly in the Western Snake River plain. Alternate gravity model along a profile showed underplating as a possible additional source for the gravity high along the Western Snake River Plain.

Introduction

Scientists have used geophysical methods to solve geological problems for centuries. Geophysical methods are generally scale independent. In this dissertation, I used 2D and 3D active seismic, passive seismic, gravity and magnetic data and integrated the results with well log data, geological maps, and digital elevation data to study subsurface features. Three different areas in different tectonic provinces in the United States were chosen, which are: the southeast Fort Worth Basin, Texas, the Harney Basin, Oregon, and the Snake River Plain, Idaho. In the Fort Worth Basin, I studied the shallow reservoirs and tectonic setting of the Barnett Shale and its relation to the underlying basement. In the Harney Basin and Snake River Plain, my studies primarily focused on upper to deep crustal structures and tectonic evolution of these areas. The main aims of this study are to integrate available geophysical datasets with geological data and to identify the tectonic and structural features of the subsurface of the study areas and their tectonic evolution.

This dissertation includes three different chapters, and each chapter is a stand-alone scientific paper. These chapters are at different stages of publication. Chapter 1 on the southeast Fort Worth Basin has been accepted for publication by the Interpretation Journal of the Society of Exploration geophysicists. Chapter 2 on the Harney Basin is almost ready to submit to Geosphere that is published by the Geological Society of America. Chapter 3 on the Snake River Plain will also be submitted to Geosphere and is currently in preparation.

Chapter 1: A window into the Proterozoic: integrating 3D seismic, gravity, and magnetic data to image sub-basement structures in the southeast Fort Worth Basin

Abstract: The Fort Worth Basin is one of the most fully developed shale gas fields in North America. Although there are hundreds of drilled wells in the basin, almost none of them reach to the Precambrian basement. Imaged by perhaps one hundred 3D seismic surveys, the focus on the relatively shallow, flat-lying Barnett Shale objective has resulted in little published work on the basement structures underlying the Lower Paleozoic strata. Subtle folds and systems of large joints are present in almost all 3D seismic surveys in the Fort Worth Basin. At the Cambro-Ordovician Ellenburger level, these joints are often diagenetically altered and exhibit collapse features at their intersections. In this research, we show how the basement structures relate to overlying Paleozoic reservoirs in the Barnett Shale and Ellenburger Group. In support of our investigation, the Marathon Oil Company provided a high quality, wide-azimuth, 3D seismic data near the southeast fringe of the Fort Worth Basin. In addition to the seismic volume, we integrated the seismic results with gravity, magnetic, well log, and geospatial data to understand the basement and sub-basement structures in the southeast Fort Worth Basin. Major tectonic features including the Ouachita thrust-fold belt, Lampasas arch, Llano uplift, and Bend arch surround the southeast Fort Worth Basin. Euler deconvolution and integrated forward gravity modeling helped us extend our interpretation beyond the 3D seismic survey into a regional context.

Keywords: *geophysical integration, 3D seismic, gravity, magnetic, basement, Euler deconvolution*

Introduction

The Fort Worth Basin (FWB) is a Late Paleozoic foreland basin that is associated with the Ouachita orogenic belt (OOB) and occupies an estimated area of about 15000 sq. miles (~38000 km^2) (Montgomery et al., 2005; Pollastro et al., 2007; Bruner and Smosna, 2011). Major tectonic units that bound the Fort Worth Basin include the Muenster arch that is related to the Southern Oklahoma aulacogen (SOA), the Llano uplift (LU), the Ouachita thrust-fold belt (OTFB), and the Bend arch (Fig. 1.1). The FWB was primarily developed during the Early and Middle Pennsylvanian in front of the advancing Ouachita fold belt (Walper, 1982; Kruger and Keller, 1986; Pollastro et al., 2007).

Tectonic studies of the FWB and its surrounding regions, such as the OOB, and the LU, dates back as early as 1857 (Viele, 1989). Flawn (1961) published a notable summary about the geological and tectonic history of the entire OOB. After the emergence of plate tectonics, studies of the region escalated and numerous regional analyses of the tectonic and geological evolution of the Ouachita system were undertaken (e.g., Nicholas and Rozendal, 1975; Kruger and Keller, 1986; Arbenz, 1989, 2008; Denison, 1989; Keller et al., 1989; Nicholas and Waddell, 1989; Viele 1989; Viele and Thomas, 1989). The Llano uplift (LU) is important because it is the only Precambrian basement outcrop in the region; studies of its structure and evolution include Carter (1989), Mosher et al., (2008), Barker and Reed (2010), Levine and Mosher (2010). Regional geophysical studies of the FWB region include Nicholas and

Rozendal (1975) who employed 2D seismic, gravity, and geological data to interpret the subsurface structures within the Ouachita fold belt and their relation to the Paleozoic cratonic margin. Kruger and Keller (1986) used gravity, drilling, and geologic data to study the crustal structure of Ouachita Mountains and FWB region. The crustal scale structure of the region was synthesized by Mickus and Keller (1992) who used 2D seismic refraction and reflection profiles from COCORP and PASSCAL scientific experiments, well data, and gravity data to interpret the lithospheric structure of the Ouachita frontal thrust belt (OFTB) across the Gulf coastal plain, to the Gulf of Mexico.

The geological framework, history, and tectonic evolution of the FWB is discussed in many publications such as Henry (1982), Walper (1982), Meckel et al. (1992), Thomas and Texas (2003), Erlich and Coleman (2005), Montgomery et al. (2005), Loucks and Ruppel (2007), Pollastro et al. (2007), and Bruner and Smosna (2011). Hardage et al. (1996) used 3D seismic data to study the relationships between the karst and collapse features and overlying clastic stratigraphy. Since these study, potential field data, drilling results, and volumetric seismic attributes such as dip and azimuth, curvature, coherence, and reflector parallelism of convergence are widely used to identify and interpret small to mega scale structural features in the subsurface and their relation to the bounding rock units. For example, Sullivan et al. (2006) successfully employed volumetric seismic attributes such as curvature, coherence, and reflector rotation to map chimneys, collapse, and karst features of the Ellenburger Group in the FWB and showed that these features are controlled by tectonic processes. Aktepe et al. (2008) used volumetric attributes such as coherence and curvature to map and analyze basement faulting and showed their involvement with the observed collapse

features in the Paleozoic strata above the basement. Elebiju et al. (2010) used volumetric seismic attributes and high-resolution aeromagnetic data to successfully establish links between the Precambrian basement structure and sedimentary structures of overlying Paleozoic strata in the northern part of FWB.

Most of the recent geophysical studies in the FWB are focused on the northern part because of the presence of thicker Barnett Shale and other oil and gas bearing carbonate units. Geophysical studies and published works in the southern FWB are limited because of the reduced thickness of the Barnett Shale and absence of the key Paleozoic carbonate units such as the Viola, Simpson, and Forrestberg Limestone (Montgomery et al., 2005; Pollastro et al., 2007; Bruner and Smosna, 2011). Although there are hundreds of oil and gas exploration and production wells, most are focused on the shallow Barnett Shale production such that we lack well data below the Cambro-Ordovician Ellenburger Group. There is even less data and fewer published studies on the basement structures of the southern FWB.

This study is focused on the data sparse southern Fort Worth Basin, where Marathon Oil Company collected 3D seismic data in a small area of Hamilton County, Texas in 2006 (Fig. 1.1). We used these 3D seismic data to identify and interpret basement and sub-basement structures and their relationship with the overlying Paleozoic and Late-Paleozoic sequences. We augmented this proprietary data volume with publically available gravity, magnetic, and geospatial data. We integrated the results obtained from these geophysical methods to understand the details of the Precambrian basement in the southeast FWB. We also constructed an integrated forward gravity model across the FWB and OFTB and performed Euler deconvolution

of the magnetic data. Afterwards, we integrated the results to interpret the tectonic and structural history of the basement and its relationship with the overlying basin.

Geological and tectonic background

The Phanerozoic evolution of the area started with Early Paleozoic continental rifting in the context of a Wilson Cycle that formed the SOA and the Early and Middle Paleozoic continental margin along which the OOB developed in the Late Paleozoic (e.g., Keller, 2009). The FWB was part of the southern Laurentian passive margin when Laurentia collided with Gondwana in the Mid Paleozoic (Dalziel et al., 1994; and Dennie, 2010). The Paleozoic Ellenburger Group, Simpson Group, and Viola Limestone lie beneath a major unconformity and are overlain by the Forrestberg Limestone, Barnett Shale, and Marble Falls Limestone Group. Pennsylvanian strata subsequently filled the Fort Worth Basin. Today, Proterozoic rocks are exposed in the Llano uplift area. The west and northwest portions of the FWB are covered with the Paleozoic rocks whereas the OOB, eastern FWB, and the GCP (Gulf Coastal Plain) are all covered with Cretaceous and Quaternary sediments (Fig. 1.1). Walper (1982) interpreted some high angle normal faults and graben structures in the FWB mostly associated with the Ouachita orogenic fold-thrust belt and the Llano uplift. Some of these faults are exposed, but most of them are buried under the Quaternary sediments.

The FWB is bounded on the east by the OOB, which is the most prominent structure in the periphery of the basin and forms the approximate boundary between the transitional crust of the Gulf of Mexico and the cratonal North America (e.g. Kruger and Keller, 1986; Keller et al., 1989; Gao et al., 2008). The Ouachita Mountains have limited exposure in Texas and are buried beneath the younger Cretaceous and

Quaternary sediments (e.g. Keller and Cebull, 1973; Keller et al., 1989; Viele, 1989; Viele and Thomas, 1989). The Ouachita orogeny started in the Late Paleozoic when a southern continent collided with North America; the tectonic activity migrated westward and ended by the Early Permian (Keller and Hatcher, 1999; Kruger and Keller, 1986). The inboard side (side toward the FWB) of the OFTB contains unmetamorphosed to slightly metamorphosed pre-orogenic offshore and syn-orogenic deep-water rocks, whereas the outboard side contains higher-grade metamorphic rocks (Flawn, 1961; and Viele, 1989). The north border of the basin, the Muenster arch, is a fault bounded basin uplift related to the SOA, which was reactivated during the Ouachita orogenic compression (Walper, 1982; Keller et al., 1989; Pollastro et al., 2007; Elebiju et al., 2010). The FWB is bounded by the Bend arch in the west. that is a subsurface structural high that extends north of the LU. In the Late Mississippian, the FWB subsided and tilted westward, which is one of the reasons for the formation of the Bend arch (Tai, 1979; Walper, 1982; Pollastro et al., 2007). The FWB is terminated on the south by the LU, which is a dome shaped structural feature that exposes Mesoproterozoic-Paleozoic rocks (Montgomery et al., 2005; Pollastro et al., 2007; Mosher et al., 2008). The rocks in the northeast portion of the LU are deformed and metamorphosed with many NE-SW trending normal faults related to the Ouachita orogenic event (Smith, 2004; Mosher et al., 2008). The Lampasas arch is another prominent structure in the southern FWB that extends northeast from the LU and follows the orientation of other major faults related to the Ouachita frontal zone (Pollastro et al., 2007). In addition to these major structures, many basement related normal faults, thrust faults, fractures, karst, and collapse features are abundantly found

in the Cambrian to Pennsylvanian units throughout the FWB. These structures relate to multiphase tectonic events. Some of these structures were reactivated in the north and northeast part of the basin, however, the direction and orientation of these structures changes rapidly from place to place (Flawn, 1961; Henry, 1982; Pollastro et al., 2003; Montgomery et al., 2005; Pollastro et al., 2007). Due to these different tectonic events, the FWB formed as an asymmetrical and wedge-shaped basin that pinches out toward the south (Figure 1.1).

General stratigraphy

The generalized stratigraphy of the FWB is shown in Figure 1.2. The basement of the FWB is made up of structurally complex Precambrian meta-sediments, granite, diorite, gneiss, and schist (Preston et al., 1996; Pollastro et al., 2003). However, in most of the cases, no well data penetrate below the Ellenburger Group. Above the basement, unconformably lie the Cambrian rocks of Wilberns and Riley Formations (Denison, 1989). The Riley Formation consists of the oldest Hickory Sandstone Member, Cap Mountain Limestone Member, and the youngest Lion Mountain Sandstone Member, whereas, the Wilberns Formation is made up of (from oldest to youngest) the Welge Sandstone Member, Morgan Creek Limestone Member, Point Peak Member, and San Saba Limestone Member (Fig. 1.2). These rocks were deposited in shallow marine environments, which were often sub-aerially exposed (Preston et al., 1996; and Smith, 2004). Their thickness ranges from about few meters to 915 m (~3000 ft) in the south and southeast area near the Llano uplift (Preston et al., 1996; Smith, 2004; Pollastro et al., 2007). The Cambro-Ordovician Ellenburger Group conformably overlay the Wilberns Formation. It predominantly consists of porous dolomite and limestone with

abundant chert and occasional sandstone units. These rocks are characterized by numerous karst, solution-collapse, and brecciated structures (e.g. Loucks, 2003; Montgomery et al., 2005; Sullivan et al., 2006; Loucks and Ruppel, 2007; Dennie, 2010). In the central part of the FWB, basement faults have influenced the Ellenburger sub aerial karst features, and these features have helped to reactivate the faults (Sullivan et al., 2006). Above the Ellenburger Group, the Middle and Upper Ordovician Simpson Group, Forrestberg Limestone, and Viola Limestone were deposited, but these units are absent on the southeast area (Bruner and Smosna, 2011). In the south and southeast area, the Mississippian Barnett Shale unconformably overlays the Cambro-Ordovician Ellenburger Group (Pollastro et al., 2003; Montgomery et al., 2005; Dennie, 2010; Bruner and Smosna, 2011). The absence of the Devonian and Silurian rocks indicates an erosional surface (unconformity) above the Ellenburger Group. The thickness of the Barnett Shale varies across the basin. It is as thick as 213 m (~700 ft) in the northeast corner whereas the thickness decreases to about 9 m (~30 ft) in the south and southeast corner (Montgomery et al., 2005; Loucks and Ruppel, 2007; and Bruner and Smosna, 2011). The Barnett Shale is overlain by the Mississippian Marble Falls Limestone, which in turn is covered with the Atokan conglomerate and sandstone (Bruner and Smosna, 2011). Above these Paleozoic units, lies a relatively thin cover of the Cretaceous and Quaternary sediments.

Geophysical data preparation, processing, and interpretation

In this study, we analyzed 3D seismic data, gravity, and aeromagnetic data and integrated the results with other geospatial data including well logs, geological maps, fault maps, and digital elevation models to interpret the basement structures. In the

following sections, we discuss the details of these methods, basics of the processing techniques, and the interpretation.

Seismic data

3D seismic data preparation:

The 3D seismic survey covered approximately 220 km^2 (~ 85 Sq. miles) and has 1189 inlines and 1119 crosslines with spacing of 16.76 m (~55 ft) each. We used the pre-stack time-migrated seismic volume for interpretation purposes. The data processing was focused on imaging the shallow Barnett Shale objective, leaving some low frequency migration artifacts in the deeper portion of the seismic data. In an ideal case, one should pre-stack depth migrate the data to image the basement. Here, we applied a bandpass Butterworth filter (10-15-24-30 Hz) to reduce the migration artifacts and higher band frequency related multiples. We picked some of the key Paleozoic horizons and faults along with some of the strongest sub-basement reflectors (Fig. 1.3). Given the flat nature of the Paleozoic section, these dipping reflectors represent geology of the area rather than multiples. These reflectors are discontinuous in places but are trackable. Below these strongest reflectors, there are various discontinuous and weaker reflectors. These reflectors truncate upward and terminate into the sub-basement reflectors. These sub-basement reflectors form bounding envelopes (Fig. 1.3). We also mapped some of the major fault patterns, which exhibit NNE-SSW trends.

Another major technique applied to the seismic data was attribute analysis. Volumetric seismic attribute analysis not only helps to delineate and identify major structural features such as faults, karst, and collapse features, but also aids visualization of dip and azimuth variations and reflector rotation. The volumetric attributes, such as

amplitude variation, coherence, curvature, dip and azimuth variation, reflector rotation, and structurally oriented filters are routinely used in the 3D seismic interpretation (Brown, 1996; Chopra and Marfurt, 2005, 2007a, b). We used an internally developed software package to generate numerous volumetric seismic attributes. Among them, coherence, curvature, reflector rotation, and dip and azimuth variation of the reflectors were the most useful in this study. The results from the volumetric attributes analysis are shown in Figures 1.4 through 1.7. The discussion of the mathematical details and theoretical background of these methods is beyond the scope of this paper, with the details found in Brown (2011), Chopra and Marfurt (2007a).

Seismic data interpretation:

Although, the seismic data covers only a small part of the study area, its spatial resolution helped to easily identify major subsurface features. We identified and mapped major faults, key Paleozoic horizons, the top of the Precambrian basement, and sub-basement reflectors in the seismic volume. Figure 1.3 shows the main structural features observed in the seismic data on a representative vertical slice through the central portion of the survey. The top of the Precambrian basement is clear throughout the seismic volume. Above the basement, Wilberns and Riley Formations were clear, and we mapped the Ellenburger Group and the Marble Falls Limestone horizons. The Barnett Shale lies between these units and thins from A towards A′ (eastward). Montgomery et al. (2005) and Bruner and Smosna (2011) discussed the absence of the Viola Limestone, Simpson Group, and the Forrestberg Limestone in the southern part of FWB. We can confirm this in the seismic section (Fig. 1.3). Four major faults namely F1, F2, F3, F4 are mapped (Fig. 1.3). These normal faults have a regional trend of

NNE-SSW. Fault F1, is shallow but has the largest offset, which is about 0.25 s. Fault F2, has a small offset of a few milliseconds. We traced this fault to a depth of about 1.4 s. Fault F3, cuts across the Paleozoic sequences as well as the Precambrian basement. This fault can be trace down to about 1.5 s. Below this depth; it is faintly visible and is shown by a dashed white line in Figure 1.3. Deep in the seismic section, we observe other potential faults (dashed white lines). We suspect these features are probably normal and thrust faults that trend NNE from the eastern LU and are most likely related to faults associated with the Ouachita orogeny (e.g. Ferrill and Morris, 2008; Mosher et al., 2008; Levine and Mosher, 2010). Fault F4, has a smaller offset and is mapped to about 1.1 s. Below 1.3 s, we also picked some strong and continuous intra-basement reflectors (denoted as sub-basement 1 and sub-basement 2 in Fig. 1.3). They are irregular, curved and truncated in 3D perspective view. The irregular shapes, truncation and curvature of the basement are the product of the complex history of Ouachita tectonics and multi-phase uplift in the Llano area that is related to Grenville orogeny and subsequent erosional unconformity (e.g. Freeman and Wilde, 1964; Mosher et al., 2008; Levine and Mosher, 2010). At about 2.0 s and below, there are more intra-basement reflectors (dashed black lines in Fig 1.3). They are discontinuous through the seismic volume and hence are more difficult to pick. We interpret these events as possible intrusive bodies, sills, and dikes mostly related to the magmatism that is observed in the eastern LU and are probably related to the Grenville orogeny.

We used different volumetric attributes to aid the seismic interpretation process including curvature, coherence, combined dip and azimuth, and reflector rotation. Co-rendering these attributes and the seismic data together is a very useful technique to

visualize subtle geological features that may not be readily observed in the traditional seismic amplitude display. Coherence attributes measure the similarity of the neighboring seismic traces along the dip and azimuth of the seismic reflectors (Chopra and Marfurt, 2007a). This attribute is a useful tool to visualize faults, river channels, reefs, karst features, and collapse features. Curvature approximates local seismic reflectors with a quadratic surface and highlights folds, flexures along the fault planes, collapse, and karst features. Figure 1.4 shows a time slice through co-rendered coherence, most positive and negative principal curvature near the approximate top of Precambrian basement with vertical slice through seismic amplitude co-rendered with the two curvatures. Blue areas (such as indicated by the cyan arrow) highlight valleys and bowls while red areas (such as indicated by the white arrow) highlight ridges and domes. Some of these valleys and ridges cut across the Barnett Shale and Ellenburger Group and extend at least to the basement. Note the complex deformation of the basement that controls the collapse features in the shallower Ellenburger Group (such as area indicated by the red and blue ellipse). In the NW corner of the survey, we also observed a pop-up block throughout the Paleozoic sequences. This indicates the presence of transpressional tectonic setting and complex deformation history. To find the vertical extent of karst and collapse features observed in the Marble Falls Limestone and Ellenburger Group, we analyzed co-rendered times slices of coherence, most-positive and negative principal curvature at different depth ranging from 0.75 s to 1.1 s and plotted them against the seismic data (Fig. 1.5). The slice at t=0.75 s approximates the top of the Ellenburger Group where we see all of the picked faults F1, F2, F3, and F4 and significant numbers of the collapse and karst features (indicated by cyan

arrows). We observe that some of these karst and collapse features align well with faults as in F2 and F3 forming a "string of pearls" as seen in other FWB surveys (Schuelke, 2011). At t=0.9 s, these collapse and karst features are not clearly visible (except in the southwest corner). At this level, we are at one of the sandstone units of the Riley or the Wilberns Formation. At t=1.0 s time slice, some of these karst and collapse features (indicated by cyan arrows) reappear in the southeast corner of the survey. We interpret this time slice as cutting to one of the limestone members of the Riley or the Wilberns Formation. At t=1.1 s, none of these karst or collapse features are visible. At this depth, we are looking into the Precambrian basement in the area, which is mainly composed of granite and diorites as shown in Figure 1.2 and reported by Smith (2004), Sullivan et al. (2006), and Bruner and Smosna (2011).

The combined dip and azimuth attributes help us identify and interpret the orientation of dipping seismic reflectors, faults, and folds. We co-rendered the combined dip and azimuth attribute and seismic amplitude values and show the result in Figure 1.6. Faults F1, F2, F3, and F4 are all observed with brighter (higher intensity/luminosity) color indicating steeper dips of about 15^0-20^0. Faults F1, F2, F3 are dipping toward the NNW, whereas F4 dips SSE. Reflector rotation is a more recently introduced attribute (Marfurt and Rich, 2010) that estimates the non-quadratic features of the local surfaces. Mathematically, the mean curvature is the divergence of the vector dip while the reflector rotation is the curl of the reflector dip. At t=0.7 s and t=1.0 s we observe strong NNE-SSW trending fabrics as shown in Figures 1.7A and 1.7B. These fabrics match well with the structural trend of Balcones fault and the thrust faults of the OOB (Fig 1.1 and 1.10). We also observed possible Reidel shear (?)

structures in between faults F1 and F2 (Fig. 1.7A). The presence of these shear zones indicates the transpressional tectonic setting in the area during the Paleozoic. We also extracted vertical slices along the arbitrary lines AA′ and BB′ and show these seismic sections in Figures 1.7C and 1.7D. We identified key Paleozoic horizons and some of the Proterozoic reflectors. These sub-basement Proterozoic reflectors are probably igneous sills and intrusions related to the Grenville orogeny similar to those observed in the nearby eastern LU (Carter, 1989; Mosher et al., 2008; Barker and Reed, 2010). There are some unidentified reflectors (marked by white block arrows; Figs. 1.7C and D). We believe these reflectors either are faults related to the Ouachita orogeny or are some meta-sedimentary or meta-volcanic Proterozoic horizons.

With the help of all these interpretations, we constructed the 3D perspective view of the time-structure map with the major basement structures, mapped faults, and key Precambrian horizons shown in Figure 1.8. The top of the Precambrian basement is relatively flat and continuous. The Proterozoic sub-basement surfaces are irregular and truncated. These surfaces resemble the shape of intrusive igneous bodies such as sills or plutons. Faults F2 and F3 are deep seated and cut across the entire Proterozoic and Paleozoic sequences in the area whereas faults F1 and F4 are shallow and are mapped in the Paleozoic sequences and in the shallower portion of the Precambrian basement.

Gravity and magnetic data

Gravity and magnetic data preparation and processing:

The terrestrial gravity and aeromagnetic data for the continental United States are freely accessible online at Pan American Center for Earth & Environmental Studies

(PACES) [http://research.utep.edu/paces/]. We downloaded the regional gravity and magnetic data for an area of about 2 degrees out on each side of the seismic survey. One of our goals is to determine if the regional potential field data relates the basement structures mapped on the seismic volume with the large scale OOB, Lampasas arch and the LU tectonic units in the study area. The regional data covers the area between 30^0N-34^0N latitudes and 95^0W-99^0W longitudes (Figs. 1.1, 1.9, and 1.11). We used complete Bouguer anomaly (CBA) gravity values from the PACES database for further mapping and processing and used the Texas state magnetic data to analyze magnetic anomalies. These latter data were collected as part of the National Uranium Resource Evaluation (NURE) program in 1973 and is freely available online at USGS website [http://pubs.usgs.gov/ds/2006/232/]. We used a 2 km (~6562 ft) grid spacing for both CBA and total magnetic intensity (TMI) grids. We also reduced the TMI data to the magnetic North pole so that the resulting residual magnetic anomalies will lie directly above the magnetic source (Blakely, 1996) unless there is a strong remanent magnetization present. This reduced-to-pole residual TMI grid was used for further processing and filtering the magnetic data. Geosoft® software was used for processing and analyzing the potential field data.

To enhance the visualization of gravity and magnetic anomalies, their shapes, and boundaries, we used various wavelength filters. We applied upward continuation filter to the CBA to estimate the regional anomalies and subtracted the result from the CBA map to obtain a residual CBA map (Fig. 1.9A). We also applied the directional derivative, tilt derivative, and total horizontal derivative filters to both the gravity and magnetic data, to delineate boundaries of intrusive bodies, faults, and other lateral

changes using edge detection techniques. The discussions of the mathematical and theoretical details of these filters are found in Miller and Singh (1994), Blakely (1996), and Verduzco et al. (2004).

In addition to the wavelength and edge detecting filters, we also applied Euler deconvolution techniques to the magnetic data to determine the depth to the basement of the magnetic anomalies. The Euler deconvolution method relates the vertical and horizontal gradients of the residual TMI values with help of geometry of the magnetic bodies given by the structural index (SI) (e.g. Thompson, 1982; and Barbosa et al., 1999). In addition to estimating basement depth, solutions obtained from the Euler deconvolution help to delineate source geometry and boundaries and can map fault if the proper SI value is used for the given fault offset depth, and location of the fault. Shallow faults with larger offsets and irregular contacts are assigned an SI value of 0, whereas deeper faults with small offsets are assigned an SI value of 1 (Reid et al., 1990). Although the solution form Euler deconvolution techniques help us to locate the anomaly of isolated magnetic bodies with the appropriate SI, solutions in areas with multiple source and complex geometry can be problematic (Blakely, 1996). In this paper, we used SI values of 0 to map deeper faults and 0.5 and 1 to map the top of the Precambrian basement.

Interpretation of gravity and magnetic data:

In a study such as this, potential field data like gravity and magnetic surveys have lower spatial resolution than seismic reflection data. However, they are very helpful for understanding regional geological and tectonic setting of the area. The CBA anomaly in the area varies by about 100 mGal. We observed major tectonic units

surrounding the FWB such as the LU, OOB, and SOA, which are associated with regional gravity highs. A prominent gravity low is associated with the FWB basin. We focused on the local area that contains the seismic data and analyzed gravity features (Fig. 1.9B). The seismic survey area lies within a series of local gravity high anomalies (G1, G2, G3; marked by dashed blue polygons, Fig. 1.9B) with a NE-SW regional trend. Two major gravity lows lie to the NW and SE sides of these features (marked by dashed red polygons).

To aid in the interpretation, a residual gravity anomaly map was constructed by subtracting the surface resulting from upward continuing the data to 40 km (Fig. 1.10). Major tectonic units are identified on this map, including the approximate boundaries of the FWB, LU, SOA and OOB interior zone. Inside the FWB, two major gravity lows are observed. To the northwest, a large linear gravity minimum is known as Abilene gravity minima (AGM). Adams and Keller (1996) interpreted its source to be potentially a Precambrian granitic batholith that is similar to the size of Sierra Nevada batholith. Northeast of the LU, another gravity minimum (G4) of similar intensity of the AGM but of smaller extent is observed. We interpret this minimum as similar to that of the AGM in its origin. We hypothesize that the encroaching Ouachita frontal thrust in the Late Paleozoic played an important role in creating elliptical shape of the gravity minimum (G4), with its longer axis parallel to the direction of the Ouachita frontal thrust zone. The analogy can be drawn from the Sudbury structure, Ontario, Canada, where the impact structure was intensely deformed by the Grenville orogeny (Boerner et al., 2000).

We also analyzed the magnetic data and a reduced-to-pole residual TMI map is shown in Figure 1.11. Magnetic highs related to the OOB and SOA are observed (shown by sets of white and yellow arrows respectively, Fig. 1.11A) Within the FWB itself, there are several magnetic bodies giving rise to interfering anomalies. The localized TMI map with a focus on the seismic survey area is shown in Figure 1.11B. Two positive local magnetic anomalies (M1 and M2) are observed in vicinity of the seismic survey. These anomalies are related to the folded and bulged structures (sub-basement 1 and sub-basement 2) shown in Figures 1.3 and 1.8, which we interpret to be igneous intrusions related to the eastern LU. We also observe a local magnetic minimum, M3 in the residual TMI map. This minimum is partly related to the thicker Cambrian sediments to the northeast side of the LU (Preston et al., 1996; and Smith, 2004) and probably partly due to the felsic intrusive bodies from the Grenville orogeny (Carter, 1989; Mosher et al., 2008; Barker and Reed, 2010; Levine and Mosher, 2010).

We modeled a 272 km (~169 mi) long residual CBA gravity profile AA′ (Fig. 1.10) across the OOB using seismic, drilling, and geologic data as constraints. The density model along the profile is shown in Figure 1.12. We chose this profile in such a way that it crosses the 3D seismic data and the most important tectonic units in the area. A few of the interpreted well logs lie in the profile but none penetrates through the shallow Ellenburger Group. The average Moho depth in the area has been estimated to be about 40 km (e.g. Kruger and Keller, 1986; Keller et al., 1989; and Gao et al., 2008). Based on this model, we interpret the Moho depth to range from about 42 km in the FWB to about 37 km in the GCP. The mantle and the lower crust were assigned typical average densities of 3.3 and 3.0 g/cm^3 respectively. At about 3 km depth, we modeled

shallow igneous body with density of 2.65 g/cm^3, which we interpret to be a granitic sill. A prominent local gravity minimum (G4) is located at the center of profile (Fig. 1.10). Some researchers have interpreted G4 to be related to thick sedimentary units of the FWB. This contradicts the well log data, which, show the top of the Ellenburger Formation in this area is rather flat (Montgomery et al., 2005; and Bruner and Smosna, 2011). To model the gravity low of G4, we took an alternative modeling approach by thickening the Cambrian units of Riley and Wilberns Formation to some extent (Preston et al., 1996) and emplacing a low-density (2.6 g/cm^3) granitic batholith in the upper crust. The density variation for granite at the given depth is as suggested by Oliver (1977) for the Sierra Nevada granites. We used seismic data, well logs, and geospatial database to constrain the upper few kilometers of the model. To determine the densities of the Paleozoic units from the seismic data, we used Gardner's empirical relation (Gardner et al., 1974) between the density and P-wave velocity. We compared and confirmed these densities with the aid of well logs in the area. In the FWB, the top of the Precambrian basement is at the depth of about 2.5 to 3.5 km (~8000 - 11500 ft.) whereas the depth of the Cambrian unit ranges between 1.4 -1.8 km (~4500 - 5800 ft.). The Ellenburger Group overlies the Cambrian units. The top of Ellenburger Group is relatively flat and is overlain by the Barnett shale and Marble Falls Limestone. Cretaceous and Quaternary sediments unconformably overlie the Paleozoic sequence. To the southeast side of G4, lies the OOB. We modeled the Ouachita frontal zone and Ouachita interior zones with densities of 2.64 and 2.71 g/cm^3. The difference in densities is based on the rock types they contain. The frontal zone mostly consists of pre-orogenic off-shelf and syn-orogenic deep-water rocks, whereas, the interior zone

mostly contains metamorphosed rocks from of the interior metamorphic belt (Viele, 1989). Our model suggests that the root of the OOB is as deep as 10 km and deepens southward which matches other estimates for the area (Kruger and Keller, 1986; Arbenz, 1989; Keller et al., 1989). Under the OOB, a mafic intrusion was also included to model prominent gravity high and may mark the Cambrian margin of North America as is indicated further to the east by Keller et al. (1989) and Mickus and Keller (1992). Further to the south lies the GCP. The magnetic anomalies across the profile are complex due to presence of the multiple magnetic sources in the basement of the area and uncertainty of the remnant magnetization values. For this reason, we did not model magnetic data. However, we compare the gravity and magnetic anomalies along profile A-A′ (Fig. 1.12).

In order to extend our mapping of the top of the basement beyond the seismic survey, we performed Euler deconvolution on the reduced-to-pole residual TMI data. The results of the standard Euler solutions obtained are shown in Figures 1.13-1.15. In Figure 1.13A, we show the standard Euler solution computed with a structural index of 0 and a tolerance error less than 12% plotted on top of the reduced-to-pole TMI map. The solutions clustered around the magnetic anomalies. Next, we generated a depth to the top of basement map (Fig. 1.13B) of the area using the solutions obtained from Figure 1.13A and compared these two maps. The top to the magnetic basement ranges from about 400 m to 5300 m (~1250 to 17000 ft). The sets of the block arrows with same colors are used in both maps (Figs. 1.13A and B). The positive and negative magnetic anomalies from Figure 1.13A are related to the deeper and shallower depth to the top of basement on 1.13B respectively as shown by the black arrows. However, the

area shown by the white arrow shows the opposite result with positive magnetic high anomaly related to shallower top of the basement. The depth to the top of magnetic basement within the seismic survey ranges from about 1500-2800 m (~5000 - 9100 ft). This basement depth interpretation lies within the error range of Euler deconvolution of magnetic data while compared with the result from the seismic data.

Next, we plotted the Euler solutions on the filtered magnetic maps. Figures 1.14A and B show the standard Euler solutions plotted on the tilt derivative and total horizontal derivative of reduced-to-pole residual TMI maps respectively. The solutions are clustered along the edges of the magnetic anomalies on the tilt derivative maps where the zero values of the anomalies are observed. In Figure 1.14B, the Euler solutions are clustered at the center of the magnetic anomalies. Verduzco et al. (2004), and Lahti and Karinen (2010) explained that the tilt derivative has its zero values close to the edges of the magnetic bodies. In case of the total horizontal derivatives, the maxima are generally sharper and are directly above the edges of the anomalies.

We also compared the faults mapped in seismic data with the results from the Euler solution to see if they correlate. The results are presented in Figure 1.15. Figures 1.15B and C show windowed Euler solutions with structural index of 0 and 1 respectively with tolerance error of 12%. Trend and location of mapped faults F1 and F3 in Figure 1.15A matches with the location of these faults in Figure 1.15B and 1.15C respectively. From the seismic section, we know F1 is a large offset irregular fault, whereas fault F3 is smaller offsets planer fault suggesting the use of SI values of 0 and 1 respectively as explained. However, the standard Euler solutions do not capture faults F2 and F4 that were mapped in the seismic section. We explain this either because of

the inadequate fault offsets or due to the insufficient difference in the magnetic sources across these faults.

Geological and geospatial database

In addition to the seismic, gravity, and magnetic data, we also considered information obtained from other sources such as geological maps, tectonic maps, fault databases, DEM data, interpreted well logs, and interpreted 2D deep seismic refraction profiles to generate a regional gravity model (Fig. 1.11). The geological maps, DEM data, and fault map are available online in the USGS websites. Well locations and digital well log data are accessible at no cost for download via the Texas Rail Road Commission (TRRC) website [http://www.rrc.state.tx.us/data/online/gis/index.php]. All these data have been integrated to aid our interpretation of the geological structure and tectonic setting of the southeast FWB region.

Integrated discussion of the results

After analyzing the seismic, gravity, magnetic, and geospatial data, we integrated these results and placed them in a tectonic context. We divide the tectonic evolution of the southeast FWB and its surrounding into the following two broad categories.

The Proterozoic evolution

From the rocks exposed in the core of LU area and eastern LU, we now know that there existed a Mesoproterozoic terrane and orogenic belt along the southern margin of Laurentia during the Grenville orogeny (Mosher et al., 2008). During this orogeny, the southern margin of the Laurentia collided with an oceanic arc that was

followed by the continental-continental collision, crustal thickening, and uplift (Mosher et al., 2008; Barker and Reed, 2010). During these processes, metamorphism and considerable magmatic activity took place, and granitic batholiths, sills and dykes were emplaced in the area. We observed some of these Precambrian sub-basement reflectors in the deeper section of our seismic data as shown in Figures 1.3, 1.7, and 1.8. We relate these reflectors to the granitic intrusions or some of the metamorphosed units that resulted from these events. Our integrated gravity model (Fig. 1.12) also includes batholiths and sills in the middle crust.

During the Neoproterozoic and Early Cambrian, the Rodinian supercontinent broke up to form a shallow-marine, passive margin that the Ouachita orogenic belt approximately followed and where the shallow marine and continental shelf deposits took place (Arbenz, 1989; Viele and Thomas, 1989). Extensional basins formed along the passive margin during this time. The shallow continental margin was bounded by oceanic crust until the Late Paleozoic (e.g., Keller et al., 1989). From exposures in the Ouachita Mountains and Marathon uplift and subsurface data, we know pre-orogenic Ouachita strata were deposited during the Late Proterozoic-Early Paleozoic and depositional environments ranged from deep-water to continental shelf to the shallow marine environment (Viele and Thomas, 1989). The pre-orogenic rocks include shale, sandstone, cherts, limestone, and dolomites. These rocks are identified as the lower unit of Ouachita facies. We included these units in the gravity model (Fig. 1.12) with appropriate rock densities.

The Paleozoic and Mesozoic evolution

During the Cambrian, the whole area was still under a shallow ocean, when the Wilberns and Riley Formation were deposited as sandstone, shale, and limestone. The area was often sub-aerially exposed and sometimes submerged (Preston et al., 1996), and hence, we see karst and collapse features in the Cambrian units on the seismic data (Figs. 1.4 and 1.5). In the Ordovician, carbonate rocks such as Ellenburger, Viola, and Simpson Groups were deposited. The presence of karst and collapse features in the seismic data (Figs. 1.3-1.7) indicates its sub-aerial exposure during this time as well. During the Late Mississippian and Early Pennsylvanian, compressional tectonics started and the ocean closed. Inboard from this tectonic activity, the Barnett Shale with frequent limestone layers was deposited during this period. Early Pennsylvanian syn-orogenic deposits formed in the Ouachita frontal zone in a deltaic environment (Walper, 1982; Viele, 1989). Meanwhile regional metamorphism occurred in the pre-orogenic Ouachita facies. The post-orogenic Late Pennsylvanian Units (Strawn, Canyon, and Cisco Groups) are predominantly shale, sandstone, conglomerate, and red beds, which indicate a fluvial depositional system. The seismic section and analyzed seismic attributes (Figs. 1.3-1.8) show these strata. The metamorphosed interior zone of the OOB is associated with regional gravity and magnetic high anomalies as shown in Figures 1.9-1.15.

The orogenic activity continued into the Early Permian forming the foreland FWB. Due to north-northwestward compression, the Bend arch, Muenster arch, and Lampasas arch formed around the FWB. We interpret faults F3 and F4 to bound a structural high related to the Lampasas arch (Figs. 1.3, 1.5A, and 1.8). Many of the

normal and reverse faults were active during the post-orogenic phase. Most of these faults are buried, but can be mapped in the seismic data (Figs 1.3-1.8). We also mapped some of these faults with help of the Euler deconvolution of magnetic data (Fig. 1.15). The general trends of these faults match with the principal stress direction of the area during the Ouachita orogeny. Some of these faults like F2 and F3 cut across the entire Paleozoic section and Precambrian basement (Figs. 1.3, 1.6, 1.7, and 1.8) and the karst and collapse features observed in the Paleozoic sequences align along these faults (Figs. 1.3-1.5). Elebiju et al. (2010) suggested the reactivation of some of the faults in the northeast portion of the FWB during the Ouachita orogeny, but we do not see the sign of reactivation of these faults in the southeast FWB. However, the presence of a pop-up block (Fig. 1.4) and possible Reidel shear zones (Fig. 1.7A) in the Paleozoic sequences of the southern FWB indicate the presence of transpressional tectonics in the area. The alignment of the collapse features with the mapped faults (Figs 1.4-1.7) suggests that there is some basement control on the overlying Paleozoic sequences and the associated reservoirs.

Conclusions

Although the basement and sub-basement reflectors are visible in the seismic sections, they are hard to trace throughout the seismic volume. To improve the visibility of these reflectors, we used volumetric seismic attributes. Some of the basement and intra-basement reflectors are dipping and folded. We interpret the intra-basement reflectors in the southeast FWB to represent igneous intrusions. The gravity and magnetic maps and models agree with these interpretations. The solutions from Euler deconvolution for determining top to the magnetic basement provided some useful

results and validated the fault interpretation from the seismic data. Some of the normal and reverse faults that cut across the Paleozoic sequence are also visible and penetrate the basement. The observation of the pop-up block and the possible Reidel shear zones within the seismic survey area indicates the presence of transpressional stress and complex tectonic deformation of the southeast Fort Worth Basin. Karst features that were previously mapped in the northern part of the FWB are also present in the shallower section in the southeast FWB. Alignment of these karst and collapse features with the mapped faults indicates that the deep-seated faults and the collapse features are associated with reservoirs of the Ellenburger Group, Barnett Shale, and the Marble Falls Limestone

Acknowledgements

Many thanks go to the Marathon Oil Company for providing us a license to use their seismic data. The U. S. Geological Survey and Pan American Center for Environmental Studies (PACES) have made the gravity and magnetic data available to the public and can be accessed at http://research.utep.edu/paces/ and http://pubs.usgs.gov/ds/2006/232/. Seismic interpretation was done using Petrel Software using license provided to University of Oklahoma (OU) for research and education purpose by Schlumberger. Attributes were generated using software developed by OU′s AASPI industrial consortium. We also like to thank Nabanita Gupta and Atish Roy for their help in effectively using the technology.

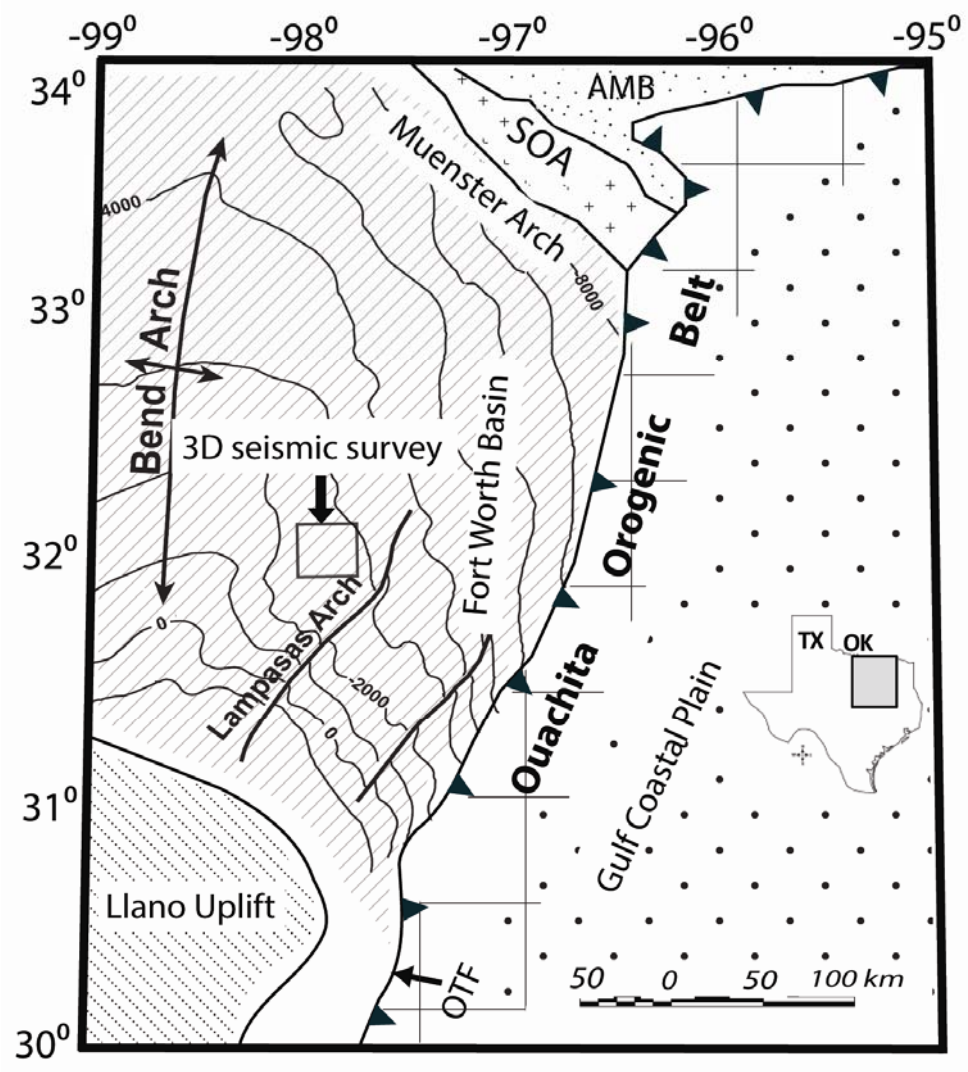

Figure 1.1: Index map of the study area showing Fort Worth Basin and major tectonic units surrounding it, modified after Ewing et al. (1990), Pollastro et al. (2007), and Keller (2009). The boundaries of the Ouachita orogenic belt, Llano uplift, Southern Oklahoma aulacogen (SOA), Ardmore-Marietta Basin (AMB), and Ouachita thrust front (OTF) are based on observed gravity anomalies. Contours represent the depth to the top of Ellenburger Group with an interval of 1000 ft (~305 m).

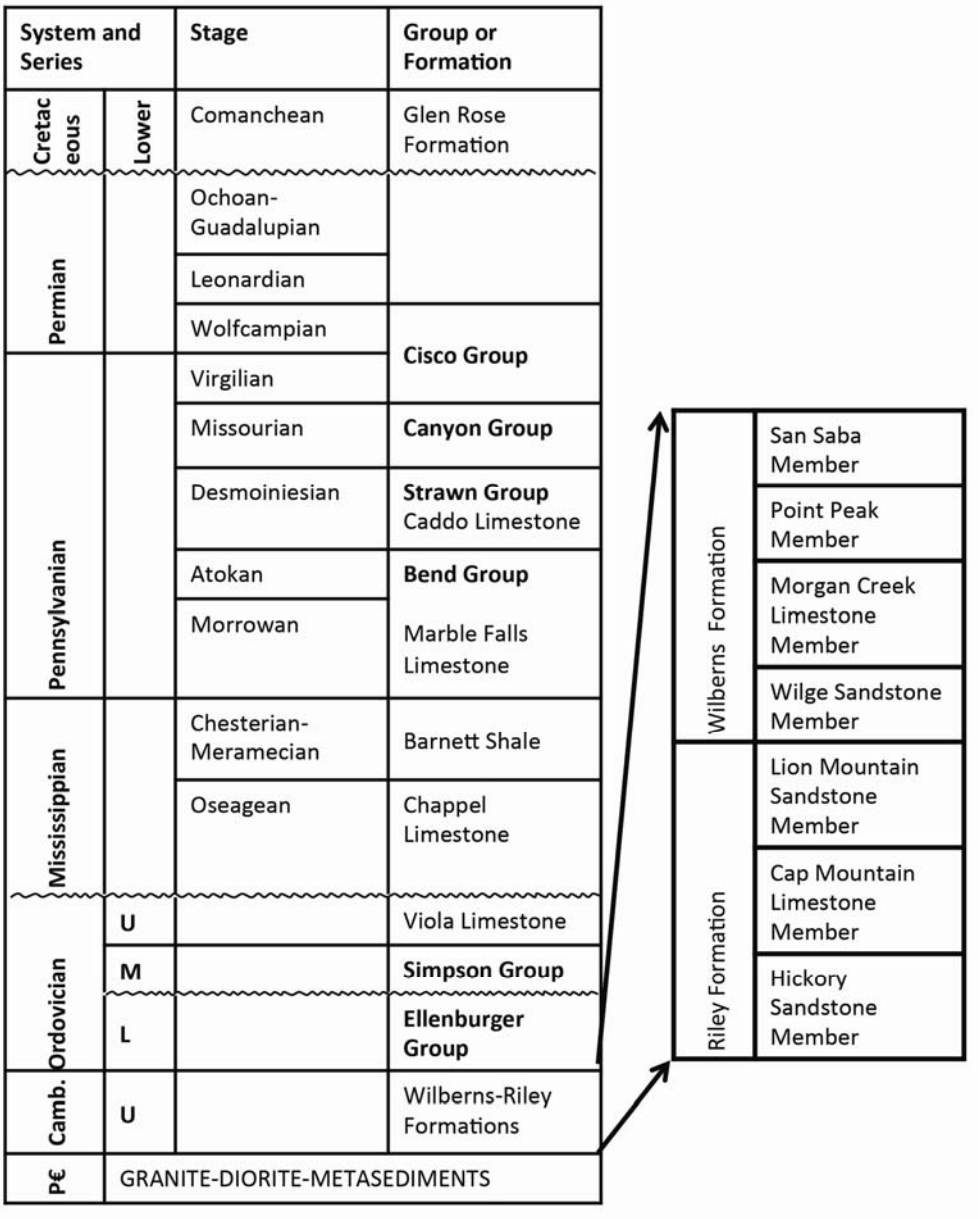

Figure 1.2: Generalized stratigraphic column in the Fort Worth Basin modified from Pollastro et al. (2003) and Smith (2004). The details of the Cambrian stratigraphy are based on the Llano uplift area, Central Texas.

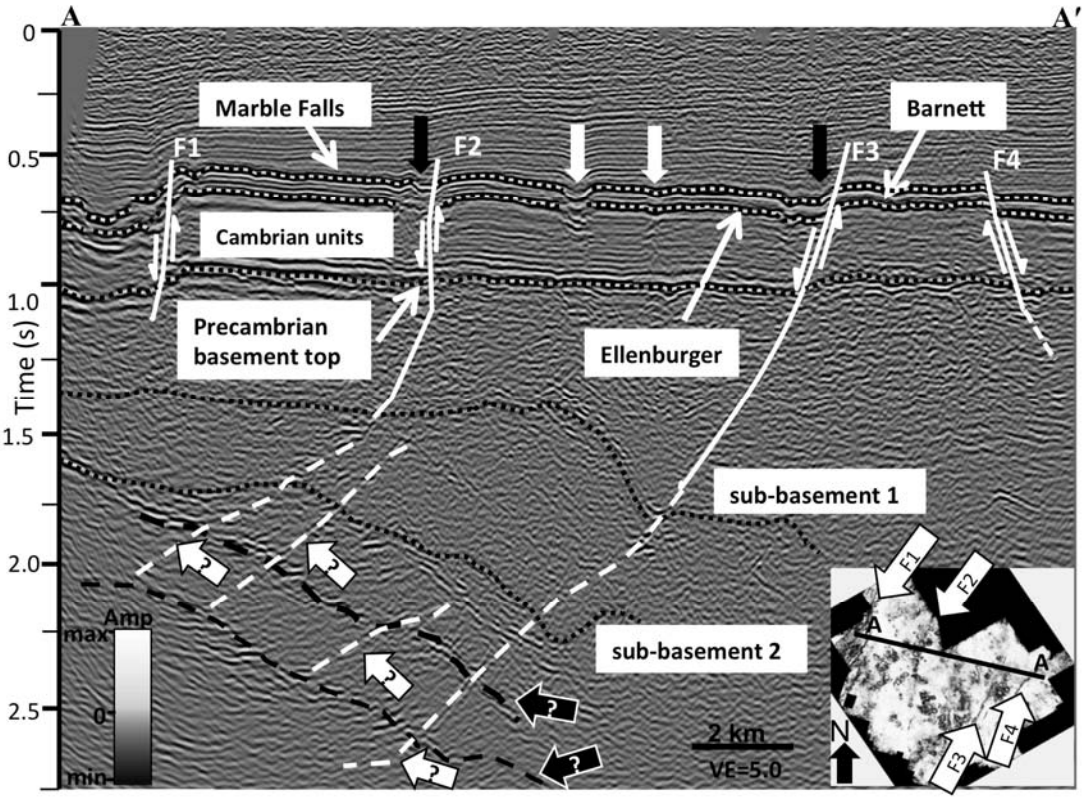

Figure 1.3: Interpreted seismic section across line AA′ as shown in the inset Figure. Four major faults namely F1, F2, F3, and F4, were picked that align NE-SW with the regional trend of Ouachita thrust fold belt. Major Paleozoic horizons, the top of Precambrian basement, and two sub-basement surfaces are picked (dotted black lines). The Paleozoic reflector such as Ellenburger Group, Marble Falls Limestone, and Barnett Shale are shown. The Ellenburger Group shows many of the karst and collapse features. Some of these collapse features are related to the basement and basement faults as identified by the black arrows whereas the others are not related and are shown by white arrows. Some unknown strong reflectors (dashed black line) below the basement are probably related to the intrusive bodies.

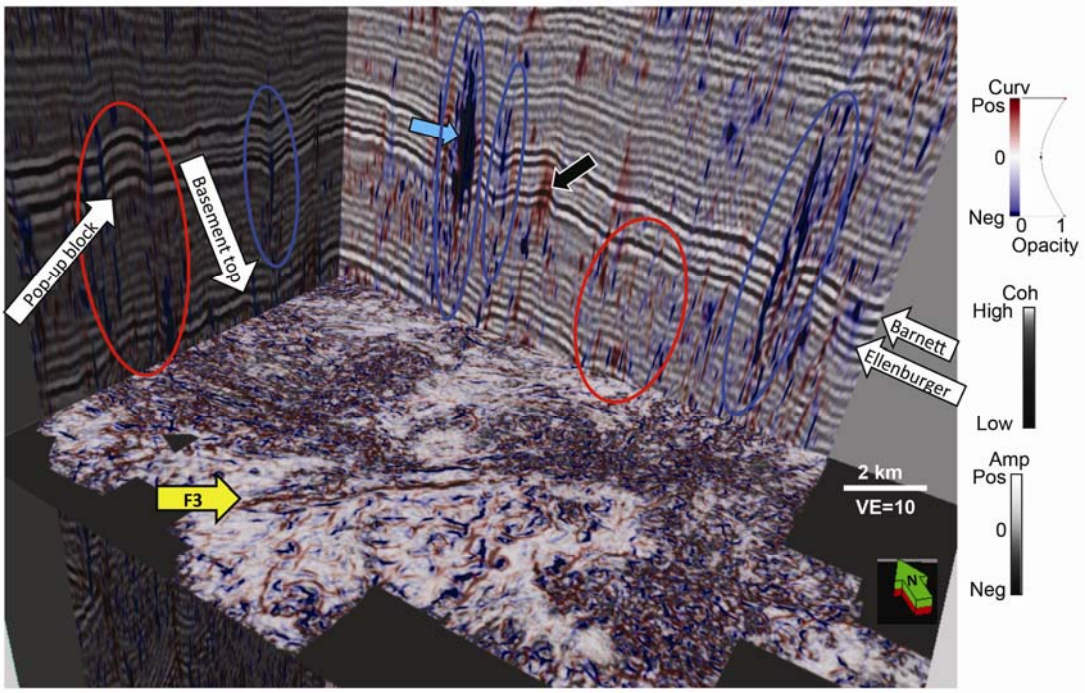

Figure 1.4: Illustration of geometric attributes using a 3D chair diagram showing vertical slices through seismic amplitude and a time slice at 0.98 s (approximate basement) through coherence co-rendered with most-positive and negative principal curvature. Blue areas (such as indicated by the cyan arrow) highlight valleys and bowls, while red areas (such as indicated by the black arrow) highlight ridges and domes. Probable pop-up block is observed in the NW corner of the survey indicating complex deformation history of the area.

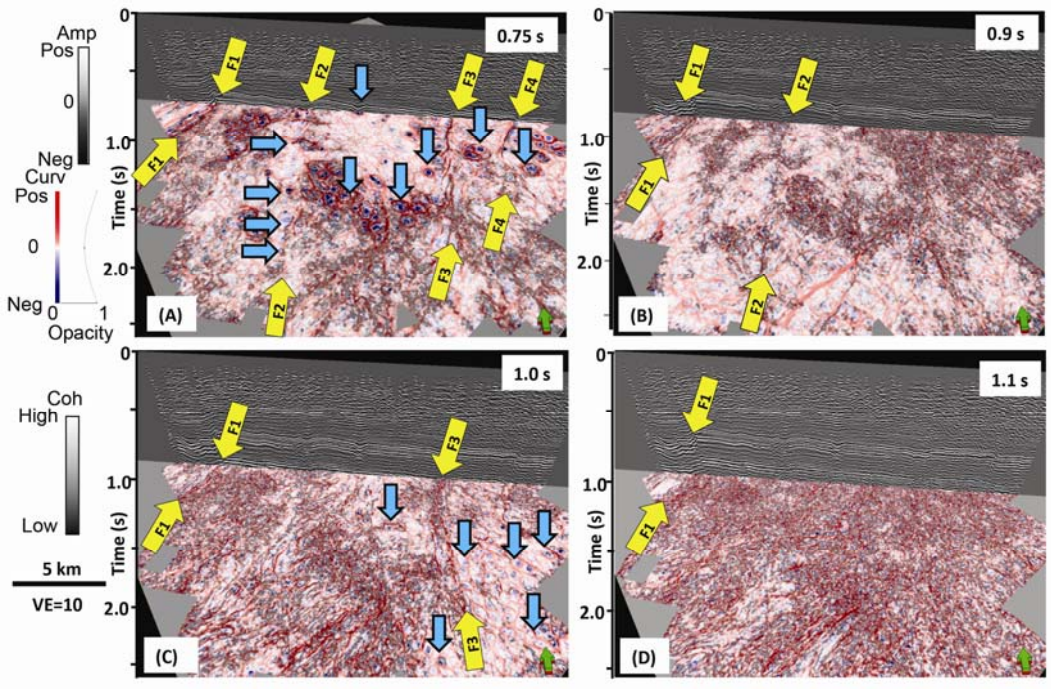

Figure 1.5: Display of karst, collapse features, and faults in the seismic data using coherence and curvature attributes and arbitrary seismic section at time: (A) t= 0.75 s, approximate Ellenburger top, (B) t= 0.9 s, at a Cambrian Unit (C) t= 1.0 s, approximate basement top, and (D) t= 1.1 s in the basement. Cyan arrows indicate collapse features whereas sets of yellow arrows shows major faults mapped in the area.

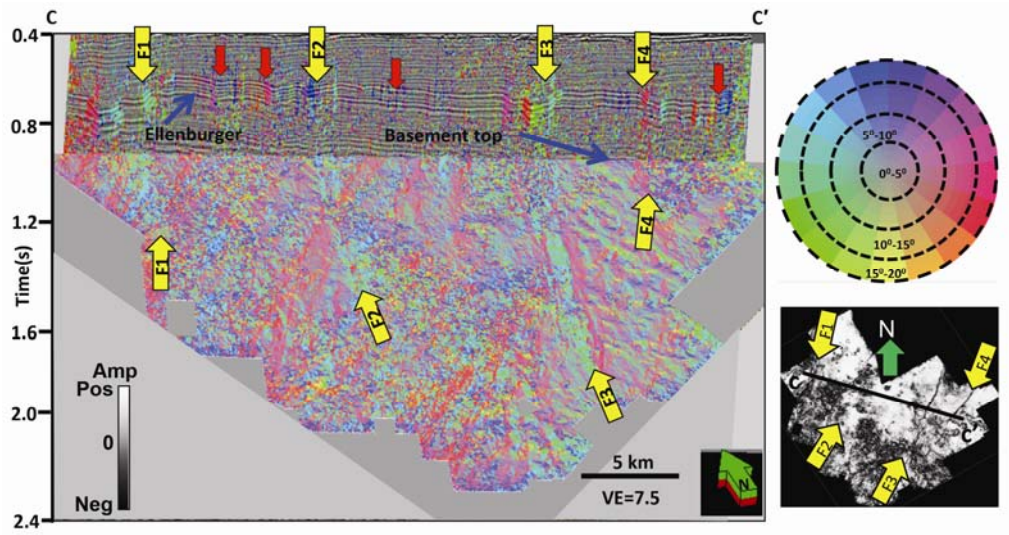

Figure 1.6: Combined dip and azimuth attributes co-rendered with arbitrary seismic section at line CC′ as shown in inset Figure with time slice at 0.98 s. The brighter color represents higher dip (highest dip amount is 20^0). Blue, red, yellow, and green colors represent structures dipping towards the north, east, south, and west respectively. Faults F1, F2, and F3 are green and dip toward west-northwest whereas fault F4 is red and dips east-northeast. The red arrows represent vertical karst and collapse related linear features that cut as deep as the top of Ellenburger Group.

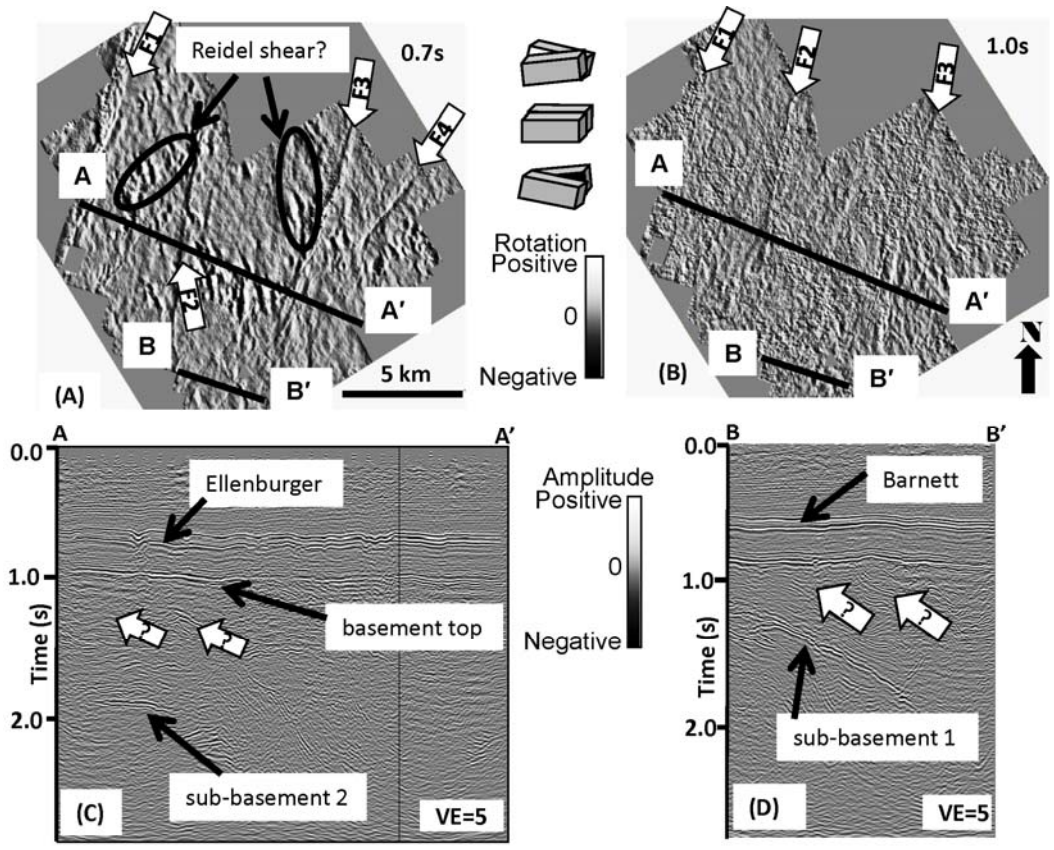

Figure 1.7: Time slice through the reflector rotation at (A) t=0.7 s (approximate top of the Ellenburger) and (B) t=1 s (approximate top of the basement) showing strong NNE-SSW trending fabrics. White lineaments are down to the right (clockwise rotation) while black lineaments are up to the right (counter-clockwise rotation). Probable Reidel shear structures are observed at the top of the Ellenburger Group. Figures C and D are vertical slices through seismic amplitude along lines AA′ and BB′. Key Paleozoic horizons and some strong Proterozoic reflectors are identified. Yet others are unidentified as shown by white arrows in Figures C and D.

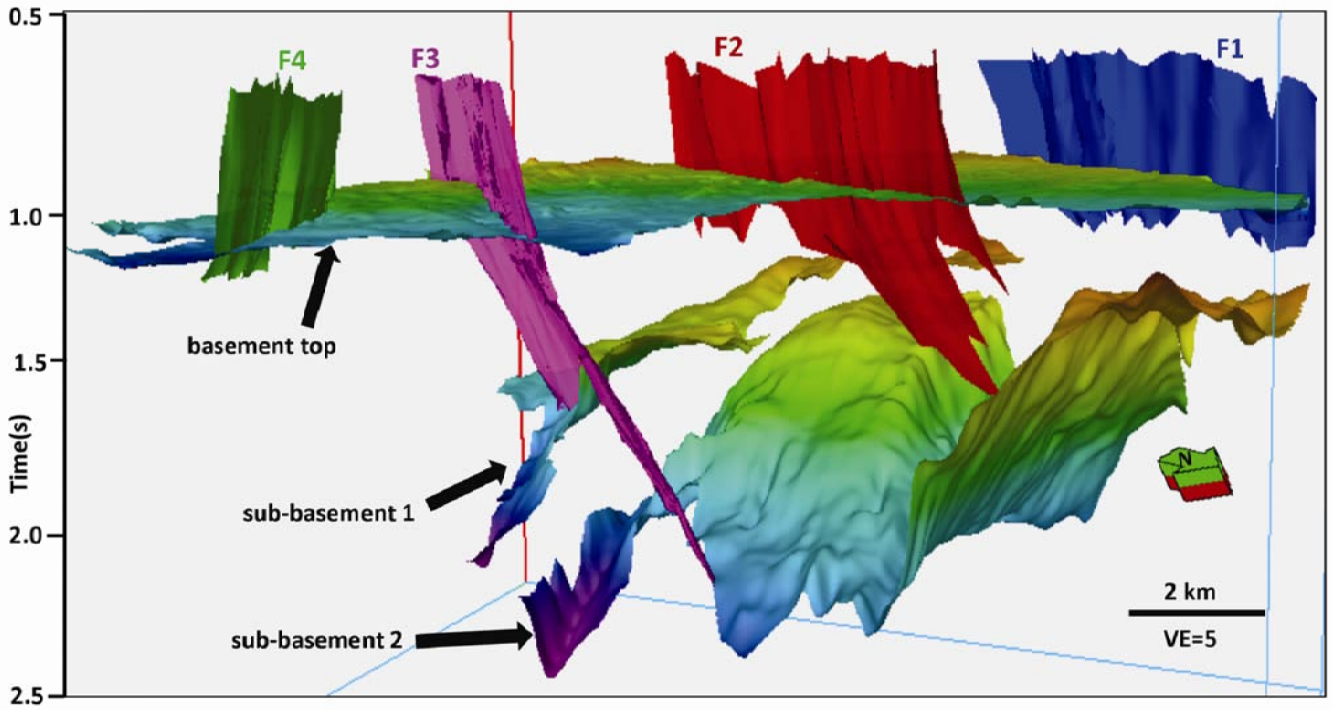

Figure 1.8: 3D perspective view of the picked faults and horizons on the seismic data. F1, F2, F3, and F4 are major faults mapped. These faults have NE-SW trends with F1, F2, and F3 dipping northwest whereas F4 dips southeast. The top of the basement is at about t=1.0 s. These basement and sub-basement surfaces represent different tectonic stages in the area.

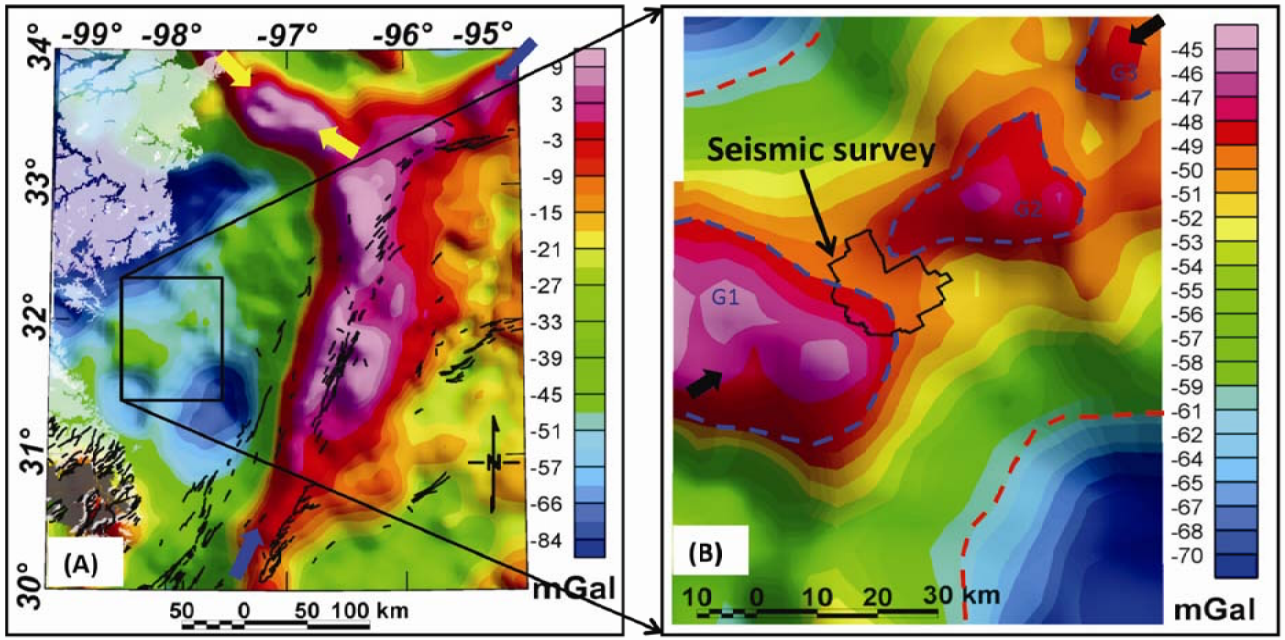

Figure 1.9: Complete Bouguer anomaly (CBA) maps of the study area. The set of blue and yellow arrows (Fig. A) represent gravity highs related to the Ouachita Orogenic belt and Southern Oklahoma aulacogen respectively whereas the gravity high in the southeast corner is related to the Llano uplift. The Fort Worth Basin is partly associated with a regional gravity low. Black linear lines represent surface faults (>4 km). Gray and white areas in the western side show Proterozoic and Paleozoic rock exposures respectively. Figure B is a zoomed in view that show a series of northeast-southwest trending local gravity high anomalies namely G1, G2, and G3 shown by a set of black arrows.

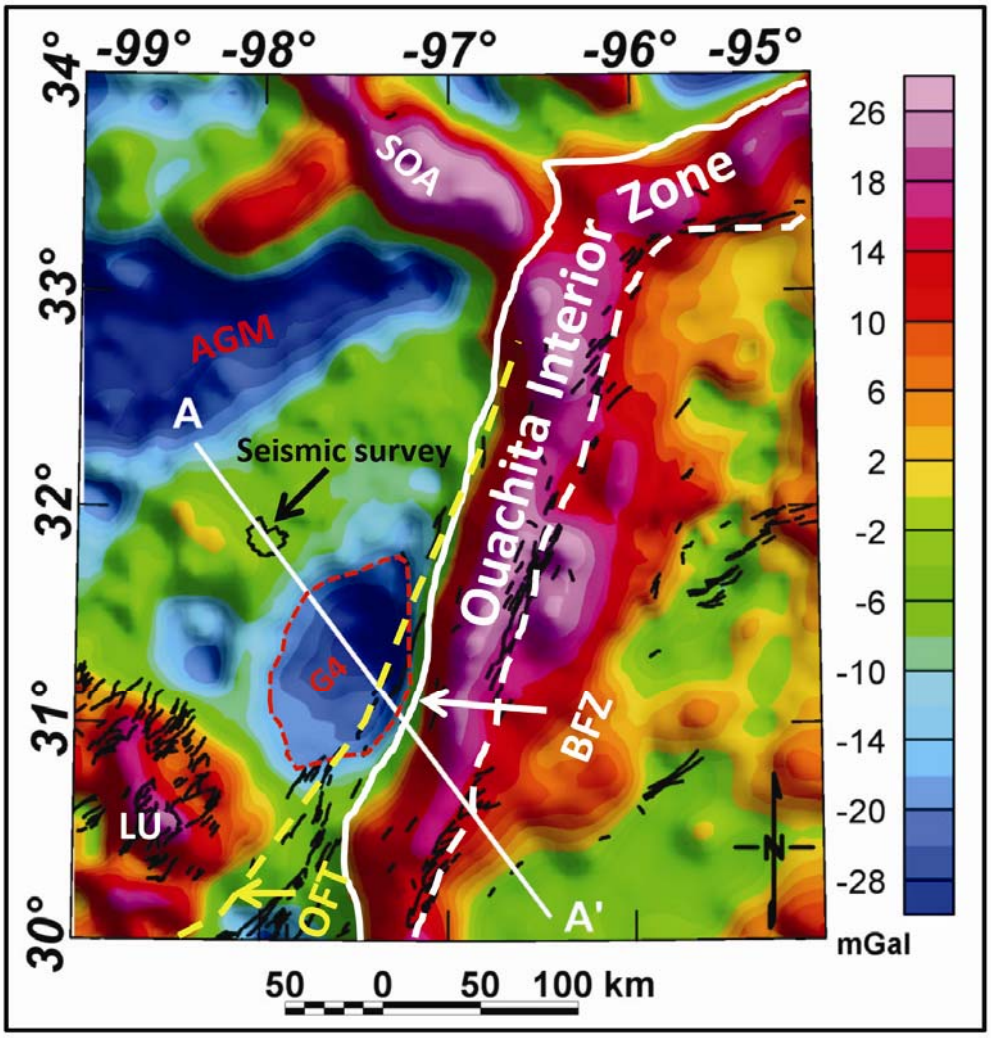

Figure 1.10: Residual CBA map of the study area after applying 40 km upward continuation filter. Major tectonic units and its boundaries are tentatively drawn based on the observed gravity anomaly. Acronyms used are: AGM= Abilene gravity minima, BFZ= Balcones fault zones, LU=Llano uplift, OFT= Ouachita frontal thrust, and SOA= Southern Oklahoma aulacogen. AA′ is a modeled gravity profile across the OOB (Fig. 1.12). We tentatively draw the OFT (dotted yellow) line based on work by Kruger and Keller (1986) and Flawn et al. (1961).

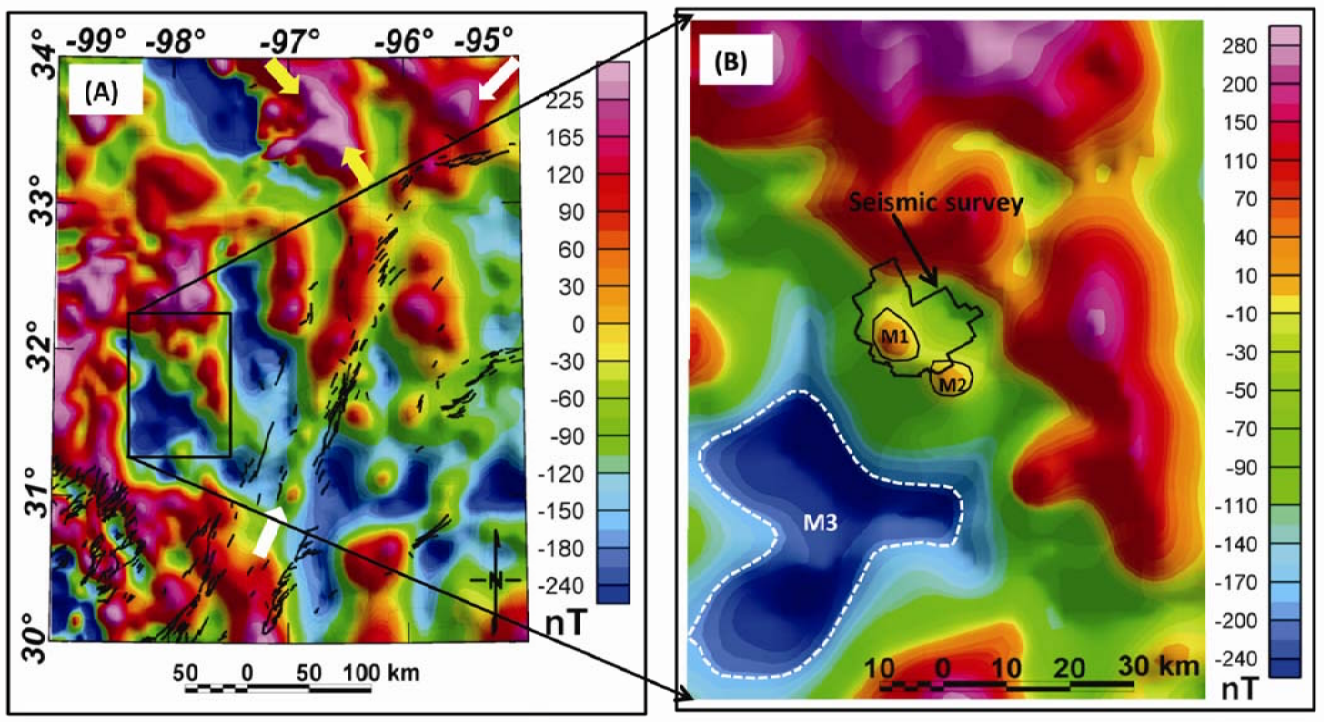

Figure 1.11: Residual total magnetic intensity (TMI) maps of the study area after reducing to magnetic pole. Figure A shows residual TMI map of the regional area. The set of white and yellow arrows represent magnetic highs related to the OOB and SOA respectively. Black lines represent surface faults (>4 km). Figure B is zoomed in view with outlines of the major magnetic anomalies in the vicinity of the seismic survey.

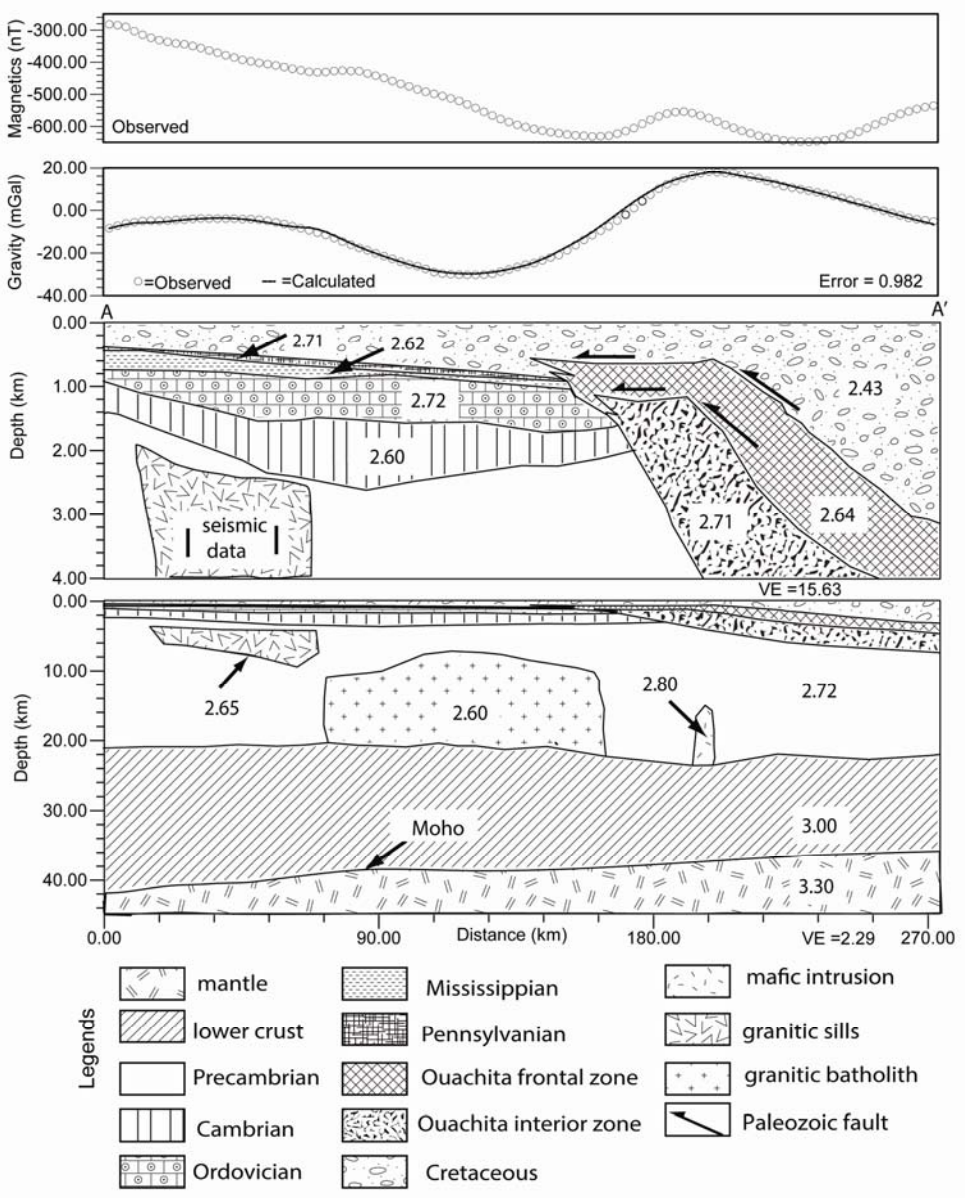

Figure 1.12: Regional gravity model across the OOB on profile AA′ across the seismic survey as shown in Figure 1.10 starting at Fort Worth Basin to the Gulf coastal plains. We used shallow well logs, seismic data, geospatial data, and geological information from published literature to model the residual gravity. The density values are in g/cm^3. VE in the Figure stands for vertical exaggeration showing the third and fourth panels have different vertical scales.

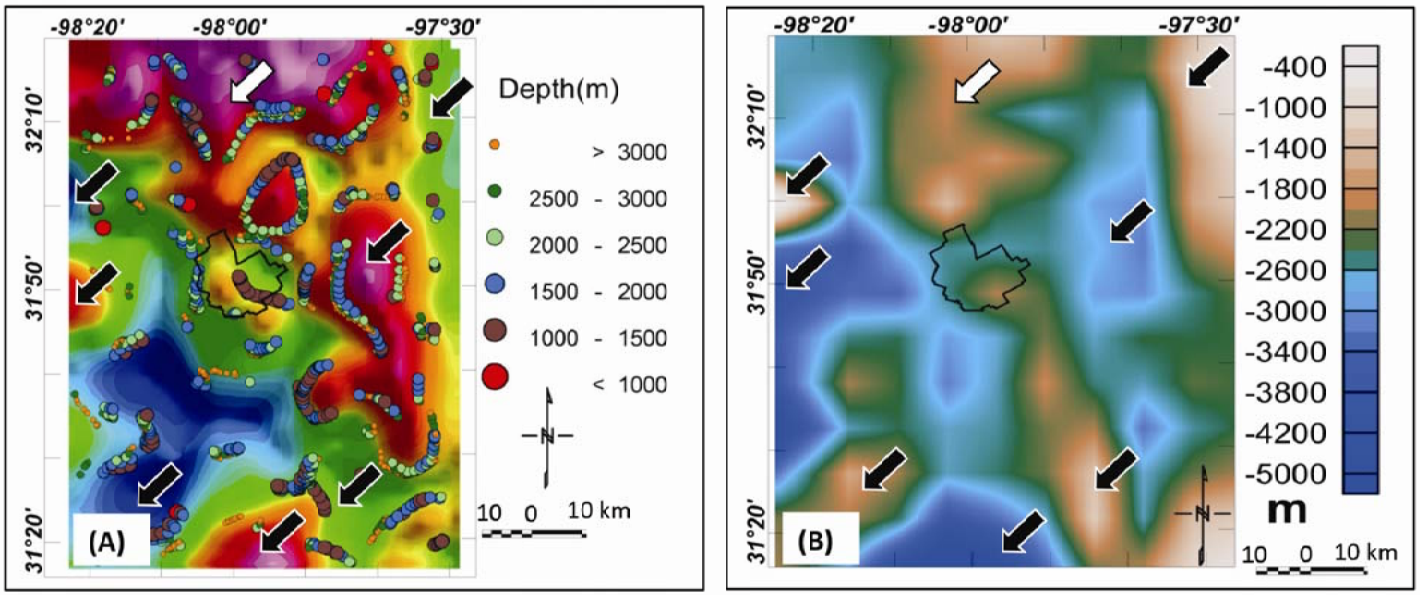

Figure 1.13: Depth to basement solution derived from Euler deconvolution with the structural index value of 0. Reduced-to-pole residual TMI grid is used on to compute the solutions. Figure A shows standard Euler depth solutions on top of the reduced-to-pole residual TMI grid. Figure B shows a contour depth map based on the solutions from A. Sets of black and white arrows show relationships between basement depth and the magnetic anomalies, where black arrows show the area with inverse relation and white arrow shows the area with direct relation.

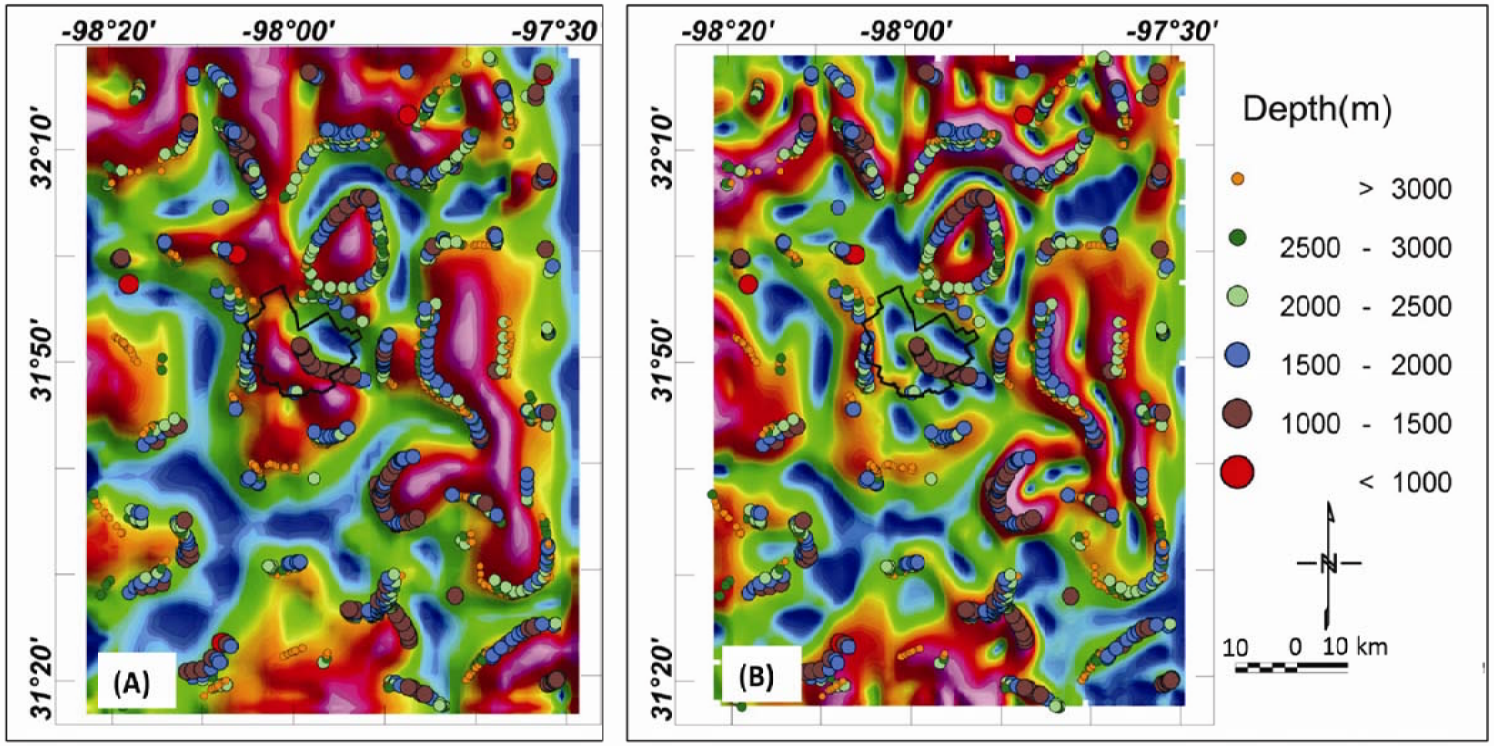

Figure 1.14: Standard Euler solutions from Figure 1.13 are plotted on top of: (A) the tilt derivative and (B) the total horizontal derivative of the reduced-to-pole residual TMI map. The solutions are clustered around the edges (close to zero) and the center of the magnetic anomalies in Figures A and B respectively.

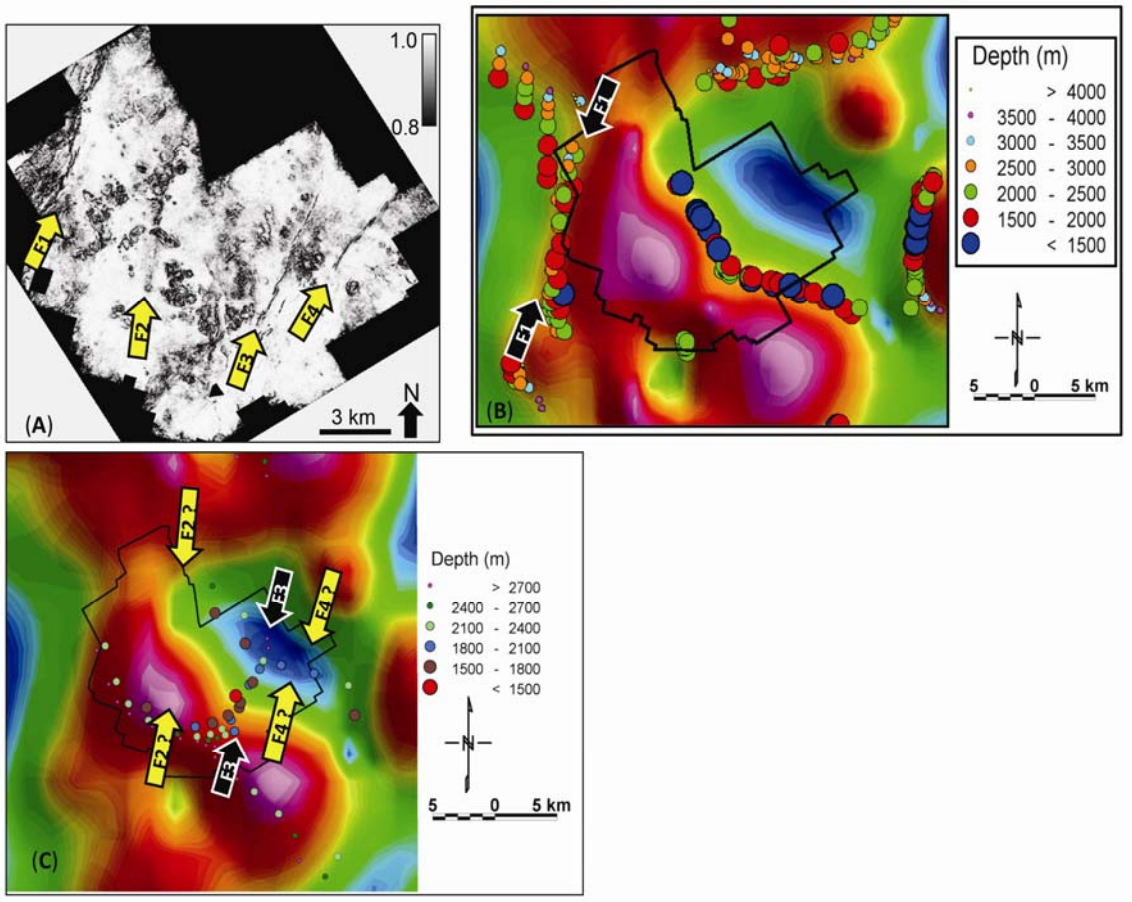

Figure 1.15: Comparing fault locations between seismic data and Euler solutions. Figure (A) shows faults F1, F2, F3, and F4 picked on 3D seismic data with coherence time slice at 0.75 s. Windowed standard Euler solutions with SI values of 0 and 1 are shown in Figures B and C respectively. Trend and location of faults F1 and F3 from Figure A tentatively match with the faults in Figures B and C respectively.

References

Adams, D.C., and G.R. Keller, 1996, Precambrian basement geology of the Permian basin region of West Texas and eastern New Mexico: A geophysical perspective: AAPG Bulletin, 80, 410-431.

Aktepe, S., K.J. Marfurt, and R. Perez, 2008, Attribute expression of basement faulting-time versus depth migration: The Leading Edge, 27, 360-367.

Arbenz, K.J., 1989, Ouachita thrust belt and Arkoma Basin: Hatcher RD Jr., Thomas W. A., and Viele G.W., eds., The Appalachian-Ouachita orogen in the United States: GSA Bulliten, 621-634.

Arbenz, K.J., 2008, Structural framework of the Ouachita Mountains, in Suneson, N. H.,(ed.), Stratigraphic and structural evolution of the Ouachita Mountains and Arkoma Basin, southern Oklahoma and west-central Arkansas: Applications to petroleum exploration: 2004 Field Symposium. Oklahoma Geological Survey, Circular 112A, the Arbenz-Misch/Oles volume, 1-40.

Barbosa, V.C.F., J.B.C. Silva, and W.E. Medeiros, 1999, Stability analysis and improvement of structural index estimation in Euler deconvolution: Geophysics, 64, 48-60.

Barker, D.S., and R.M. Reed, 2010, Proterozoic granites of the Llano Uplift, Texas: A collision–related suite containing rapakivi and topaz granites: GSA Bulletin, 122, 253-264.

Blakely, R.J., 1996, Potential theory in gravity and magnetic applications, Cambridge University Press, Cambridge, UK.

Boerner, D.E., B., Milkereit, and A. Davidson, 2000, Geosciences impact: A synthesis of studies of the Sudbury structure. Canadian Journal of Earth Sciences, 37(2-3), 477-501.

Brown, A.R., 1996, Seismic attributes and their classification: The Leading Edge, 15, no.10, 1090.

Brown, A.R., 2011, Interpretation of three-dimensional seismic data, in geophysics 9 and AAPG Memoir 42, 534.

Bruner, K.R., and R. Smosna, 2011, A Comparative study of the Mississippian Barnett Shale, Fort Worth Basin, and Devonian Marcellus Shale, Appalachian Basin, US Department of Energy, National Energy Technology Laboratory, report, DOE/NETL-2011/1478.

Carter, K.E., 1989, Grenville orogenic affinities in the Red Mountain area, Llano Uplift, Texas: Canadian Journal of Earth Sciences, 26, 1124-1135.

Chopra, S., and K.J. Marfurt, 2005, Seismic attributes A historical perspective: Geophysics, 70, 3SO-28SO.

Chopra, S., and K.J. Marfurt, 2007a, Seismic attributes for prospect identification and reservoir characterization, Geophysical development series no. 11, Tulsa: Society of Exploration Geophysicists, 464.

Chopra, S., and K.J. Marfurt, 2007b, Volumetric curvature attributes add value to 3D seismic data interpretation: The Leading Edge, 26, 856-867.

Dalziel, I.W.D., L.H. Dalla Salda, and L.M. Gahagan, 1994, Paleozoic Laurentia-Gondwana interaction and the origin of the Appalachian-Andean mountain system: GSA Bulletin, 106, 243-252.

Denison, R., 1989, Foreland structure adjacent to the Ouachita foldbelt: The Appalachian-Ouachita orogen in the United States: Boulder, Colorado, Geological Society of America, Geology of North America, 2, 681-688.

Dennie, D.P., 2010, An integrated paleomagnetic and diagenetic investigation of the Barnett Shale and underlying Ellenburger Group carbonates, Fort Worth Basin, Texas, PhD dissertation, University of Oklahoma.

Elebiju, O.O., G.R. Keller, and K.J. Marfurt, 2010, Case history investigation of links between Precambrian basement structure and Paleozoic strata in the Fort Worth Basin, Texas, USA, using high-resolution aeromagnetic, HRAM data and seismic attributes: Geophysics, 75, B157-B167.

Erlich, R., and J. Coleman, 2005, Drowning of the Upper Marble Falls carbonate platform (Pennsylvanian), central Texas: A case of conflicting "signals?": Sedimentary Geology, 175, 479-499.

Ewing, T.E., R.T. Budnik, J.T. Ames, D.M. Ridner, and R. Dillon, 1990, Tectonic map of Texas: Bureau of Economic Geology, University of Texas at Austin.

Ferrill, D.A., and A.P. Morris, 2008, Fault zone deformation controlled by carbonate mechanical stratigraphy, Balcones fault system, Texas: AAPG Bulletin, 92, no. 3, 359-380, doi:10.1306/10290707066.

Flawn, P.T., A. Goldstein, P.B. King, and C.E. Weaver, 1961, The Ouachita System. Austin, Texas, University of Texas, Bureau of Economic Geology, 401p.

Freeman, T., and G.,Wilde, 1964, Age and stratigraphie implications of major faults in the Llano region, Central Texas: AAPG Bulletin, 48, 714-718.

Gao, S.S., K.H. Liu, R.J. Stern, G.R. Keller, J.P. Hogan, J. Pulliam, and E.Y. Anthony, 2008, Characteristics of mantle fabrics beneath the south-central United States: constraints from shear-wave splitting measurements: Geosphere, 4, 411-417.

Gardner, G., L. Gardner, and A. Gregory, 1974, Formation velocity and density; the diagnostic basics for stratigraphic traps: Geophysics, 39, 770-780.

Hardage, B., D. Carr, D. Lancaster, J. Simmons Jr, R. Elphick, V. Pendleton, and R. Johns, 1996, 3-D seismic evidence of the effects of carbonate karst collapse on overlying clastic stratigraphy and reservoir compartmentalization: Geophysics, 61, 1336-1350.

Henry, J.D., 1982, Stratigraphy of the Barnett Shale (Mississippian) and associated reefs in the northern Fort Worth Basin, Dallas Geological Society, Dallas, Texas. 157-177.

Keller, G.R., J. Kruger, K. Smith, and W. Voight, 1989, The Ouachita system: A geophysical overview: The Appalachian–Ouachita orogen in the United States, Geol. North Am., F-2, 689-694.

Keller, G.R., 2009, Some Thoughts on the structure and evolution of the Ouachita Mountains-Arkoma Basin region: Oklahoma Geology Notes, 69, 4-12.

Keller, G.R., and R.D. Hatcher, 1999, Some comparisons of the structure and evolution of the southern Appalachian–Ouachita orogen and portions of the Trans-European Suture Zone region: Tectonophysics, 314, 43-68.

Keller, G.R. and S.E, Cebull, 1973, Plate tectonics and the Ouachita system in Texas, Oklahoma and Arkansas: GSA Bulletin, 83, 1659-1665.

Kruger, J., and G.R. Keller, 1986, Interpretation of crustal structure from regional gravity anomalies, Ouachita Mountains area and adjacent Gulf Coastal Plain: AAPG Bulletin, 70, 667-689.

Lahti, I., and T. Karinen, 2010, Tilt derivative multiscale edges of magnetic data: The Leading Edge, 29, 24-29.

Levine, J., and S. Mosher, 2010, Contrasting Grenville-aged tectonic histories across the Llano uplift, Texas: New evidence for deep-seated high-temperature deformation in the western uplift: Lithosphere, 2, 399-410.

Loucks, R.G., 2003, Review of the Lower Ordovician Ellenburger Group of the Permian Basin, West Texas, Bureau of Economic Geology, Austin, TX, 92.

Loucks, R.G., and S.C. Ruppel, 2007, Mississippian Barnett Shale: Lithofacies and depositional setting of a deep-water shale-gas succession in the Fort Worth Basin, Texas: AAPG Bulletin, 91, 579-601.

Marfurt, K.J. and J. Rich, 2010, Beyond curvature – volumetric estimates of reflector rotation and convergence, 80th Annual international Meeting, SEG, Expanded Abstracts, 1467-1472.

Meckel Jr, L.D., D.G. Smith, and L.A. Wells, 1992, Ouachita foredeep basins: Regional paleogeography and habitat of hydrocarbons: Foreland Basins and Fold Belts. Tulsa, AAPG Memoir, 55, 427-444.

Mickus, K., and G.R. Keller, 1992, Lithospheric structure of the south-central United States: Geology, 20, 335-338.

Miller, H.G., and V. Singh, 1994, Potential field tilt—a new concept for location of potential field sources: Journal of Applied Geophysics, 32, 213-217.

Montgomery, S.L., D.M. Jarvie, K.A. Bowker, and R.M. Pollastro, 2005, Mississippian Barnett Shale, Fort Worth Basin, north-central Texas: Gas-shale play with multi–trillion cubic foot potential: AAPG Bulletin, 89, 155-175.

Mosher, S., J. Levine, and W. Carlson, 2008, Mesoproterozoic plate tectonics: A collisional model for the Grenville-aged orogenic belt in the Llano uplift, central Texas: Geology, 36, 55-58.

Nicholas, R., and D. Waddell, 1989, The Ouachita system in the subsurface of Texas, Arkansas, and Louisiana: The Appalachian-Ouachita orogen in the United States, Geological Society of America, The Geology of North America, 2, 661-672.

Nicholas, R.L., and R.A. Rozendal, 1975, Subsurface positive elements within Ouachita foldbelt in Texas and their relation to Paleozoic cratonic margin: AAPG Bulletin, 59, 193-216.

Oliver, H.W., 1977, Gravity and magnetic investigations of the Sierra Nevada batholith, California: GSA Bulletin, 88, 445-461.

Pollastro, R.M., R.J. Hill, D.M. Jarvie, and M.E. Henry, 2003, Assessing undiscovered resources of the Barnett-Paleozoic total petroleumsystem, Bend arch–FortWorth Basin province, Texas: Transaction of the AAPG Southwest Section Convention, Fort Worth, Texas, American Association of Petroleum Geologist/ Datapages, 18., CD-ROM. http://www.searchanddiscovery.com/documents/pollastro/index.htm (accessed, June 2004).

Pollastro, R.M., D.M. Jarvie, R.J. Hill, and C.W. Adams, 2007, Geologic framework of the Mississippian Barnett shale, Barnett-paleozoic total petroleum system, Bend arch–Fort Worth Basin, Texas: AAPG Bulletin, 91, 405-436.

Preston, R.D., D.J., Pavilcek, R.L., Bluntzer, and J., Derton, 1996, The Paleozoic and related aquifers of central Texas, Texas Water Development Board, Austin, report 346 77.

Reid, A.B., J. Allsop, H. Granser, A. Millet, and I. Somerton, 1990, Magnetic interpretation in three dimensions using Euler deconvolution: Geophysics, 55, 80-91.

Schuelke, J.S., 2011, Overview of seismic attribute analysis in shale play; Attributes: new views on seismic imaging - their use in exploration and production, 31st annual GCSSEPM Foundation Bob F. Perkins Research Conference, December 4-7, Houston, Texas.

Smith, R., 2004, Paleozoic aquifers of the Llano Uplift: Aquifers of the Edwards Plateau: Texas Water Development Board Report, 360, 181-200.

Sullivan, E.C., K.J. Marfurt, A. Lacazette, and M. Ammerman, 2006, Application of new seismic attributes to collapse chimneys in the Fort Worth Basin: Geophysics, 71, B111-B119.

Tai, D.T.W., 1979, Subsurface study of Atoka (Lower Pennsylvanian) clastic rocks in parts of Jack, Palo Pinto, Parker, and Wise counties, north-central Texas: AAPG Bulletin, 63, 50-66.

Thomas, J. D., and W. Texas, 2003, Integrating synsedimentary tectonics with sequence stratigraphy to understand the development of the Fort Worth Basin: AAPG Southwest Section Meeting, Ruidoso, New Mexico, 6-8 June. http://www.searchanddiscovery.com/abstracts/pdf/2003/2002sw/image/ndx_thomas.pdf.

Thompson, D., 1982, EULDPH; a new technique for making computer-assisted depth estimates from magnetic data: Geophysics, 47, 32-38.

Verduzco, B., J. D., Fairhead, C.M. Green, and C. MacKenzie, 2004, New insights into magnetic derivatives for structural mapping: The Leading Edge, 23, 116-119.

Viele, G.W., 1989, The Ouachita orogenic belt: in Hatcher, R.D., Jr., Thomas W. A, and G.W., Viele, eds., The Appalachian-Ouachita orogen in the United States, Geology of North America, F-2, 555-561.

Viele, G.W., and W.A.,Thomas, 1989, Tectonic synthesis of the Ouachita oregenic belt: in Hatcher, R.D., Jr., Thomas W.A, and G.W.,Viele, eds., The Appalachian-Ouachita orogen in the United States, Geology of North America, F-2, 692-726.

Walper, J.L., 1982, Plate tectonic evolution of the Fort Worth Basin, in Martin, C. A., ed., Petroleum geology of the FortWorth Basin and Bend arch area: Dallas Geological Society, 237–251.

Chapter 2: Integrated geophysical imaging of the upper crustal features in the Harney Basin, southeast Oregon

Abstract: The Harney Basin is a relatively flat lying depression in the northeast corner of the enigmatic High Lava Plains volcanic province in eastern Oregon. A thick blanket of volcanics including flood basalts, rhyolites, tuffaceous deposits, ash flows, and distinct eruptive centers covers the basin making it very difficult to study the upper crustal features. In addition to the High Lava Plains active source seismic data, we also employed gravity, magnetic, digital elevation, and other geospatial data for this integrated study. We generated an upper crustal 3D seismic tomographic model of the Harney Basin and surrounding area using a sparse grid of 2D seismic lines. We then integrated it with gravity, magnetic, and geologic data to construct a geophysical model of the upper crustal structure, which reveals that the basin reaches as deep as 6 km in the central areas. The tomographic inversion shows some unusually high velocity (>6.5 km/s) bodies in the upper crust near the central basin area. The presence of several ash-flow tuffs and voluminous rhyolites in the Harney Basin region indicate the sources of these materials are nearby. We observe two major caldera shaped features within the basin, which are likely candidates for the source of some of these tuffaceous deposits. These potential calderas are associated with seismic low velocity areas, low gravity anomalies, and depressed topographic features. We interpret the extent of these calderas with the help of integrated geophysical results. We propose a nested caldera complex in the northern Harney Basin and smaller caldera in the southern part of the basin.

Key words: *Harney Basin, seismic tomography, gravity, integrated geophysical interpretation, caldera complex*

Introduction

The High Lava Plains (HLP) of Oregon is one of the key components of a large igneous province of the Pacific Northwest that was formed due to the complex intra-plate volcanism during the Cenozoic (e.g. Carson and Hart, 1987; Camp et. al, 2003; Streck and Grunder, 2008; Druken et al., 2011). The presence of Cenozoic volcanic activity in the region with lava flows and pyroclastic material poses a challenge to identify older crustal structures and tectonic events (Anderson, 1989). This tectonically complex area experienced various tectonic processes including Farallon plate subduction, back arc volcanism, ignimbrite flare ups (Lipman et al., 1971), flood basalt volcanism (Brueseke et al., 2007), strike slip deformation, Basin and Range extension, terrane accretion, and widespread mafic volcanism (Camp and Ross, 2004) in a comparatively short period of time. The non-extending accreted Blue Mountains terrains and the Columbia River Basalt Plateau lie north of the HLP. The east side of the HLP is bounded by the Sr 0.706 line that separates the North American craton to the east from the Mesozoic accreted terrains (Armstrong et al., 1977), whereas to the south the HLP is bounded by the northern Basin and Range province. The Cascade Range lies on the west side of the HLP. Other major units in the surrounding area are the Steens Basalt Dikes, Northern Nevada Dikes, Owyhee Plateau, Oregon-Idaho grabens, Brothers fault zones, the Newberry volcanic field, and a few other local volcanic fields (Figure 2.1).

The Harney Basin is one of the main components of the High Lava Plains (HLP) (Figure 2.1). It is bounded to the north and south by parts of the Blue Mountains and the Steens Mountain respectively. The eastern and western boundaries are somewhat ill defined. The Harney Basin lies in the northeastern part of the HLP. The basin is mostly covered with the Quaternary sediments and seasonal lakes with occasional basalt flows, tuffaceous deposits, volcanic ash, and some distinct volcanic centers.

Three voluminous tuff deposits have been mapped in the Harney Basin region. The 7.1 Ma old uniformly thick and widespread Rattlesnake Tuff (RST) is the largest one and covers about 9000 km^2 area (Streck and Grunder, 2008). When reconstructed, the areal coverage is estimated to be ~40,000 km^2 with a volume of 280 km^3 of dense rock equivalent (DRE). Based on degree of welding and the pumice size and thickness, its source has been inferred to be in the western Harney Basin (Streck and Grunder, 1995; 2008). The Devine Canyon Tuff (DCT) and Prater Creek Tuff (PCT) are other two widespread tuff deposits in the area. The DCT is 9.7 Ma old and covered an area of ~19000 km^2. The DRE volume is estimated to be ~195-250 km^3 (Greene, 1973), and the source is interpreted to be beneath the Harney Basin lowland based on the thickness and distribution of the deposits. Similarly PCT is an 8.4 Ma old deposits that had a DRE volume of about 100-150 km^3 (Greene, 1973; Ford, 2013). There are numerous small-scale ash flow deposits in the area, whose age range from 12 Ma to recent. Overall, these tuffs deposits and rhyolite distribution in the Harney Basin region and their massively reconstructed volumes indicate that there must be at least some sources for these eruptions in the proximity of the Harney Basin.

The Harney Basin has been interpreted as a large structural depression possibly created due to caldera collapse (e.g. Greene, 1973; Walker, 1979; Walker and Nolf, 1981, Streck and Grunder, 1995; 2008). In the Late Cenozoic, the depression was filled with ash-flow tuffs, tuffaceous sediments, basalt flows, rhyolites, andesites, basaltic breccias, detrital alluvial, fanglomerate, playa deposits, and lacustrine sediments derived from widespread igneous rocks (e.g. Piper et al., 1939; Baldwin, 1976; Walker, 1979; Russell, 1984). The evolution and the upper crustal structure beneath the Harney Basin are poorly understood due to the thick blanket of multi-phase volcanism.

The HLP active source seismic experiment in 2008 was primarily conducted to image the crustal and upper mantle structures beneath the HLP and Steens Mountain region. The survey consisted of two major long lines across the HLP and some short linking lines around the Harney Basin, which provides a modest 3D seismic survey (Fig. 2.2). In this study, we used six shots around the basin with five lines of receivers (Figs. 2.5 and 2.6). With multiple fan shot-receiver and some typical inline source-receiver geometry combinations, 26 different shot gathers were generated and used for the seismic analysis (Table 2.1).

In this research, we used the fast marching tomographic (FMTOMO) method for tomographic inversion of the seismic data. FMTOMO is capable of using active, passive, or both kinds of seismic data for inversion. This method has been successfully employed for crustal scale studies (e.g. Rawlinson and Urvoy, 2006; Brikke, 2010; Rawlinson et al., 2010; Rockett, 2011), and we created a 3D seismic tomographic image of the upper crustal features in the Harney Basin area. Gravity, magnetic, and geospatial data were also used. We collected over 1000 new gravity measurements, and

generated magnetic profiles and integrated gravity models across Harney Basin. The results from the seismic tomography, gravity models, geospatial data, surface geology, and topography were used in an integrated interpretation of the basin structure and evolution. Based on these results, we propose multiple caldera locations in the Harney Basin that are the probable sources for RST, DCT, and PCT deposits.

Regional geology

The HLP track is a bimodal volcanic trend that started at the McDermitt volcanic field (Figure 2.1) in southeast Oregon at about ~16 Ma (Pierce and Morgan, 1992). It continued in a WNW direction with its youngest volcanic center at the recently active Newberry volcano (e.g. Walker, 1974; Christiansen and McKee, 1978; Smith and Luedke 1984; Jordan et al., 2004; Meigs et al., 2009). The Brothers fault zone is the major structural feature approximately parallel with the HLP trend (Figure 2.1). The Brothers fault zone is interpreted as one of the major conduits for bands of rhyolitic volcanic deposits in the HLP (Christiansen and Yeats, 1992). Walker and Nolf (1981) suggested that the HLP emerges gradationally from the northern Basin and Range Province based on the similarities observed on the fracture patterns and fault structures in the northern Basin and Range faults and the Brothers fault zones.

Another volcanic track started at the McDermitt field and moved NE toward Yellowstone through the Snake River Plain (SRP). The Yellowstone trend is also bimodal in composition. It has well defined volcanic centers that become younger to the northeast with Yellowstone being the youngest (Armstrong et al., 1975; Pierce and Morgan, 1992). Even though these two tracks mirror each other and have many similarities, key differences are seen in the gravity anomalies along them. The gravity

anomalies along the Snake River Plain form a distinct gravity high indicating significant magmatic modification of the crust whereas those of the HLP are significantly lower and irregular.

The genesis of the HLP track and its possible relation to the SRP volcanic track is highly debated. Among many of the hypotheses, backarc extension is postulated as a dominant force (e.g. Eaton, 1984; Carlson and Hart, 1987). Draper (1991) and Pierce and Morgan (1992) suggested that a plume beneath the McDermitt volcanic center drove both the HLP and SRP volcanic tracks but in opposite directions. This caused the voluminous basalt flow and bimodal volcanism in the HLP. Hooper et al. (2002) suggested the extension of the northern Basin and Range province in the HLP region is the major cause of volcanism in the HLP. The Steens Basalt and Columbia River Basalt erupted at about 16-17 Ma, which was followed by the extensive bimodal rhyolitic and basaltic volcanism in the area (Hooper, 1997). Camp et al. (2003) divided the volcanism into two broader phases based on their study done in the Malheur River Gorge, Oregon. In the Middle Miocene, the flood basalt volcanism was active and the tholeiitic mafic and bimodal basalt erupted initially followed by the early diktytaxitic olivine basalt. In the Late Miocene to present, the Basin and Range extension caused the wide spread volcanism in the HLP. In this phase, intermediate to felsic calc-alkaline rocks were erupted first and were followed by the late diktytaxitic olivine basalt. Hart (1985) suggested that the large voluminous basalt eruption in the Late Miocene were later replaced by primitive low–K, high Al, olivine tholeiite (HAOT) type of basalts. Based on a geochemical analysis of the HLP basalts, the genesis of its magma is interpreted to be in the lower crust or upper mantle (Jordan, 2002).

Previous geophysical studies of the HLP and Harney Basin

Most of the recent seismic studies in the region have employed passive seismic data from the EarthScope project's USArray of broadband stations and the High Lava Plains project's local broadband seismic network, along with permanent seismic stations for body wave, surface wave, and ambient noise tomography (e.g. Roth et al., 2008; West et al., 2009; Long et al., 2009). These studies were mainly focused on detecting mantle velocity anomalies, anisotropy, and heterogeneity.

Eagar et al. (2010, 2011) conducted a passive seismic experiment using 206 broadband seismometers stationed in and around the HLP region to study the crustal composition and structure in the region. They found the Moho depth at about 31 km in the HLP region. The abnormally high Poisson's ratio in the western portion of HLP was interpreted because of widespread basaltic flows, which probably brought high velocity material and melts to the surface through the Brothers fault zones. The Poisson's ratio in the Harney Basin region is ~0.28 (Eagar et al., 2011), which indicates the possibility of moderately mafic crustal materials.

A few crustal-scale active-source seismic studies have been performed in the HLP area. Catchings and Mooney (1988) conducted a 180-km long refraction seismic experiment from the eastern Cascades to the eastern part of the HLP and generated a crustal scale velocity structure of the HLP and Newberry volcanic field. They found the near surface volcanic material's velocity ranges from 1.6 to 4.7 km/s and has a thickness of 3-5 km in most places, but in local basins it reaches a thickness of 5-6 km. The integrated geophysical study conducted by Lerch et al. (2007, 2008) in the northern Basin and Range province south of our study showed the presence of long-lived, large

volume volcanism with significantly less extension and tectonism as a key character of the northern Basin and Range Province. Moving north into the southern HLP province, the extension slowly fades away with increased volcanic activities. In the HLP region, volcanism is dominant over the extension.

The 2008 HLP active seismic data has been analyzed before (e.g. Okure, 2009; Cox, 2011) and interpreted in the form of 2D seismic lines. Okure (2009) used the HLP seismic data around the Harney Basin area and tentatively marked the basin boundary based on the traveltime delays observed in the seismic data. Cox (2011) also used the HLP active seismic data for a crustal scale study and interpreted two long 2D lines across the HLP region. A 5-7 km thick upper layer of sediments and volcanics was detected in the region. Underplating in the lower crust and magmatic modification within the crust was observed beneath the Harney Basin (Cox, 2011).

Geophysical data

Active seismic data collection

In September 2008, a wide-angle reflection and refraction (WARR) seismic experiment was conducted in the HLP and Steens Mountain area, using 15 one-ton explosive sources and 2612 Texan recording instruments with 4.5 Hz geophones. Average spacing between recording stations was ~800 m with average source spacing of ~50 km. In addition to the Texan instruments, 120 RefTek RT 130 receivers were also deployed across the Steens Mountain. Two major lines, one about 400 km long in NW-SE direction and the other about 350 km in N-S direction, cross each other near Burns, Oregon. In addition to these lines, some short linking profiles were deployed in and around the Harney Basin (Fig. 2.2) in order to provide some 3-D coverage over this

interesting feature. Super shot gathers were generated from the seismic data for each shot and consists of 1148 receivers (seismic traces). Figure 2.3 shows an example of a raw super-gather for shot point 24. Our major aim is to create a 3D seismic velocity model of the upper crustal features beneath the Harney Basin. The shot-receiver geometry in and around the Harney Basin was designed for 3D seismic velocity modeling and seismic tomography (Fig. 2.2). We sub-sampled these super-gathers and generated five new gathers in the area of interest (Fig. 2.5), and the details are listed in Table 2.1. In the following section, we discuss how these gathers were processed, picked, and used for tomographic inversion.

Seismic data processing and preparation for tomographic inversion

We used ProMAX® software for basic processing of the super gathers. After analyzing the spectral components of the gathers, we applied a variety of filters to enhance the signal-to-noise ratio. Specifically, we used spiking deconvolution, trace DC removal, and trace equalization before applying a 1-4-12-15 Hz Ormsby bandpass filter. Afterwards, we applied crooked line geometry and sorted the receivers in such a way that the new gather would have only the desired receivers for the given shot. The goal was to establish the best 3D coverage of the upper crust of the basin possible with the data available, and the processing flow used in ProMAX® is shown in Figure 2.4. We used 6 sources out of 15 and 524 receivers out of 1148 to generate 26 different shot gathers (Table 2.1). The position of the six sources and five different lines of receivers (G1, G2, G3, G4, and G5) are shown in Figure 2.5. We chose the source-receiver pairs in such a way to maximize ray coverage in the upper crust, and the idealized ray path

diagram for the chosen source-receiver pairs is shown in Figure 2.6. The 26 new gathers were exported as separate SEGY files for travel-time picking.

To read the newly generated SEGY gathers, "zp" was employed. The zp program (http://www.soest.hawaii.edu/users/bzelt/zp/zp.html) is a freely available routine used for plotting and picking seismic refraction data in SEGY format (Zelt and Smith, 1992). We applied bottom mute, bad trace editing, velocity reduction, and AGC (automatic gain control) to enhance the seismic data quality (Fig. 2.4). The first arrival zero crossing before peaks were picked and exported with the picking uncertainty values for all of the SEGY files. Figures 2.7a and 2.8a show some examples of the newly generated SEGY gathers for shot points 14 on line 1 and shot point 15 on line 3 respectively (Fig. 2.5) before applying any filtering. Figures 2.7b and 2.8b are examples of the corresponding SEGY gathers after applying filters, trace editing, and AGC in ProMAX® and zp. The first arrival picks are shown in red (Figs. 2.7b and 2.8b). The details of the source gathers, first arrival picks, and the picking uncertainties associated with these picks are summarized in Table 2.1.

Next, we used the fast marching tomographic modeling package (FMTOMO), a FORTRAN based program to perform 3D traveltime tomography and generated seismic velocity models in and around the Harney Basin area. FMTOMO uses a finite difference Eikonal solver and fast-marching method for travel-time prediction. It inverts the residual traveltime between the observed and calculated values for a given velocity model (De Kool et al., 2006; Rawlinson et al., 2006). This method is capable of using 3D model space and an initial 3D velocity model. The tomographic inversion is based on the iterative non-linear subspace inversion scheme, which is capable of adjusting

model parameters in order to satisfy the observed data (De Kool et al., 2006). However, local linearity is assumed in each of the inversion steps, and during the repetition of fast forward marching, the inversion allows for non-linear relationships between the velocity and traveltime perturbation (Rawlinson, 2007).

The FMTOMO uses several text files as input for tomographic inversion. The source related text file contains the latitude, longitude and the elevation information of the sources. The receivers related text file contains longitude, latitude, and elevation of the receivers. It also contains the traveltime picks and associated uncertainty values for these picks. A separate text file with velocity information is created, which contains the velocity values for given depth positions. The model space was set up between 42.5^0-44^0N latitude, 118^0 to 120.25^0W longitude, and 1.9 km above mean sea level (msl) to 15 km depth below the sea level. We used a two-interface model, with grid cell size of 5.2x4.6x0.85 km in the northing, easting and vertical directions respectively. We used 14 velocity nodes along depth (Table 2.2) with continuous velocity variation between these nodes. Source, receivers, and velocity related text files were used to run the forward and inverse modeling. For ray tracing purpose from source to receivers, the guided waves were used.

A checkerboard test for the model was performed to identify the solution robustness of the tomographic inversion. In the checkerboard test, a cell size of 9.5x7.25x1.40 km was used. The checkerboard test models contained 4224 cells. Figure 2.9 shows the results from a resolution test where we compared the initial velocity model before inversion and final velocity models after inversion. Figures 2.9a, c, and f are the initial velocity models at 3 km depth from msl, longitudinal slice at 119^0W

longitude, and a latitudinal slice at 43.60^0N latitude respectively. The final inverted results at the respective positions are shown in Figures 2.9b, d, and f. We observed that the solution is robust in and around the Harney Basin area up to a depth of ~10 km below mean sea level.

Seismic tomography

After the successful checkerboard test, we ran the forward and inverse model in FMTOMO. We used 17,280 propagation grid each with cell size of 2.6x2.3x0.55 km and 28,800 velocity grids each with the size of 5.2x4.6x0.85 km. A propagation grid is used by the waves to propagate from source to receivers whereas the velocity grids are based on the velocity models and the number of propagation grids within an interval. An initial velocity model and interface model were generated for the model space. At the same time, rays were traced with help of the fast forward marching diving waves from the given source to receiver pairs. An iterative inversion process was applied, which produced the inverted velocity models. The residual values (differences between the observed (picked) and modeled traveltimes) were analyzed to see the degree of convergence from the inversion result. If the convergence was not within a satisfactory margin, we ran another routine that separates outliers from the picks to be used. In this study, we set the outlier's threshold value at >0.5 s. Once the outliers are identified, they can either be corrected in the pick files or can be excluded for the next round of tomographic inversion. The process of forward and inverse modeling was repeated until satisfactory convergence values were obtained. The process and work flow to run the FMTOMO is shown in the flowchart in Figure 2.4.

We used seven iterations for inverting the model. The residual traveltime results obtained from the inversion are shown in Table 2.3. For the first six iterations, the solutions showed convergence, but in the seventh iteration, the solutions did not converge any further. The inversion results significantly improved the traveltime fit. The RMS traveltime residuals decreased by ~72% from 376.30 ms to 108.72 ms. The variance of the misfit decreased by ~84% whereas the χ^2-misfit values decreased by ~90% from 40.9780 to 3.9422.

Afterward, we used the Generic Mapping Tools (GMT) software package (http://gmt.soest.hawaii.edu/) to extract various 3D velocity slices, interface slices, and the traced ray points along the chosen latitudes, longitudes, and depths. The GMT generated data files were read in Python for visualization. Some example slices generated are shown in Figure 2.10. Figure 2.10a and b are the initial and final velocity slices at 3 km depth below msl. The actual position of sources and receivers are shown by yellow stars and white inverted triangles respectively in Figure 2.10a. In Figure 2.10b, the change in velocity at the given depth is observed where every 100^{th} ray point generated during the forward modeling process is shown. Figures 2.10c and d are the initial and final inverted velocity model at the longitudinal slice through 119^0W. Figure 2.10d shows the upper crustal velocity variation in the Harney Basin area is significant. Every 100^{th} ray point shown in the Figure is sampled from 119.0 $\pm 0.10^0$W longitude. Similarly, in Figures 2.10e and f, we show the initial and inverted velocity models at 43.60^0N latitude. The ray points shown in the Figure are sampled from 43.60 $\pm 0.10^0$N latitude. The inverted velocity models in these selected slices are examples of the

velocity information derived in the Harney Basin area, and the tomography results will be discussed further below.

Potential field data

In addition to the active source seismic data, we used gravity and magnetic data as part of our integrated geophysical interpretation process. The gravity and magnetic data for the whole continental US are freely available in the Pan American Center for Earth & Environmental Studies (PACES) websites (http://research.utep.edu/) (Keller et al., 2006). The state based gravity and magnetic data can be found in the US Geological Survey's database (http://pubs.usgs.gov/ds/355/). We also used digital elevation model (DEM), geological maps, fault databases, aerial photos, and tectonic maps of the area as controls for the integrated interpretation (Fig. 2.4). In addition to these databases, additional gravity data were collected in and around the Harney Basin in 2008 and 2012. The details of the gravity data collection, corrections applied and processing techniques are shown in Table 2.4 and discussed below.

Gravity data collection and preparation

In August 2012, 998 gravity points were collected with average station spacing of ~1.5 km in and around the Harney Basin area. Three gravimeters (two SCINTREX CG5 AUTOGRAV and a LaCoste & Romberg) and students from three different universities collected these data over three weeks. Similarly, 271 gravity data points were collected in 2008 in the same area using LaCoste and Romberg (L&R) meter. We used differential GPS data from TOPCOn® and Leica® systems to obtain the spatial coordinates and elevations of the gravity stations with sub-meter accuracy of ~30 cm in vertical direction and 10 cm in horizontal directions.

The differential GPS data were processed with the help of Online Positioning Users Service (OPUS), an online GPS data processing website affiliated with the National Geodetic Survey (https://www.ngs.noaa.gov/OPUS/) and were tied to the corresponding gravity stations. We applied drift correction to all of these data. The gravity data collected with L&R meter were first calibrated using an instrument specific dial correction. Then the drift and earth tide corrections were applied. The tide correction is not necessary for the gravity data collected using CG5 gravimeters because these instruments have built-in tide correction programs. These drift and tide corrected data were tied with the local gravity base stations at Burns, Oregon to obtain the absolute gravity values for total of 1269 gravity stations.

We used gravity reduction spreadsheet (Holom and Oldow, 2007) to obtain the standardized free air and Bouguer anomaly values for these stations. The complete Bouguer anomaly (CBA) values for these stations were obtained after applying terrain correction to the data in Geosoft® software and adding the terrain results to the Bouguer anomaly values. These data were merged with the PACES database in the area between 42.0^0-44.5^0N latitudes and 116.5^0-120.5^0W longitudes. The merged dataset contains 6654 gravity stations in total.

Gravity mapping

After the data preparation, we use a 2 km grid spacing to generate a CBA gravity map of the area (Figure 2.11). The black dots in the map represent new gravity data points collected in 2008 and 2012 whereas the white dots are the station from the PACES database. The physiographic boundary (we manually derived from the digital elevation map) of the Harney Basin is shown by the yellow polygon. The newly

collected data are mostly from the Harney Basin, Diamond Craters, and Steens Mountain areas. The anomaly values across the region vary by ~90 mGal. Key tectonic units in the area such as the Western Snake River Plain, High Lava Plains, Steens Mountains, Owyhee Plateau, and the Blue Mountains are easily identified in the resulting map.

In order to focus on the Harney Basin, the study area was reduced the area that surrounds the physiographic Harney Basin and a new CBA grid of the area was generated. A series of wavelength and edge-detecting filters were applied in the frequency domain using fast Fourier transform (FFT) techniques. Figure 2.12a shows the CBA map of the Harney Basin area. The CBA anomaly varies by about ~50 mGal with lowest values in the Steens Mountain area. A semi-circular gravity low is observed in the northeast corner of the basin, and is possibly the signature of a caldera. The Diamond Craters area is also located in a gravity low. Figure 2.12b is a tilt derivative of the CBA map in the area. The tilt derivative filter helped enhance the edges of major features such as possible craters and calderas in the Harney Basin. Besides that, this filter helped to enhance subtle features in the Steens Mountain area. A circular shaped feature, possibly a buried crater or caldera rim, of ~8 km diameter is clearly visible. This previously unnoticed feature could be one of the eruptive centers for the Steens Basalt. The edges of the possible calderas and Diamond Craters are also enhanced. We also applied an upward continuation filter to the CBA grid, and generated a 15 km residual CBA map of the Harney Basin area as shown in Figure 2.13. The anomaly varies by ~25 mGal in the area. The black lines are the mapped Quaternary surface

faults. Gravity models across the basin along XX′, YY′, and ZZ′ were generated and discussed below.

Magnetic data processing

The USGS state magnetic databases for Oregon and Idaho from the USGS data repository were employed for magnetic data analysis. The details of the data acquisition, survey parameters, and processing applied to these grids are available in the USGS data repository webpage (http://pubs.usgs.gov/ds/355/). We merged these two grids and produced the reduced-to-pole total magnetic intensity (TMI) map of the area shown in Figure 2.14a. The TMI values vary over a range of ~800 nT. Black lines represent the mapped Quaternary faults in the area. The key tectonic components such as the HLP, WSRP, accreted terranes of the Blue Mountains, Steens Mountain, and the Steens Dikes are identified and shown (Fig. 2.14a). The E-W trending streaks observed are the artifacts due to survey boundaries. We confined our study area around the Harney Basin (42.5^0N-44^0N and 118^0W-120.25^0W). The reduced-to-pole TMI map of the Harney Basin area is shown in Figure 2.14b. In the northeast corner of the Harney Basin, we observed the low magnetic semi-circular anomaly that aligns with the low gravity anomaly in the same area as shown in Figure 2.12. The shape of this anomaly indicates the presence of caldera features, but due to the geological complexity in the area and uncertainty of the magnetic polarity signatures, we did not strongly depend on the magnetic data to interpret shallower features. However, the magnetic data helped us for the completeness of integrated geophysical interpretation. The northern Steens Mountain area is associated with a N-S trending linear magnetic high, which is probably related to the Steens Dikes.

Discussion of the results

After analyzing the results obtained from different geophysical and geological datasets, we present our integrated discussion of the subsurface structures and evolution of the upper crustal features in the Harney Basin area.

Seismic tomographic results

The seismic tomography results successfully imaged the upper crustal features of the area to ~8 km depth from msl. Figure 2.15 shows the inverted velocity models of the Harney Basin area along longitudinal slices. The upper layer basin fill has a velocity of ~3-3.5 km/s and is about 1.5 km thick in the central area whereas the whole basin is ~6 km deep from msl in the central area. The basin shallows rapidly outward on its western side. On the east, the longitudinal slice 118.60^0W shows that the basin thickens to ~5 km from msl in a narrow area that extends to the SE.

A series of latitudinal slices are shown in Figure 2.16. The basin thickness reaches to ~5 km in the central area and is shallower outward to the south and north. Figure 2.17 shows the depth slices ranging from 2 km to 7 km from msl. The velocity normally ranges from about 5 km/s at about 2 km depth to about 6.3 km/s at the depth of 7 km. The first two layers (yellow and green) represent sedimentary fill and widespread tuffs deposits. The third layer (blue) from top is most probably the volcanic rocks (basalt, rhyolites, andesites, and tuffs that form the bottom of the basin. Near the central part of Harney Basin (119^0W longitude and 43.3^0N latitude), we observed an anomalously high velocity (>6.5 km/s) body (bright pink color) at ~5.5 km depth from msl. This body can be observed in the latitudinal, longitudinal, and depth slices (Figs. 2.15, 2.16, and 2.17). It lies close to the Diamond Craters beneath the Harney Lake and

Mud Lake and is about (25x20x1.5) km^3 in size. We interpret this feature as an intrusive body associated with the low–K, high Al, olivine tholeiite (HAOT) basalts in the Diamond Craters discussed by Hart et al. (1984) and Hart (1985). The velocity of >6.5 km/s for this body, at the given depth for HAOT basalt is in the suitable range as suggested by Song (1997) from their lab experiments.

Gravity models across the basin

We modeled three gridded gravity profiles across the Harney Basin namely, XX′, YY′, and ZZ′ as shown by dashed white lines in Figure 2.13, to explore the upper crustal features in the Harney Basin area. The seismic velocity model generated by tomographic inversion along these profiles, surface geology, and the geospatial information are used as the key basis for the gravity models. To find the density (ρ) of the modeled units, we used the relation between P-wave velocity (Vp) and density postulated by the Nafe-Drake curve and given by Brocher's relation (2005):

$$\rho(g/cm^3) = 1.6612V_P - 0.4721V_p^2 + 0.0671V_p^3 - 0.0043V_p^4 + 0.0000106V_p^5$$

All of these profiles are modeled to a depth of 15 km. Figure 2.18 is a gravity model along X-X′ (43.25^0N latitude). The upper two layers with density ranging from 2.43 to 2.54 g/cm^3 are the Quaternary sediments with occasional ash flow, tuffs, and flood basalt. These layers reach as deep as ~3 km from msl. The third and the fourth layers with density of 2.64 and 2.69 g/cm^3 are mostly mixed lithologies of flood basalt, rhyolites, and sedimentary units. The fourth layer is modeled as deep as 8 km and is interpreted to be the crystalline basement. Beneath the Harney Lake area, at ~7 km depth, we modeled a body with density of 2.79 g/cm^3. We interpret this body as possible residual magma from the conduit that created the Diamond Craters and

possibly consists of HAOT type basalt. A horst block related to the Brothers fault zone is also modeled.

Figure 2.19 is a gravity model along Y-Y′ (43.60^0 N latitude). This line passes through a caldera shaped feature (Figure 2.13) in the eastern portion of the model. This area is covered by a thick upper layer with a density of 2.43 g/cm^3. The caldera feature reaches as deep as ~4 km from msl. In the area at about 8 km depth, we modeled a body with density of 2.79 g/cm^3. This body is possibly a high-density alkaline basalt intrusion.

Figure 2.20 is a density model along Z-Z′ in Figure 2.13 (118.80^0W longitude). This line crosses two interpreted calderas, a northern caldera in the northeast Harney Basin and a southern caldera to the west of Diamond Craters (Fig. 2.13) and are as deep as ~5 km from msl. These interpreted calderas are separated by a gravity high anomaly near Harney and Malheur Lakes. This gravity high is caused by a high-density (2.78 g/cm^3) mafic body at about the depth of ~4 km from msl. These gravity models show the extent of the Harney Basin and match approximately with the results from the seismic tomographic models. The magnetic profiles in Figures 2.18, 2.19, and 2.20 mostly match with the modeled subsurface lithologies.

Based on these geophysical results and geological observations, we present additional evidence in support of the caldera interpretations. The presence of voluminous Late Miocene (10-5 Ma) Rattlesnake Tuffs, Devine Canyon Tuffs, Prater Creek Tuffs and other numerous smaller tuffs deposits in the area raise a questions, where do these tuff and ash flow deposits come from? Their source has to be somewhere close by these deposits. The circular to semi-circular topographic low

features and the abundance of tuffaceous deposits, ash-flow, scoria, and rhyolites makes Harney Basin a suitable place to contain the sources of these deposits. Previous researchers have also interpreted that the sources of these tuffaceous deposits are within the Harney Basin (e.g. Parker, 1974; Walker, 1974; 1979; Macleod et al., 1976; Walker and Nolf, 1981, Streck and Grunder, 1995; 2008, 2012; Ford et al., 2013). The source locations of the tuffs were based on the degree of welding, the changing thickness of the tuffs, decrease in pumice size, and rheomorphic features. After the large volume of the material erupted, the bimodal magmatism and sedimentation continued in the area increasing the surface load. This must have lead to the gradual subsidence of the basin forming calderas in the area. The presence of hot springs in the center of the basin can yet be seen as other evidence for presence of calderas. When combined with this geologic information, we conclude that the gravity and seismic tomographic data from our study strongly suggests the presence of calderas in the area.

Integrated geophysical interpretation

The gravity anomalies represent density variations of subsurface bodies and thus have a direct relation with the P-wave velocities. In order to understand the relationships between the observed gravity and magnetic anomalies and the velocity model, we generated a series of 3D block diagrams. Figure 2.21 illustrates a 15 km upward continued residual Bouguer anomaly map on the top and a seismic velocity slice through 119.0^{0}W longitude in the cross-sectional view. The physiographic boundary of the Harney Basin is shown by the yellow polygon, and its southern boundary is associated with an upwarp of high velocity values that indicates a structural boundary. We observed a high velocity (>6.5 km/s) body near the center of vertical

slice at about a depth of 5 km below msl. This feature coincides with a gravity high anomaly (G_1; in Fig. 2.21) in the Harney Basin beneath the Mud Lake and Harney Lake area. The northern part of the basin has lower gravity values, which coincides with the thicker post-caldera basin fill deposits shown by the dashed black lines in Figure 2.21. The dashed white line is the base of the subsided basin that formed the base of caldera

Figure 2.22 is another block diagram with 15 km upward continued residual Bouguer anomaly map on the top and a seismic velocity slice through 43.10^0N latitude in the cross-sectional view. In map view, the physiographic Harney Basin boundary is shown by a yellow polygon. We observed two circular gravity lows. The shape of these features resembles that of calderas in other volcanic provinces. We refer to these calderas as the northern caldera and the southern caldera hereafter (Fig. 2.22). The northern caldera has dimensions of ~50 km in E-W and ~25 km in N-S, whereas the southern one is ~25 km in E-W and ~10 km in N-S. We also observed a high velocity anomaly at ~4 km depth beneath the Diamond Craters area indicating the presence of a mafic intrusion.

Figure 2.23 is another block diagram showing the 15 km upward continued reduced-to-pole total magnetic intensity map in the top view with a juxtaposition of 119.0^0 W longitude velocity slice in the sectional view. The Quaternary Brothers fault zone is also shown in the top view. The Harney Basin shows relatively coherent magnetic signatures in comparison to the surrounding area. The magnetic high marked by M_1 (Fig. 2.23) is associated with the high velocity anomalous body seen in the cross-sectional view at about the depth of ~5 km. This feature is close to the Harney and Mud

Lake area in the central part of the basin and coincides with gravity high (G_1) as shown in Figure 2.21.

For a detailed integrated geophysical interpretation within the Harney Basin, we compared the results from gravity, seismic data, and DEM as well as magnetic data as shown in Figure 2.24. Figure 2.24a, b, c, and d are a 15 km residual Bouguer anomaly map, a 15 km upward continued residual RTP TMI map, a 10 m resolution DEM map, and a seismic velocity slice at 4 km depth from msl respectively. The black dots in Figure 2.24a are the gravity stations and white polygons in Figures 2.24a, b and c are the physiographic boundary of Harney Basin drawn based on 10 m resolution DEM map (Fig. 2.24c). The residual gravity anomaly map in (a) shows two semi-circular negative gravity lows bounded by highs that are interpreted as the northern and the southern caldera as shown by dashed yellow and white polygons respectively. These calderas possess anomalously low seismic velocity, lies on low topography, as well as have low negative magnetic anomalies, (Figs. b, c, and d). These data support the caldera interpretation. We interpret the NW-SE trending linear gravity high (Fig. a), a magnetic high (Fig. b) and a linear velocity high (Fig. d) shown by a pair of black arrows as indicating the presence of mafic dikes. The trend of this feature is close to that of the Brothers fault zone. We interpret this feature as one of the possible sources for magmatic activity in the Harney Basin area and as an axis of the igneous Harney Basin province.

In order to investigate the caldera features and some anomalously high gravity and magnetic features in the central area of the basin, we further subdivided the basin into three different areas. These areas are described in the following sections.

Diamond Craters and southern caldera

The Diamond Craters is a basaltic lava flow of the Late Pleistocene to recent age that lies in southern part of the Harney Basin and covers ~60 km^2 areas (Piper et al., 1939; Peterson and Groh, 1964). The eruption was caused by deep fissures produced in the earth's crust, and the olivine rich lava made its way to the surface. Due to multiple and complex volcanic activity in the area, the sources of these volcanoes are hard to determine and are believed to be beneath the central crater area (Peterson and Groh, 1964). We used gravity, magnetic, seismic, and DEM data for detailed integrated geophysical interpretation of the area and show the results in Figure 2.25. Figure 2.25a is a residual Bouguer anomaly map of the area draped on a 10 m resolution DEM map. The Diamond Craters location is shown by a red dotted polygon that lacks positive gravity anomalies. To the west of the Diamond Craters, we observe a significant gravity low with a semi-circular shape shown by the dotted yellow polygon. We plotted the seismic velocity slices at 4 km depth from msl, a longitudinal slice through 118.90^0 W longitude, and a latitudinal slice through 43.10^0 N latitude as shown in Figures 2.25b, c, and d respectively. The low velocity basin fills reach as deep as ~4.5 km from msl in the area indicating the presence of a caldera. This interpretation is also supported by the topographic features, surface geology, and magnetic data (Figs. 2.17 and 2.24b). We propose this caldera to be the possible source for 9.7 Ma old Devine Canyon Tuffs. The source location is close to one proposed by Greene (1973) and Walker (1974; 1979). Beneath the caldera, we observed ~1 km thick high velocity body at depth of ~6 km. This is possibly the residual source material of the Diamond Craters volcanoes.

Based on these results, we propose a three-stage evolution of the Diamond Craters and southern caldera area. At about 10-8 Ma the area was covered with active felsic volcanism (e.g. Walker, 1979; Christiansen and Yeats, 1992; Jordan, 2002). Due to extensive volcanism and overloading in the crust, the volcanic center subsided and the southern caldera formed. The caldera was later filled by basin sediments, tuffaceous deposits, and ash-flows. Later, due to the faulting in the Brothers fault zone, the olivine rich basaltic magma that formed in the lower crust to the upper mantle (Russell and Nicholls, 1987) rose along these fissures. During the Pleistocene, this magma made its way to the surface in the eastern portion of the caldera and the Diamond Craters were formed. Some of the residual magma might have solidified in the upper crust at about ~6 km depth in the nearby area. Meanwhile the sedimentation and volcanism continued to form the present day landscape in the area forming a buried caldera beneath the Diamond Craters.

The central lake area

The lowest elevation in the Harney Basin lies in the central portion. This part is occupied by Malheur Lake in the eastern side, the relatively small Mud Lake in the center, and Harney Lake in the western side. This area contains Miocene tuffs, basaltic flows, ash-flow tuffs, and an abundance of locally fluviatile sedimentary and volcanic rocks with high P_H (acidic scale) values (Sheppard, 1994). Although separated by only few hundred meters of flat-lying land, Harney Lake has high salinity water whereas the other two lakes are fresh water. The gravity and magnetic signatures in the area are anomalously high and these anomalies separate the northern caldera from the Diamond

Craters and southern caldera area. For detailed study, we analyzed the gravity, magnetic, and seismic data of the area and show the results in Figure 2.26.

Figure 2.26a is a residual Bouguer gravity map after applying 15 km upward continued filter draped on a 10 m resolution DEM map. We observed a relatively high gravity anomaly in the low-lying lake area as shown by the dotted yellow polygon. The same areas also show high positive magnetic anomalies (Figs. 2.17 and 2.24b). Figures 2.26b, c, and d are the seismic velocity slices at 4 km depth from msl, a longitudinal slice at 119^0 W longitude, and a latitudinal slice at 43.25^0 N latitude respectively. From the seismic data, we observed that the basin deposit thickness ranges from about 2.5-4 km from msl in the area. A high seismic velocity body lies at ~5-6 km depth as seen in Figures c and d. The presence of high gravity and magnetic anomalies and presence of a high velocity zone can be inferred to the presence of some intermediate-mafic body in the upper crust. Some of the sources for Harney Lake water are hot springs that lie on the southeast side of the lake. The spring water dissolves and carries alkaline minerals with it from the subsurface (Sheppard, 1994). This is one of the reasons for high salinity water in Harney Lake.

The northern caldera

The northern caldera lies in the northeast corner of the Harney Basin and covers the northern half of Malheur Lake. It is bounded to the north and east by topographic highs. The west and south sides are somewhat flat topographically. The area is covered by fluvial, fluvio-lacustrine, and volcanic sediments.

We analyzed the gravity, magnetic, DEM, and seismic data of the area for detailed study. Figure 2.27a shows the 15 km upward continued residual Bouguer

anomaly draped over a 10 m DEM map. The caldera boundary is delineated with the dotted yellow polygon. The caldera is semi-circular in shape with dimensions of ~50 km in east-west direction and ~30 km in north south direction. Within the northern caldera, we can see two distinct depressions shown by C1 and C2 (Fig. 2.27a). They are separated by a moderate linear gravity feature (Fig. 2.12b). This is probably due to the nested calderas features as suggested by Kane et al., (1976) for the Long Valley caldera area and by Cole et al., (2005) for Masaya caldera in Nicaragua.

Figures 2.27 c and d are seismic velocity slices at 4 km depth from msl, a longitudinal slice at 118.90 ^{0}W longitude and a latitudinal slice at 43.55 ^{0}N latitude. The low velocity material has thickness of ~4-5 km (Figs. c and d). This indicates the sediments and volcanic material filled the caldera after it was formed. Thus, the surface geology, topographic features, and geophysical data suggest the presence of caldera in the area. Greene (1973); Walker (1974) and Ford et. al. (2013) also suggested the source of the 8.4 Ma old Prater Creek Tuffs in the same area.

In magnetic maps of the area, we observed that C1 has low negative magnetic anomaly but C2 correlates with high positive magnetic anomalies (Figs. 2.17 and 2.24b). The higher magnetic anomaly of C2 could be somehow related to the reactivation of the caldera in the area. This could be the result of asymmetrical tilting of the nested caldera features while it subsided. The eastern rim of the C2 caldera might have been tilted and rotated instead of collapsing during the caldera formation. The analogy can be drawn from the tilted nested caldera complex in Hong Kong as suggested by Sewell et al., (2012).

Conclusions

Using 2D seismic lines to generate a 3D seismic tomographic model of upper crustal structure in the Harney Basin area produced useful and intuitive results. The 2D line geometry sources and their pairing with the off-line receivers created multiple fan shots for each source. This approach helped to scan the upper crust several times for most of the basin and optimized 3D tomographic results. We successfully delineated the upper crustal features and identified two major calderas in the basin.

Seismic tomography, gravity and magnetic maps, integrated gravity models, surface geology, and other geospatial data were combined to interpret the major structural components in the Harney Basin area. This cross validates the seismic tomographic interpretation. Newly added gravity data revealed some previously unseen features such as a buried crater or caldera in the northwest part of Steens Mountain. The integrated geophysical approach helped to image the detailed upper crustal features of the Harney Basin area down to a depth of ~8 km below mean sea level.

Previous researchers interpreted the presence of calderas in the area (e.g. Greene, 1973; Walker 1979; Walker and Nolf, 1981; Streck and Grunder, 1995; 2008, Ford et al., 2013) but lacked detailed geophysical data to support their hypotheses. The new integrated geophysical results helped us to identify two caldera complexes within the Harney Basin, namely the southern and northern caldera. The mechanism of the caldera formation is complex because of the multi-phase bimodal volcanism and hard to decipher in detail due to thick sedimentation. One possible mechanism can be the downward flexure or downward sagging (Roche et al., 2000). This is supported by the center ward increase in the dip angle of the tuff beds in the northern Harney Basin.

(Ford et al., 2013). The lack of ring faults in the area can be credited to the thick sedimentary deposits and volcanic fill that might have covered many faults. The mechanism and process of caldera formation such as “downsagging”, “piecemeal”, or both could also cause the lack of ring faults (Cole et al., 2005). However, the presence of hot springs and geothermal activity (Cole et al., 2005) in the area is one of line of evidence that supports our interpretation for the presence of calderas. The presence of tuff deposits and numerous ash flows within the Harney Basin is additional evidence to support our interpretation. The complexity of the caldera shape and features suggests that there is no single end member mechanism for the caldera-forming processes.

One can argue the alternative interpretation to the presence of caldera such as; thick basin fill or the presence of a silicic batholith or both that can contribute to the low gravity values and seismic velocities as well as magnetic signatures. We ruled out these interpretations solely based on the findings from previous research and our study. Although sparsely available, the drilling data suggests the sediment fill in the basin in not more than few hundred of meters. We do not see any evidence of the Basin and Range structures such as fault bounded grabens and significant extension. There is no evidence for present or paleo-fluvial systems that could make Harney a fluvial basin. The presence of unusually high density and seismic velocity material in shallow crust, absence of granitic rocks in the vicinity, presence of higher magnetic materials in the caldera area indicates the absence of granitic plutons in the area. The presence of abundant rhyolite can raise the question related to its source. Based on the research on the Rattlesnake Tuffs, these rhyolite and tuffs deposits are rich in iron and silica content, have high parent magma temperatures (>880^0C), and have high Ba/Sr ratios

(e.g. Streck and Grunder, 1995; 2008; 2012; Ford et al., 2013). These indicate that the sources of these deposits were mafic and fractional crystallization created this large volume of tuffs and rhyolite deposits, thus ruling out the possibility of presence of silicic plutons.

To strengthen the proposed geophysical interpretation, more data from the scientific drilling of these caldera complexes would be ideal and a detailed 3D seismic study of the area would be helpful. Such efforts would help us to further understand the complex evolution of the upper crustal features and calderas within the Harney Basin.

Acknowledgements

We would like to thank Travis Fultz and Mark Larson from Missouri State University, Nick Mueller and Calvin Nix from UT, Dallas, Stephan Holloway, Kevin Crain, Jefferson Chang, Vikram Jayaram, Gaurang Patel, Rachel Yates, and Sam Martin from OU for helping to collect gravity data in the field. We are grateful to Dr. Nick Rawlinson for proving us with useful insight in the use of FMTOMO and interpretation of some results. We thank Dr. Anita Grunder for her insightful suggestions on regard to our interpretations. Our special thanks go to Christopher Toth, Xiao Xu, and Cullen Hogan for helping us in setting up and using FMTOMO, GMT, and Python programs. This project was funded by a NSF grant.

Shot points	Gathers	No. of receivers	No. of first arrival picks	Average picking uncertainties (ms)
sp13	G1	80	79	0.0708
	G2	137	99	0.0849
	G4	113	62	0.0861
sp14	G1	80	78	0.075
	G2	137	128	0.0396
	G3	107	103	0.0270
	G4	113	105	0.029
	G5	87	80	0.0306
sp15	G2	137	94	0.062
	G3	107	102	0.0646
	G4	113	104	0.0547
	G5	87	83	0.0552
sp24	G1	80	77	0.05649
	G2	137	129	0.07282
	G3	107	100	0.06725
	G4	113	107	0.0549
	G5	87	78	0.0572
sp26	G1	80	77	0.0509
	G2	137	111	0.0725
	G3	107	79	0.0503
	G4	113	110	0.0678
	G5	87	33	0.0783
sp31	G2	137	71	0.0623
	G3	107	59	0.0616
	G4	113	101	0.0589
	G5	87	64	0.0569
Total	26	2790	2313	

Table 2.1: Table showing the combination of source-receiver geometry chosen from the High Lava Plains active seismic experiment, 2008. The number of first arrival picks and their associated picking average uncertainties used for tomographic inversion are also shown.

Velocity interfaces	Depth (km)	P-wave velocity (km/s)
1	2.5	3.00
2	-0	3.51
3	-0.5	3.64
4	-1.51	3.76
5	-1.5	5.37
6	-2.5	5.44
7	-3.0	5.49
8	-3.1	6.1
9	-4.15	6.11
10	-7.3	6.14
11	-11	6.17
12	-14.10	6.42
13	-16.21	6.49
14	-21.0	6.74

Table 2.2: Velocity nodes along depth, used for generating initial velocity grids with -ve depth indicating below mean sea level.

Number of Iterations	RMS traveltime residuals (ms)	Variance of the misfit	χ^2- misfits
Initial values	376.30	0.07637	40.9780
1	147.22	0.02168	6.8681
2	118.47	0.01404	4.6739
3	116.52	0.01358	4.4913
4	110.54	0.01222	4.0944
5	110.44	0.01220	4.0832
6	**108.72**	**0.01182**	**3.9422**
7	110.89	0.01230	4.0120

Table 2.3: Results obtained from the iterative tomographic inversion from the FMTOMO program. After the sixth iteration, the convergence does not improve any further.

Data (survey) type	Gravimeter used	Differential GPS system used	Number of gravity stations	Applied gravity corrections				
				Drift	Earth tide	Free air	Bouguer	Terrain
Oregon 2012	SCINTRESX CG5 (UTD)	Leica®	102	Spread sheet	Instrument applied	Spread sheet	Spread sheet	Geosoft®
	SCINTREX CG5 (OU)	TOPCOn®	413	Spread sheet	Instrument applied	Spread sheet	Spread sheet	Geosoft®
	LaCoste & Romberg meter	TOPCOn®	483	Spread sheet	Earthtide in MATLAB®	Spread sheet	Spread sheet	Geosoft®
Oregon 2008	LaCoste & Romberg meter	TOPCOn®	271	Spread sheet	Earthtide in MATLAB®	Spread sheet	Spread sheet	Geosoft®
PACES	N/A	N/A	5385	N/A	N/A	N/A	N/A	N/A
Total			6654					

Table 2.4: Instruments used to collect gravity data and the processing applied to them in various programs and software.

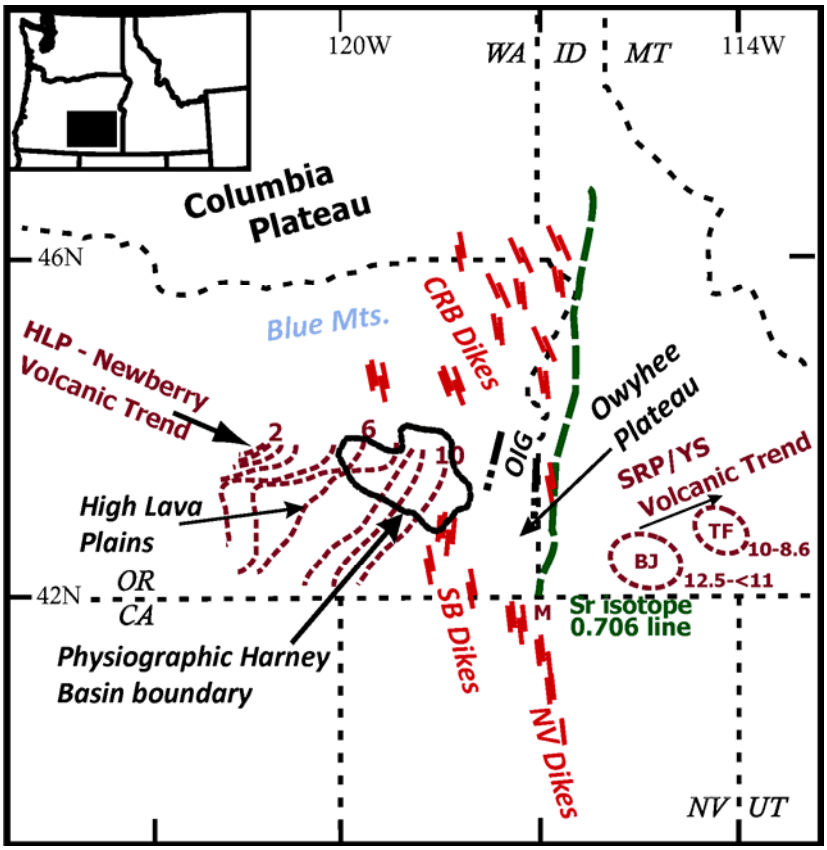

Figure 2.1: Index map of the study area showing major tectonic units around the High Lava Plains (HLP) modified after Brueseke et al (2007); Benford et al. (2010); and Cox (2011). The Harney Basin (black polygon) is one of the major features in the HLP and lies along the HLP-Newberry volcanic trend. The SR/YS (Snake River/Yellowstone) volcanic track contains the Bruneau-Jarbidge (BJ) and Twin Falls (TF) volcanic fields. The HLP is bounded to the north by the Blue Mountains and the Columbia Plateau, to the east by the Columbia River Basalt (CRB), Steens Basalt (SB), and Northern Nevada (NV) feeder dikes (rift). The 0.706 Sr isotope line (green) separates cratonal North America to the east from the accreted terranes to the west. The Oregon-Idaho graben (OIG) and Owyhee Plateau are also shown.

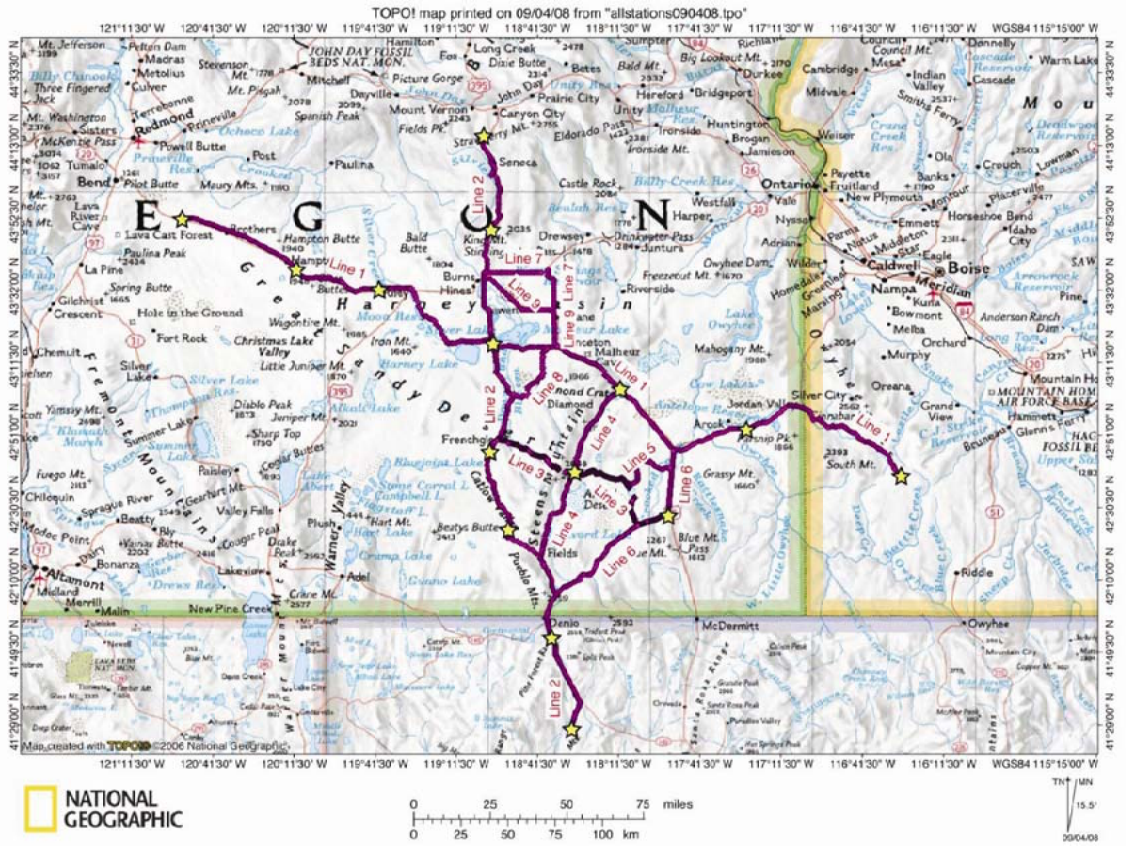

Figure 2.2: Experimental layout for the High Lava Plains active seismic project conducted in September 2008. Yellow stars represent source locations whereas the purple and blacks dots are the receiver locations. 15 shots (1 ton each), 2612 Texans recording geophones, and 120 RefTEK130 receivers were deployed in this survey.

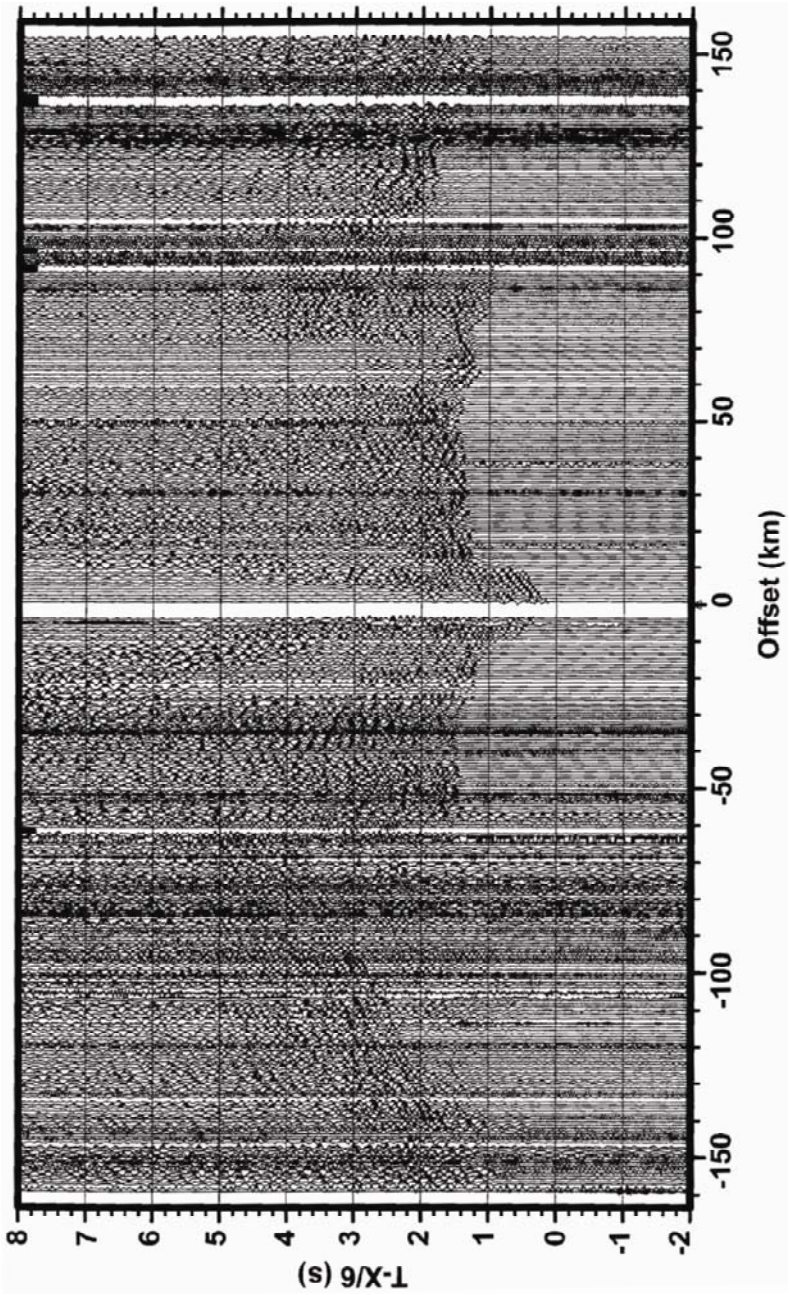

Figure 2.3: An example of the raw super-shot gather for shot point 24 from the High Lava Plains seismic experiment.

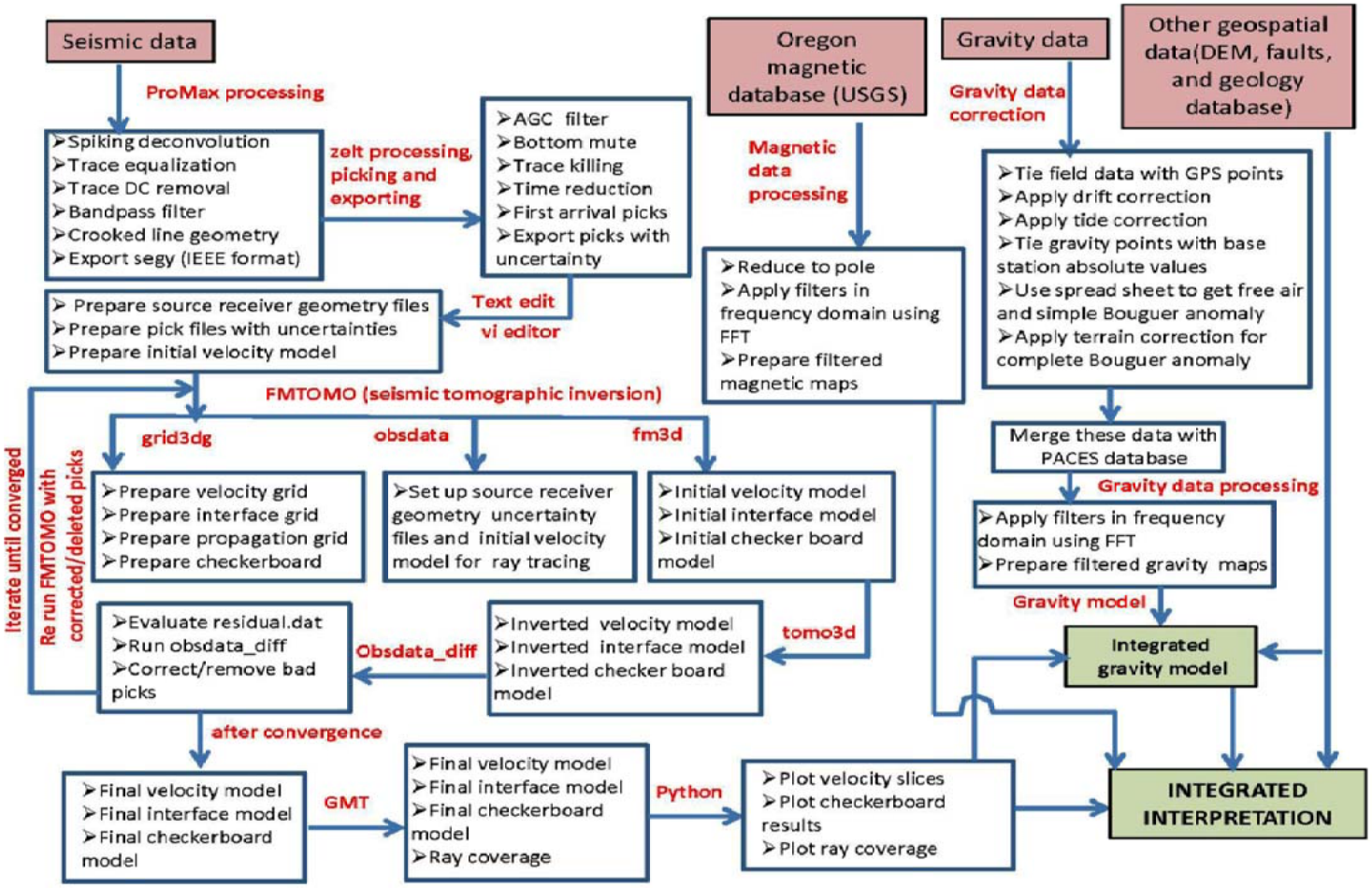

Figure 2.4: Flowchart used for this integrated geophysical interpretation of the Harney Basin region.

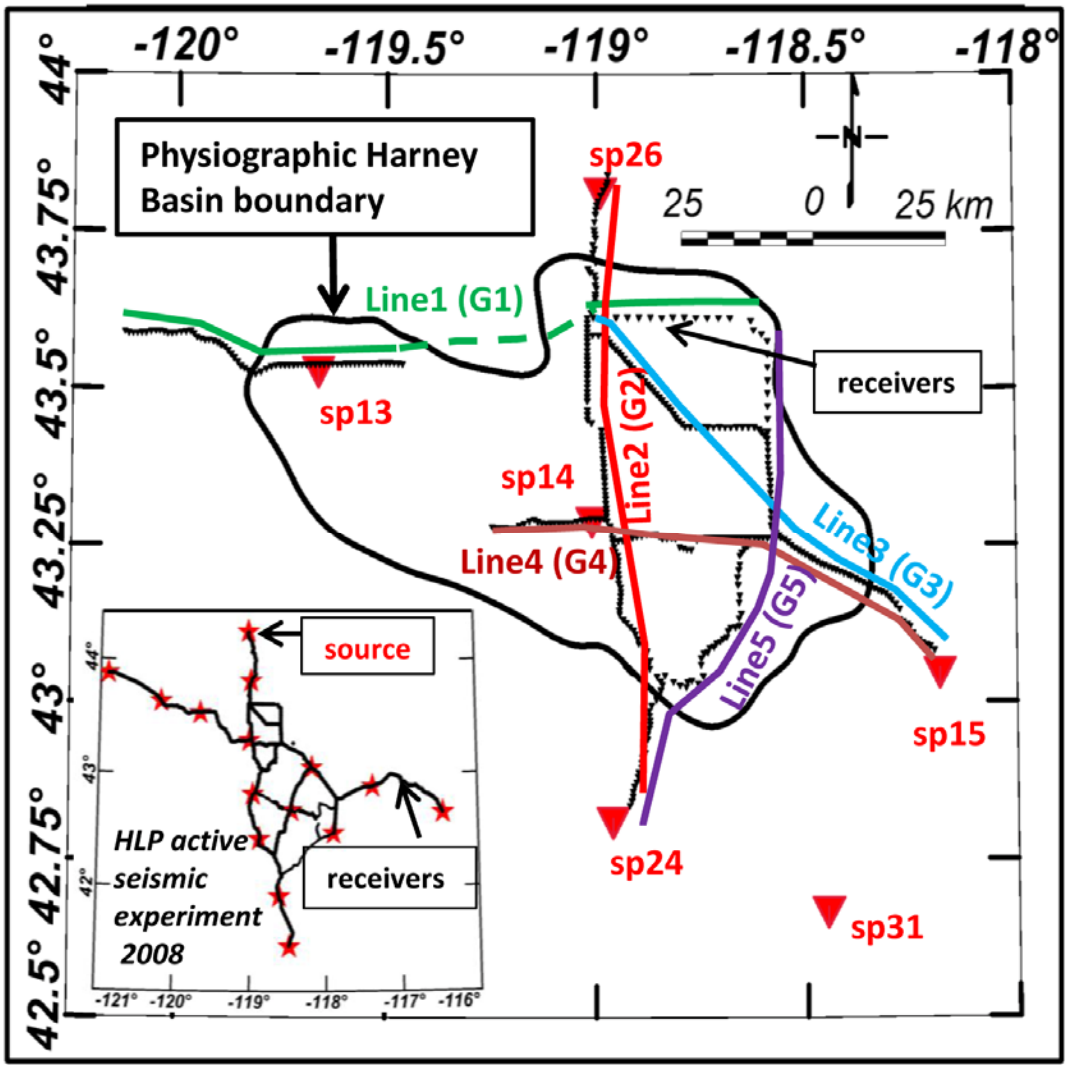

Figure 2.5: Seismic index map showing source receiver geometry chosen from the larger HLP seismic experiment, 2008 (shown in inset map). For region of this study, 6 sources and 5 different lines of receivers (524 receivers) were chosen in such a way that most of the Harney Basin area has ray coverage. Table 1 shows the details of the source-receiver pair geometry.

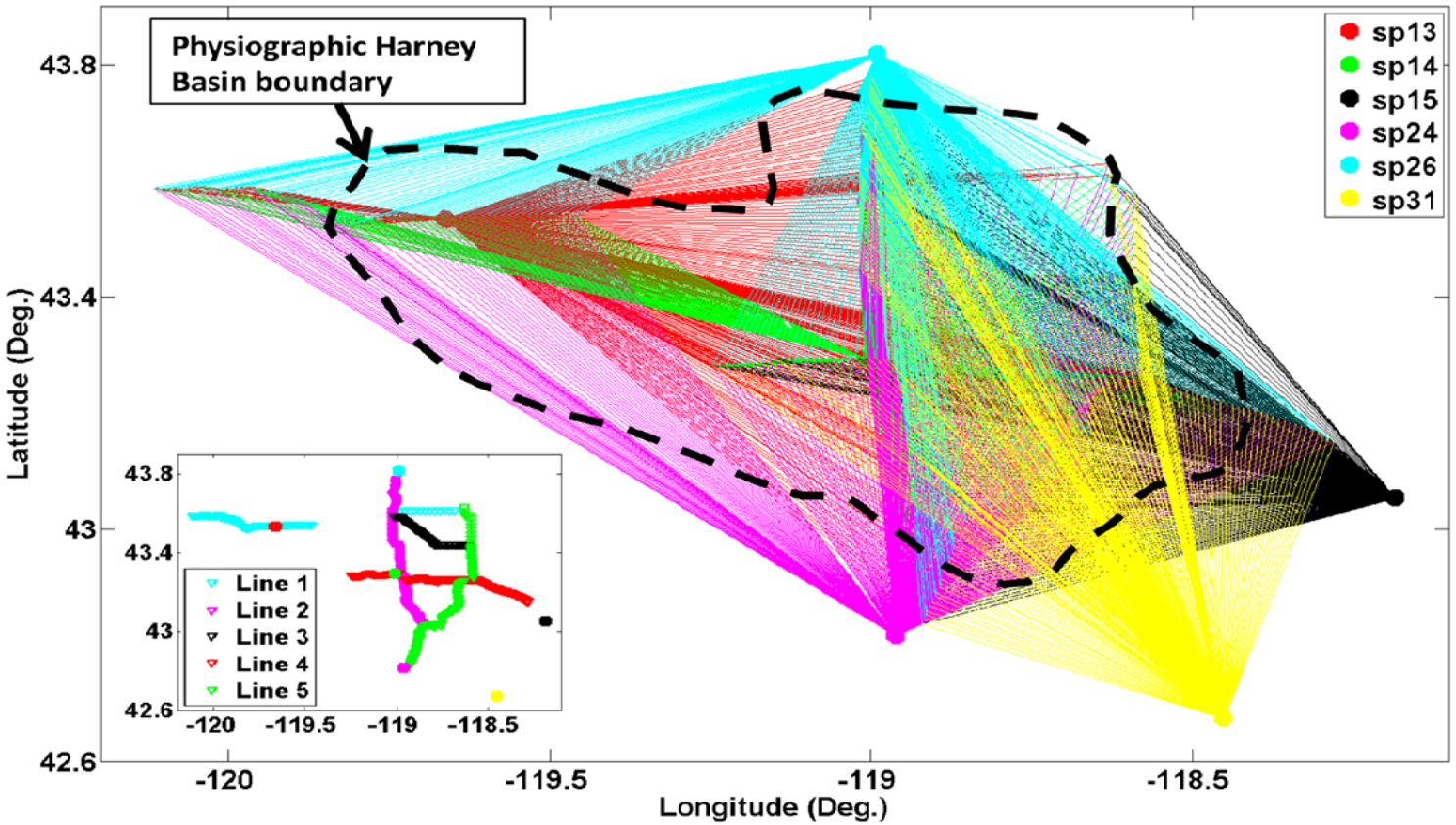

Figure 2.6: Idealized areal ray coverage map from the chosen source-receiver geometry. Inset Figure shows source receiver positions. In the ideal case, the rays from these sources to the receiver pairs cover most of the Harney Basin area as shown by a dashed black polygon.

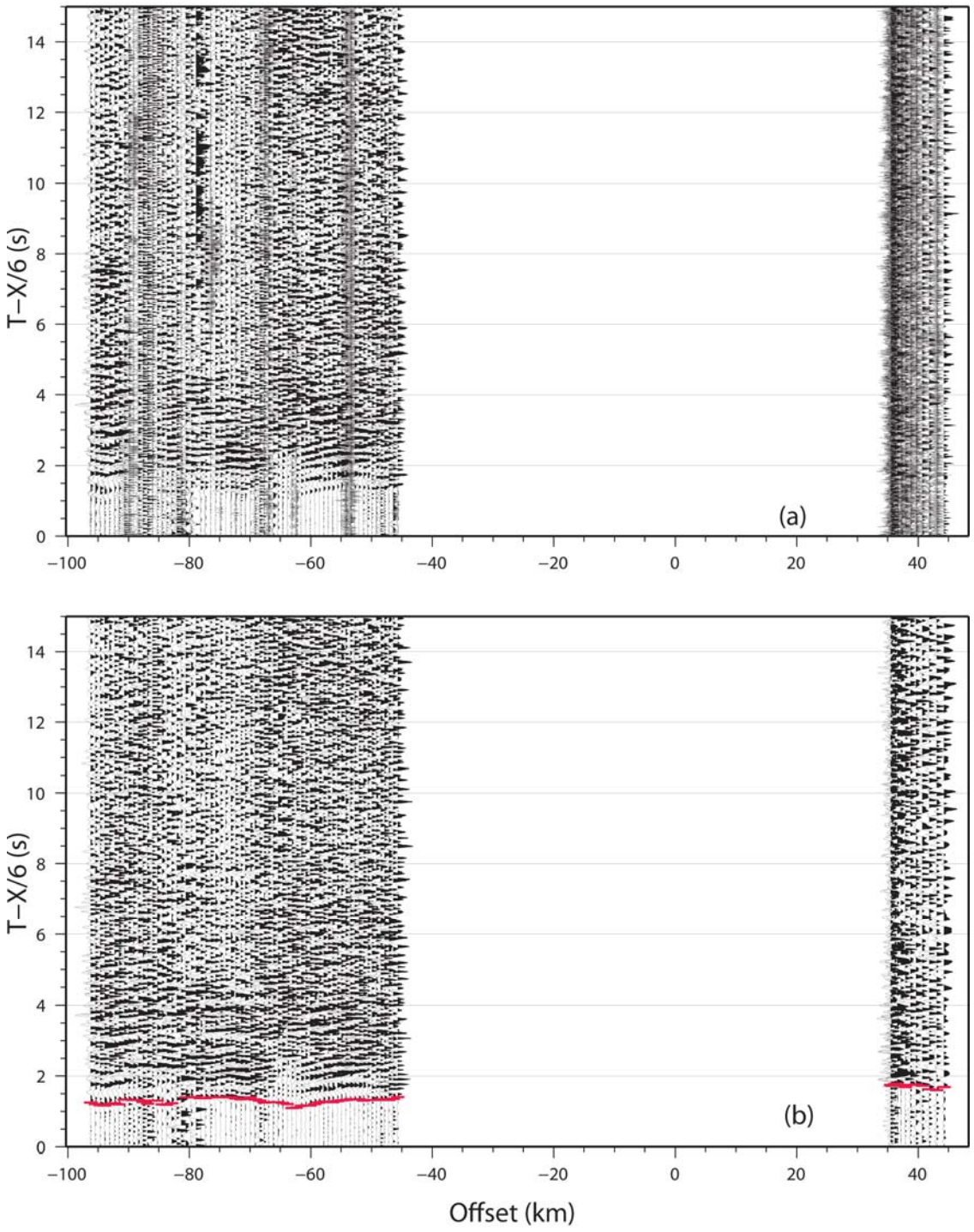

Figure 2.7: Example shot gather for shot point 14 on line 1. Figure (a) is the raw shot gather and Figure (b) is the processed and filtered shot gather for the same line with first arrival picks shown in red.

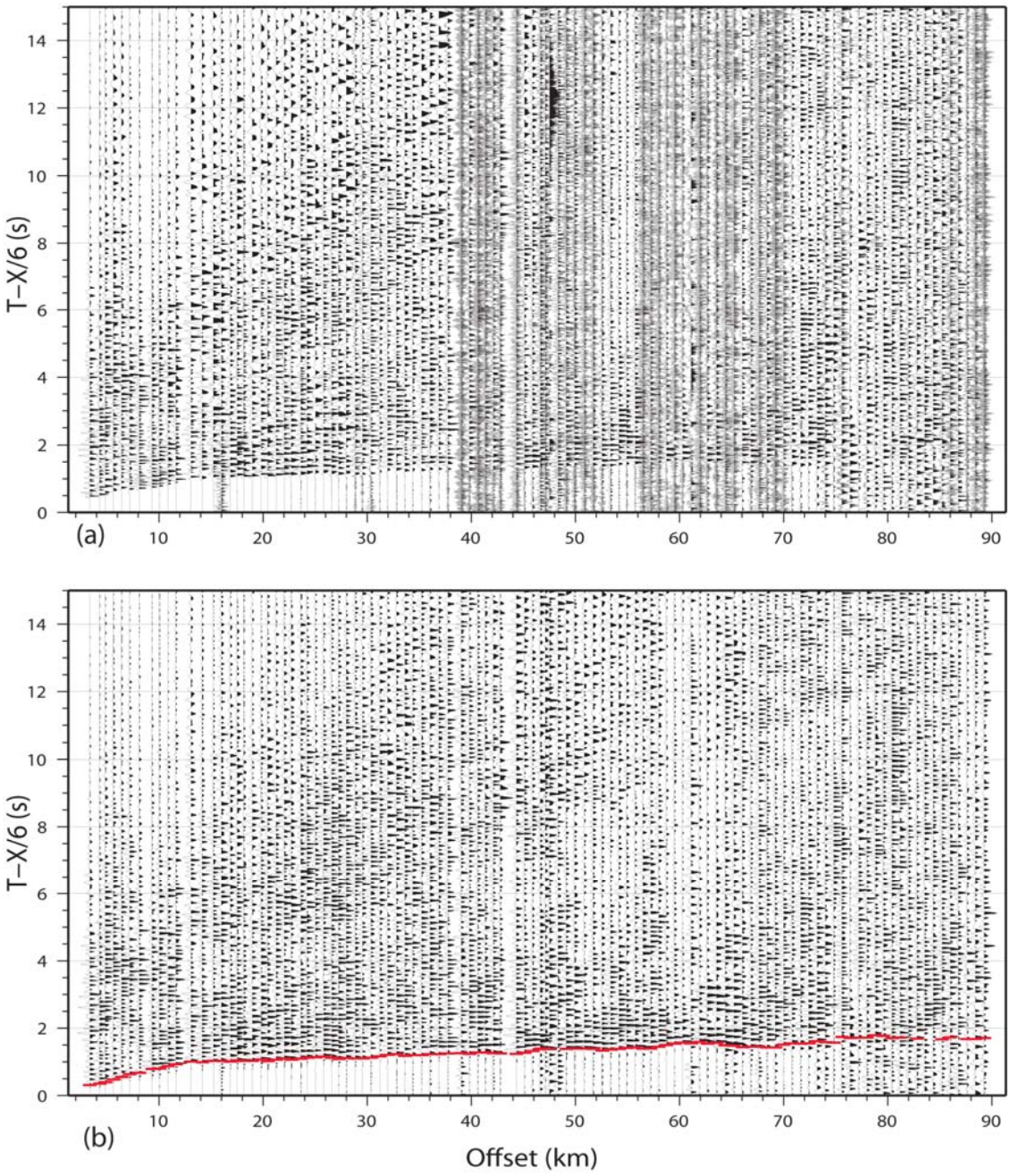

Figure 2.8: Example shot gather for shot point 15 on line 3. Figure (a) is a raw shot gather and Figure (b) is the processed and filtered shot gather on the same line with first arrival picks shown in red.

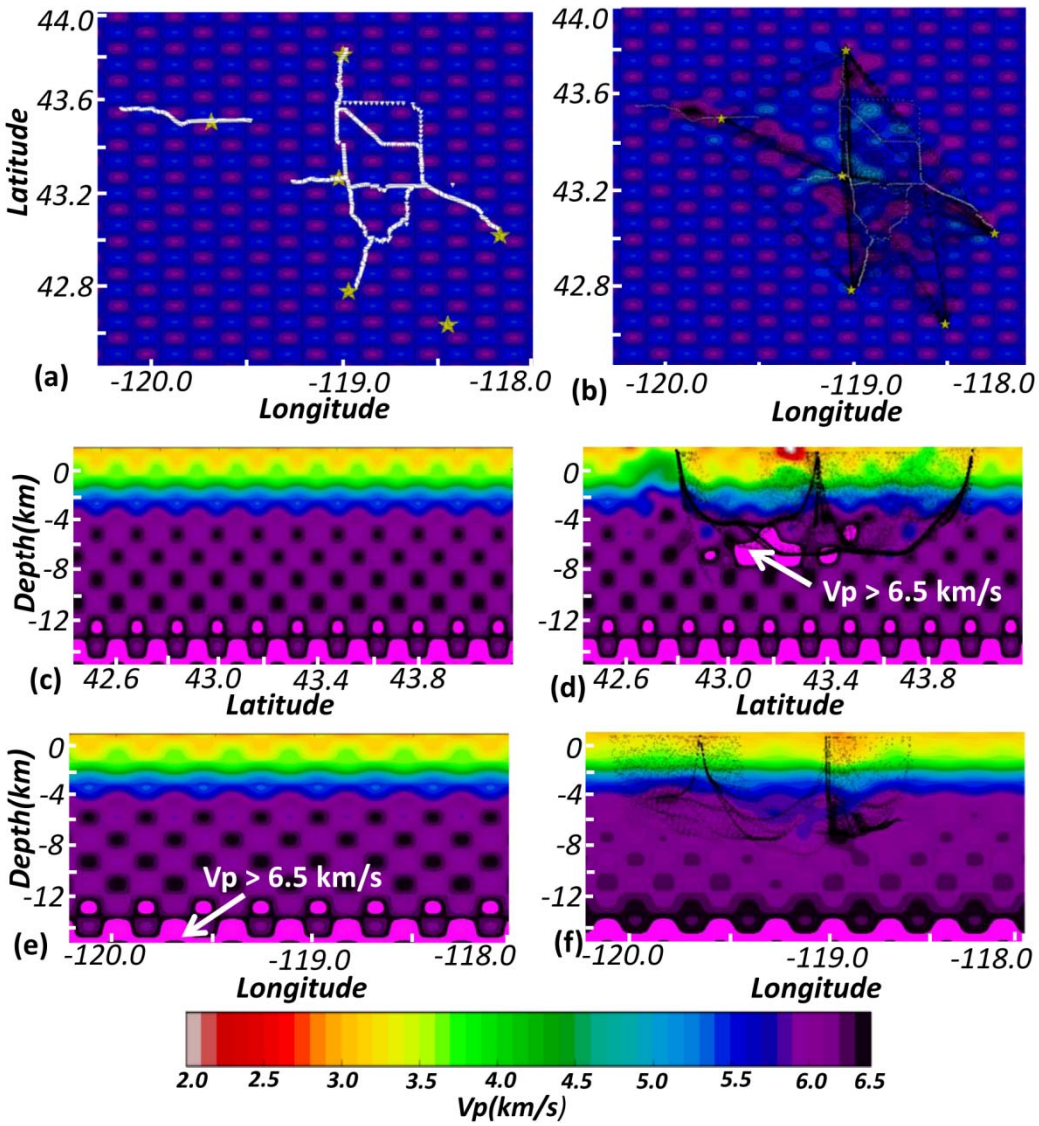

Figure 2.9: Model resolution (checkerboard) test in FMTOMO program before and after inversion. Figures (a), (c), and (e) are pre-inversion slices at 3 km depth, 119^0W longitude, and 43.6^0N latitude respectively. Yellow stars and white inverted triangles in Figure (a) are seismic sources and receivers respectively. Figures (b), (d), and (f) are final velocity models after inversion at the respective positions. Figure (b) shows every 100^{th} ray point in the model space where as figures (d) and (f) shows every 100^{th} ray points that lie within the range of $\pm 0.1^0$ along the chosen slices.

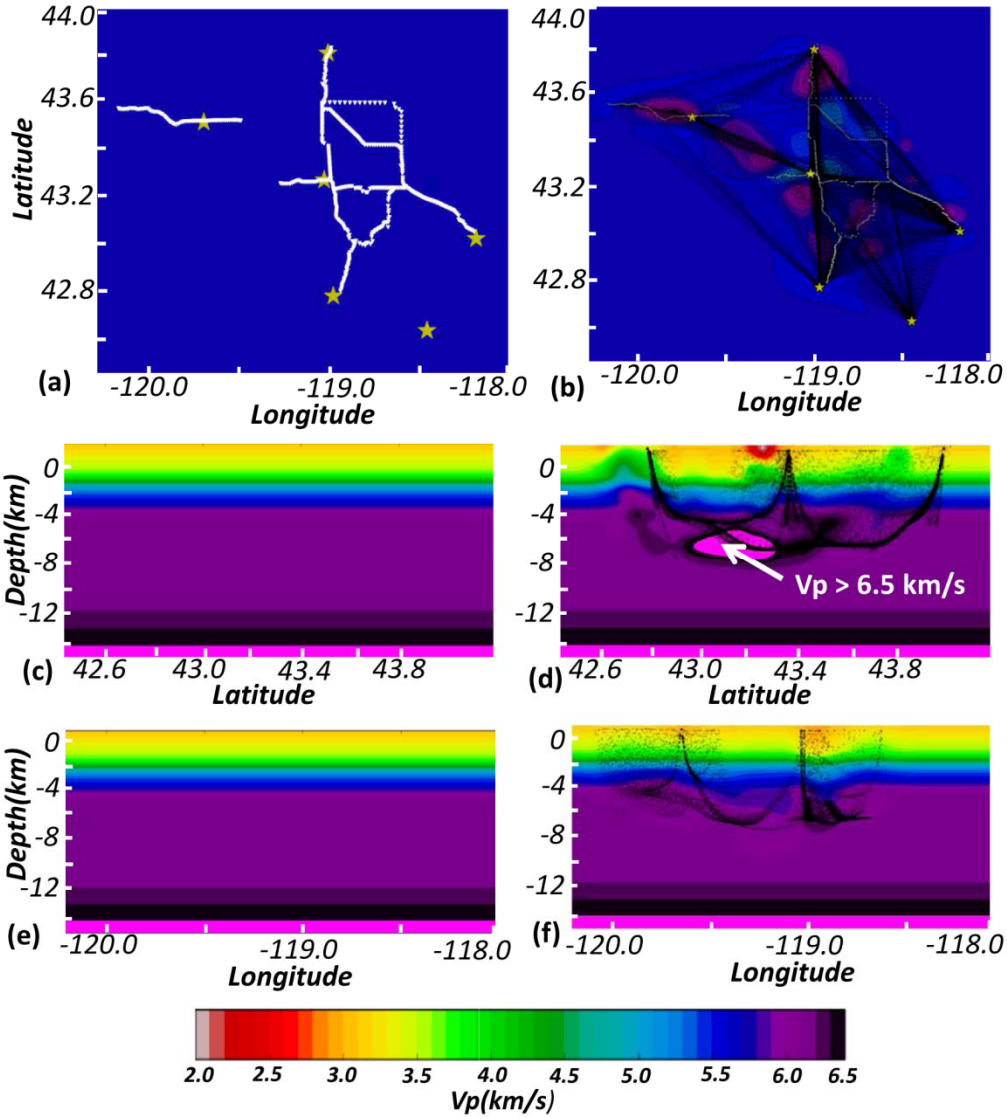

Figure 2.10: Comparison of the pre- and post-inversion velocity models in FMTOMO program. Figures (a), (c), and (e) are pre-inversion slices at 3 km depth, 119^0W longitude, and 43.6^0N latitude respectively. Yellow stars and white inverted triangles in Figure (a) are seismic sources and receivers respectively. Figures (b), (d), and (f) are post inversion slices at the respective positions. Figure (b) shows every 100^{th} ray point in the model space where as Figures (d) and (f) shows every 100^{th} ray points that lie within the range of $\pm 0.1^0$ along the chosen slices.

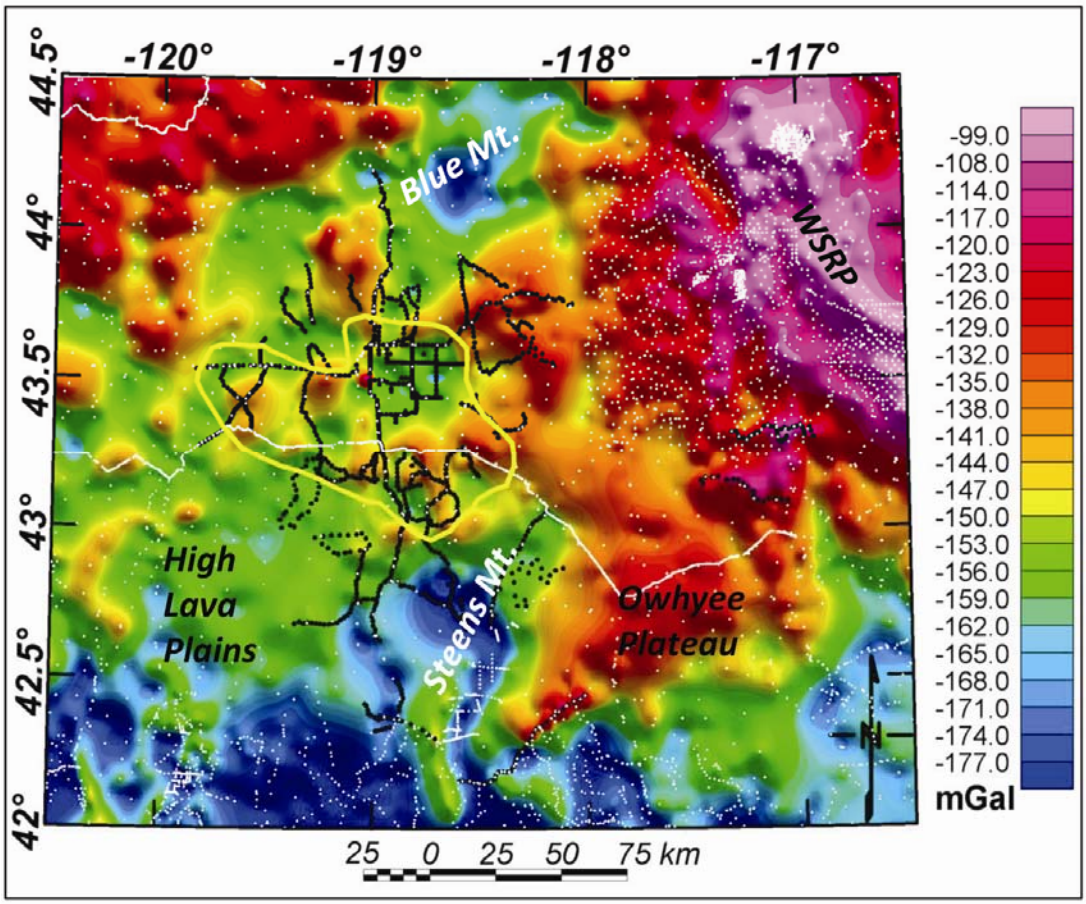

Figure 2.11: Complete Bouguer anomaly (CBA) map of the area. The yellow polygon shows physiographic boundary of the Harney Basin. White dots are the gravity stations from the PACES database whereas black dots are the gravity stations from our 2012 gravity survey. The Western Snake River Plain (WSRP) and the Owyhee Plateau are associated with high gravity anomalies. Steens Mountain and the Blue Mountains have relatively low gravity anomalies whereas the HLP is a broad region of moderate anomaly values.

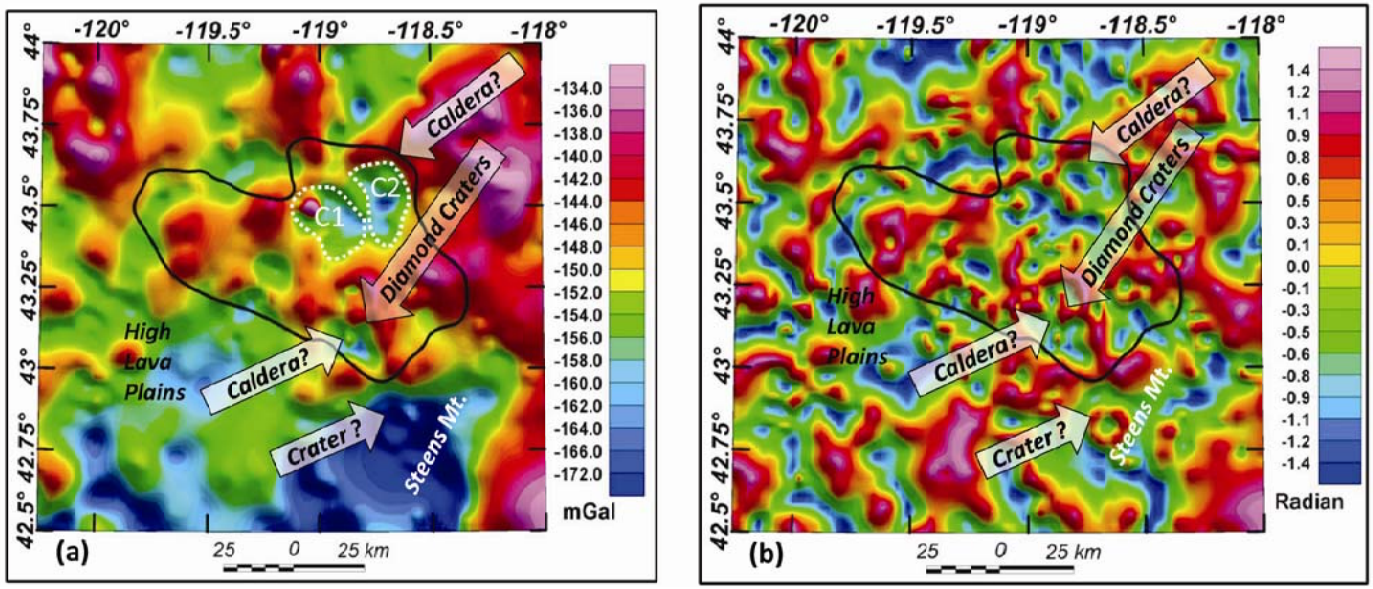

Figure 2.12: Interpretation of major features from gravity anomalies: (a) the CBA map and (b) tilt derivative of the CBA map of the Harney Basin area. The black polygons on both figures show the physiographic boundary of the Harney Basin. The Diamond Craters area contains an irregular circular anomaly that is a possible caldera. The northern portion of the basin contains a distinct gravity low in which C1 and C2 are possible nested calderas. Steens Mountain is associated with the lowest gravity anomaly in the area. A faint circular feature within the Steens Mountain is observed in Figure (a) and is enhanced in Figure (b). This could be a possible crater buried beneath Steens Basalt.

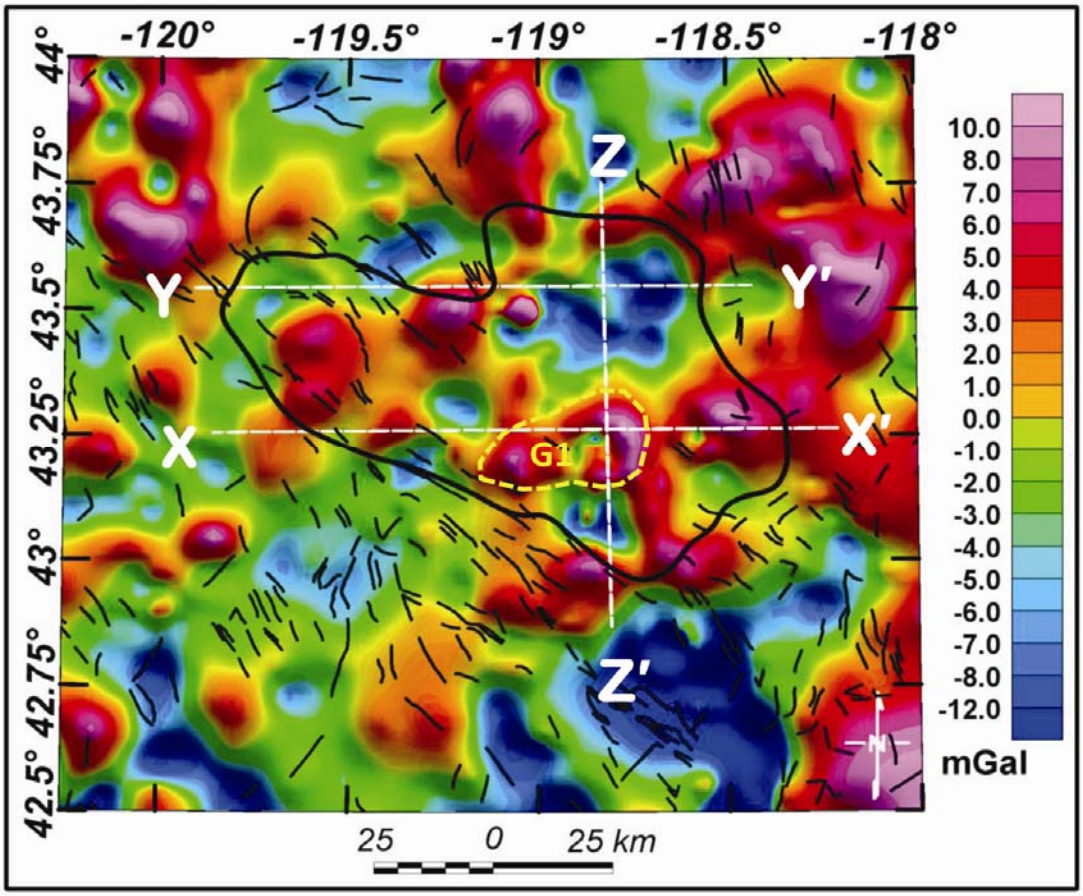

Figure 2.13: Residual Bouguer anomaly map after subtracting the 15 km upward continued surface. The black lines represent mapped faults in the area. The black polygon is the physiographic boundary of the Harney Basin. Dashed white lines XX′, YY′, and ZZ′ are three profiles along which the gravity models are generated and shown in Figures 2.18, 2.19, and 2.20 respectively.

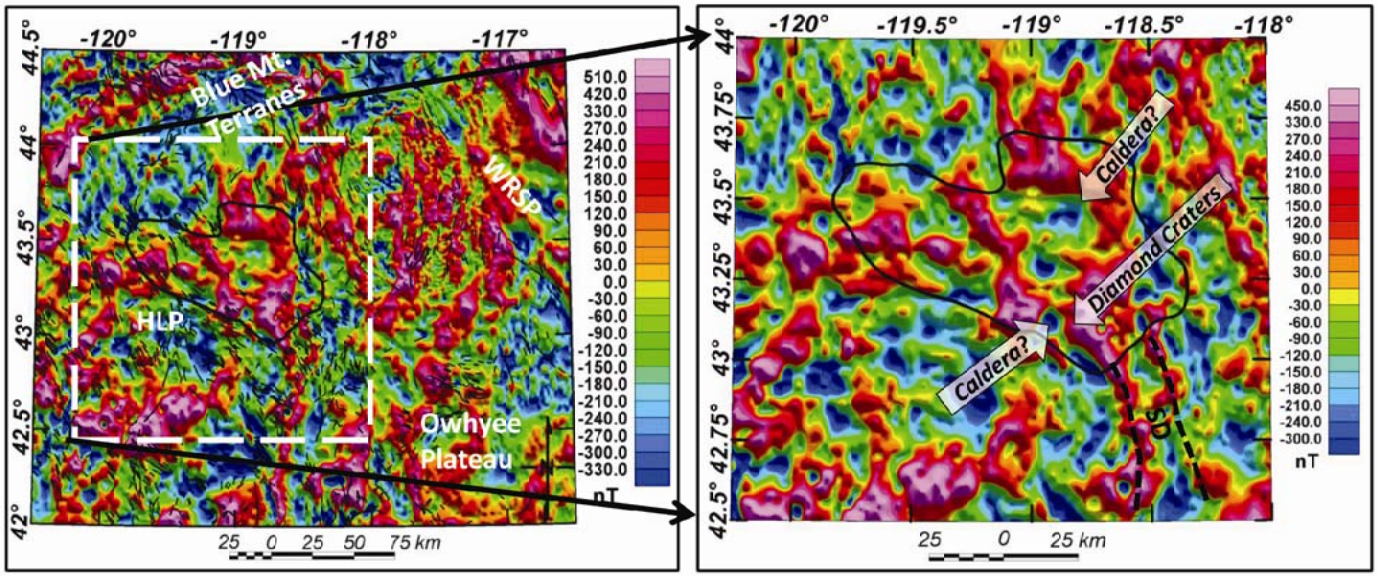

Figure 2.14: Reduced-to-pole total magnetic intensity map of the study area in Figure (a) and a map of Harney Basin area in Figure b. The black polygon is physiographic boundary of the Harney Basin. The black lines in Figure (a) represents mapped faults in the area. The Blue Mountain terranes, Western Snake River Plain (WRSP), Owyhee Plateau, and HLP related magnetic anomalies are identified. In Figure (b), possible calderas within the northern Harney Basin the Diamond Craters area are shown. The Steens Dikes (SD) are indicated by a pair of dashed black lines.

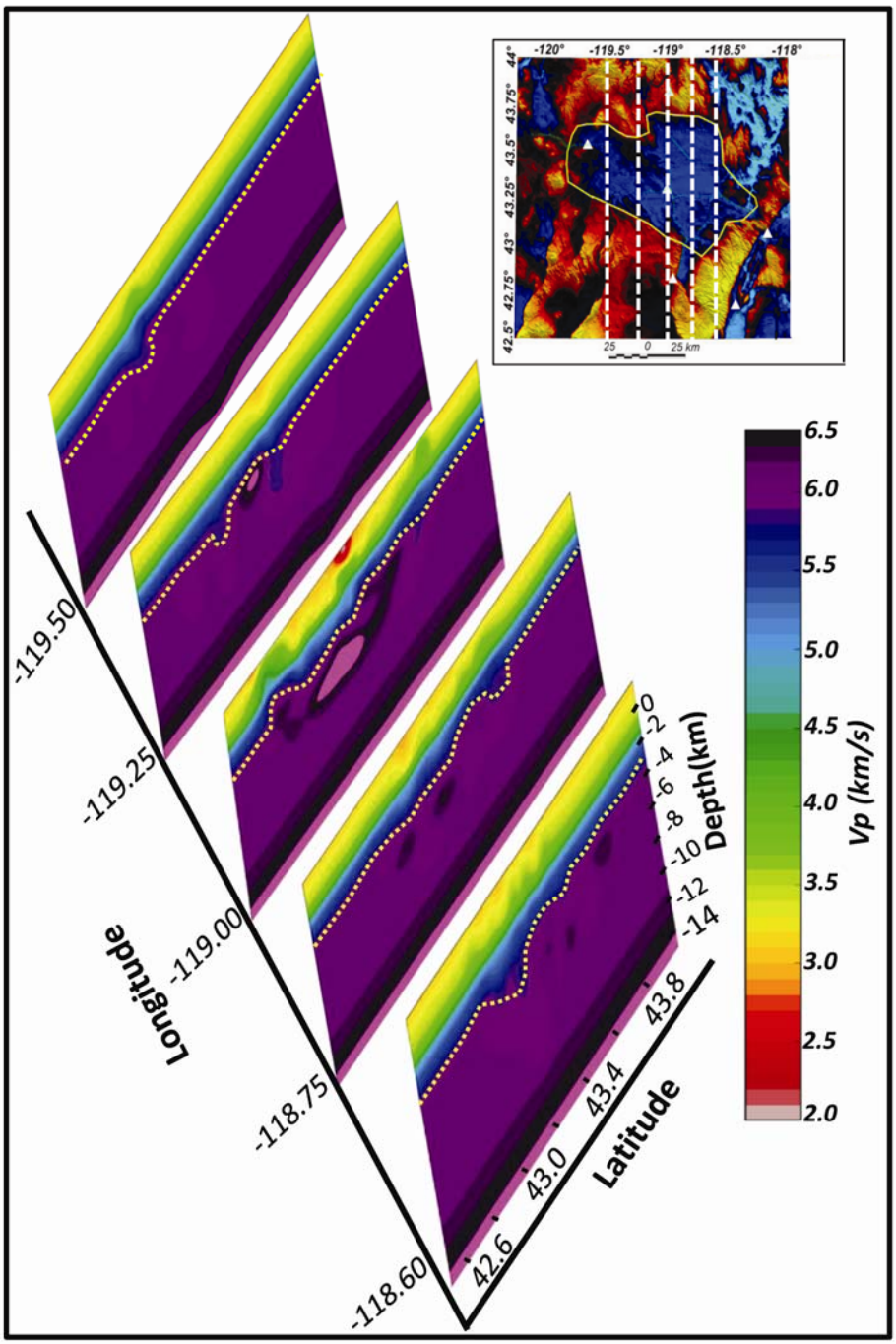

Figure 2.15: Vertical slices through the inverted velocity model of the Harney Basin area shown along longitudinal slices arranged from east to west. The areas with bright pink color in the figure have velocities greater than 6.5 km/s. Dashed white lines in the inset figure are location of these slices on the DEM map.

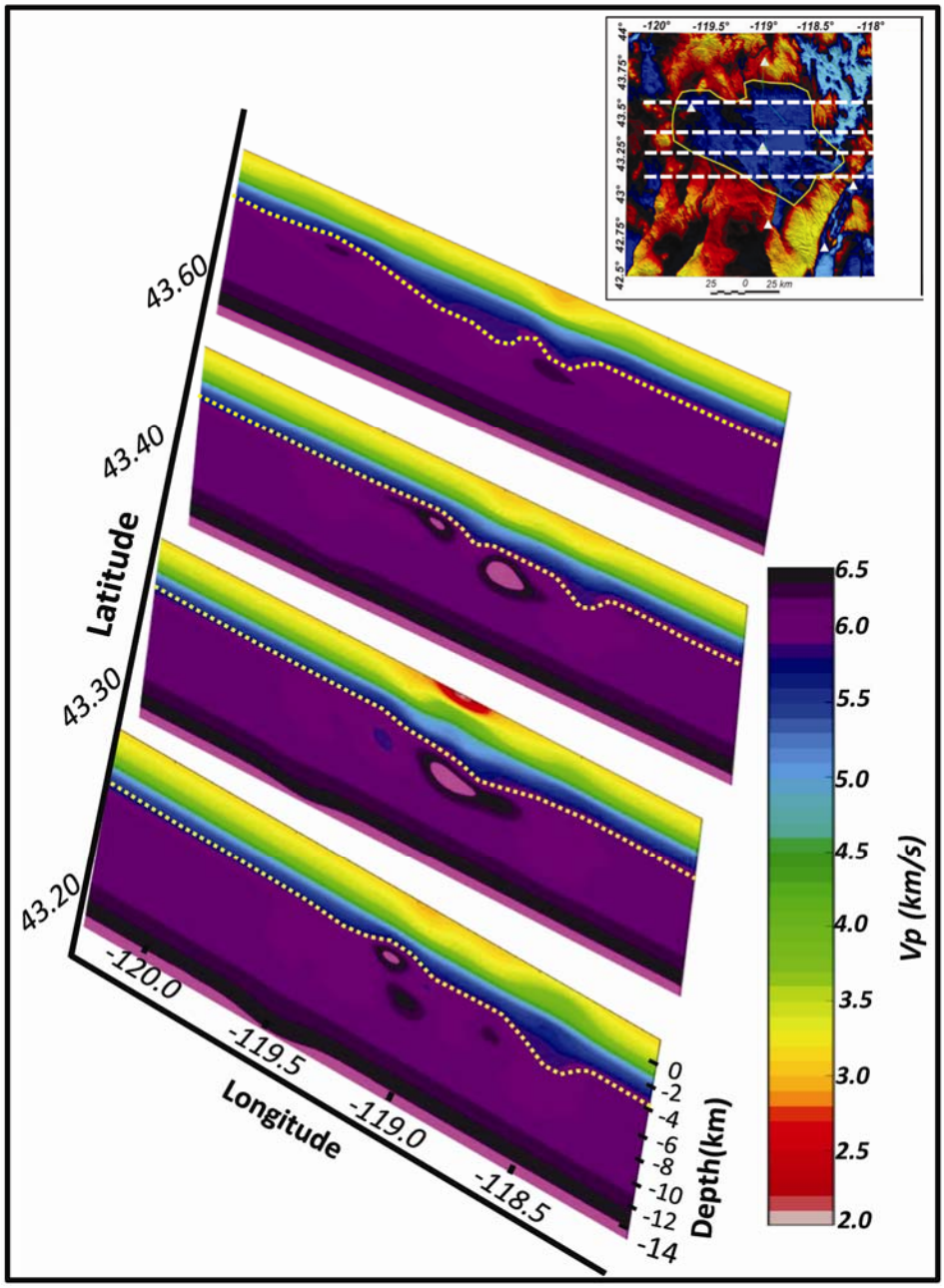

Figure 2.16: Vertical slices through the inverted velocity model of the Harney Basin area shown along latitudinal slices arranged from south to north. The areas with bright pink color in the figure have velocities greater than 6.5 km/s. Dotted white lines in the inset figure shows location of these slices on the DEM map.

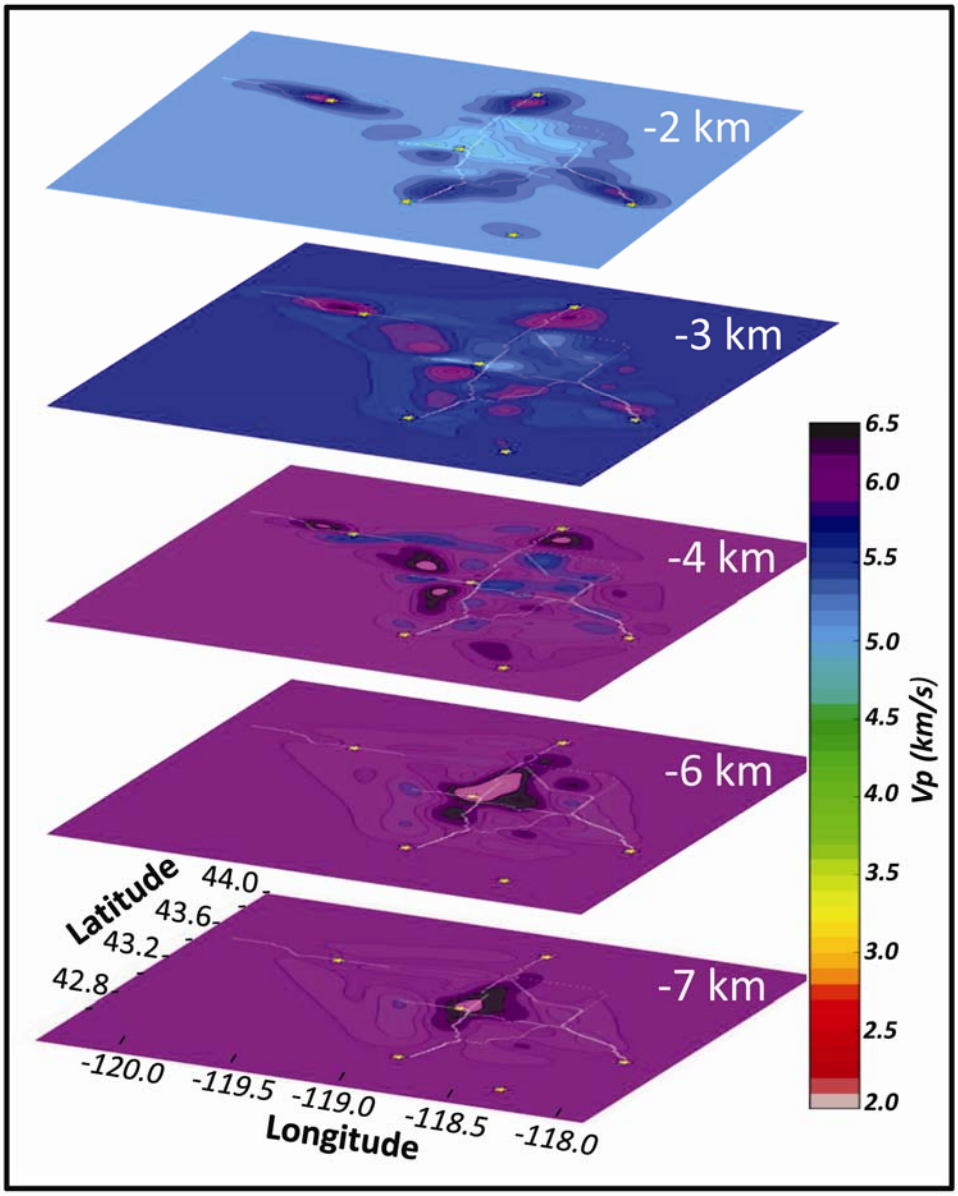

Figure 2.17: Inverted velocity model of the Harney Basin area shown along depth slices. The areas with bright pink color in the figure have velocities greater than 6.5 km/s. The depth annotations are below mean sea level (msl).

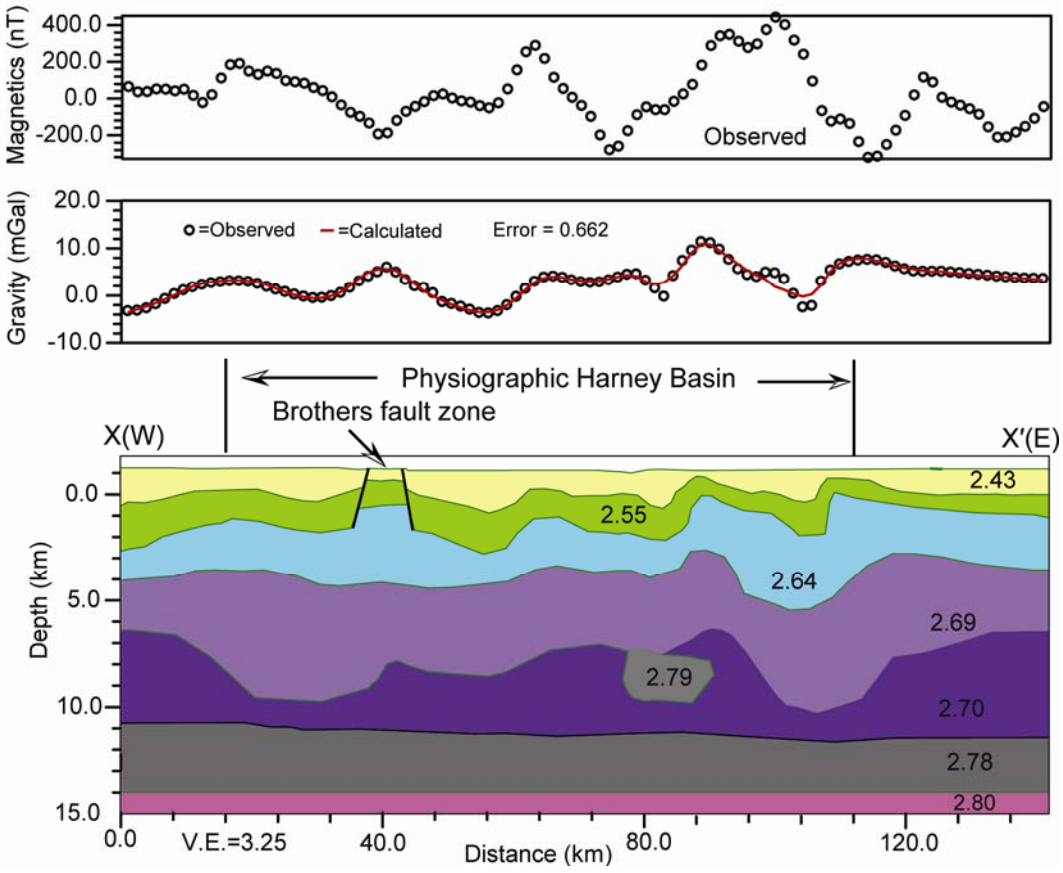

Figure 2.18: Gravity model of the upper crust across Harney Basin area along 43.25^{0}N latitude (X-X′, Fig. 2.13) based on gridded 15 km upward continued residual Bouguer anomaly values. Density values are in g/cm^3. V.E. stands for vertical exaggeration.

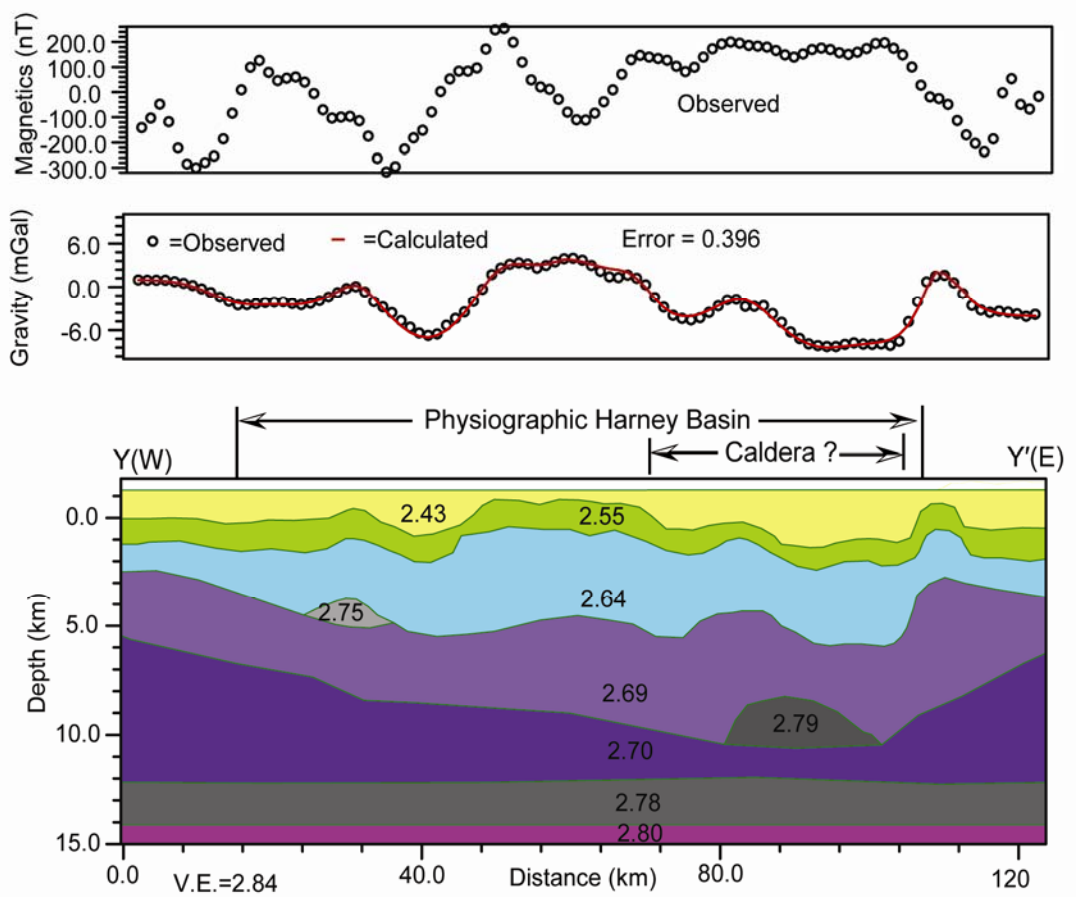

Figure 2.19: Gravity model of the upper crust across Harney Basin area along 43.60^0N latitude (Y-Y′, Fig. 2.13) based on gridded 15 km upward continued residual Bouguer anomaly values. Density values are in g/cm^3. V.E. stands for vertical exaggeration.

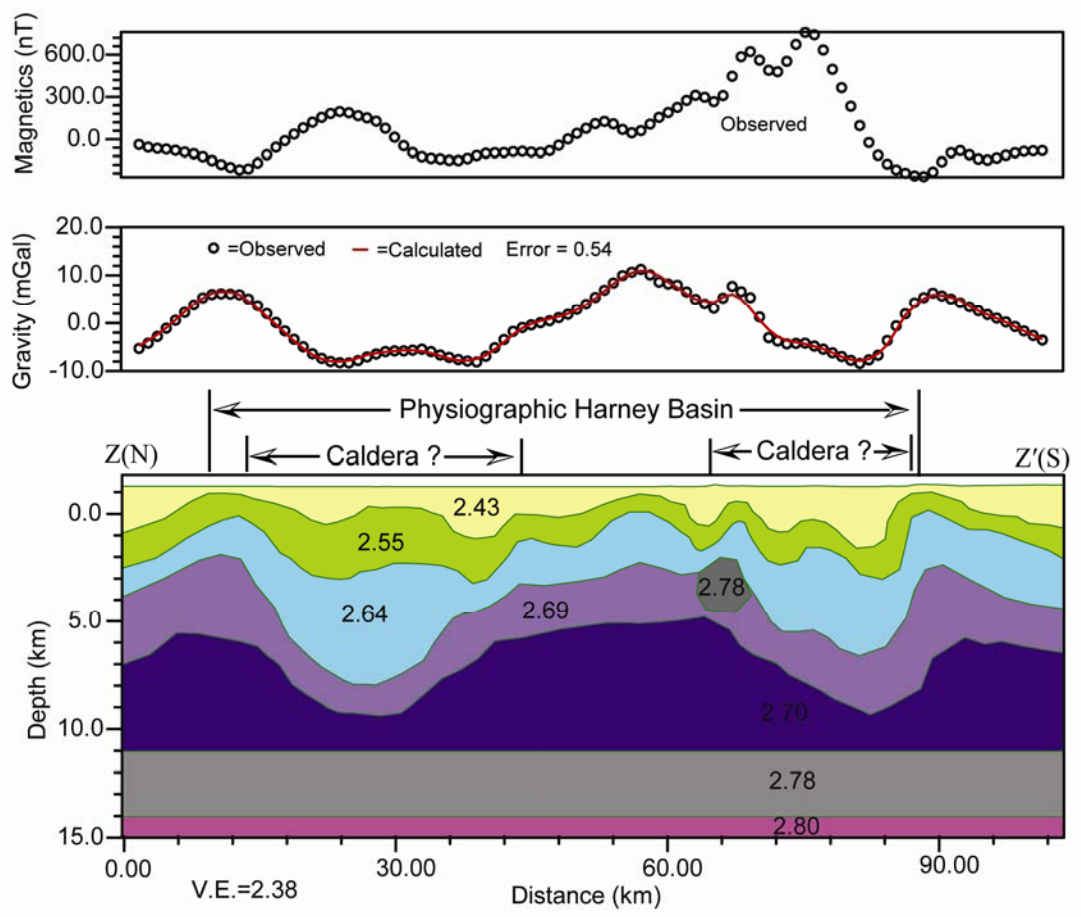

Figure 2.20: Gravity model of the upper crust across Harney Basin area along 118.80^0W longitude (Z-Z′, Fig. 2.13) based on gridded 15 km upward continued residual Bouguer anomaly values. Density values are in g/cm^3. V.E. stands for vertical exaggeration.

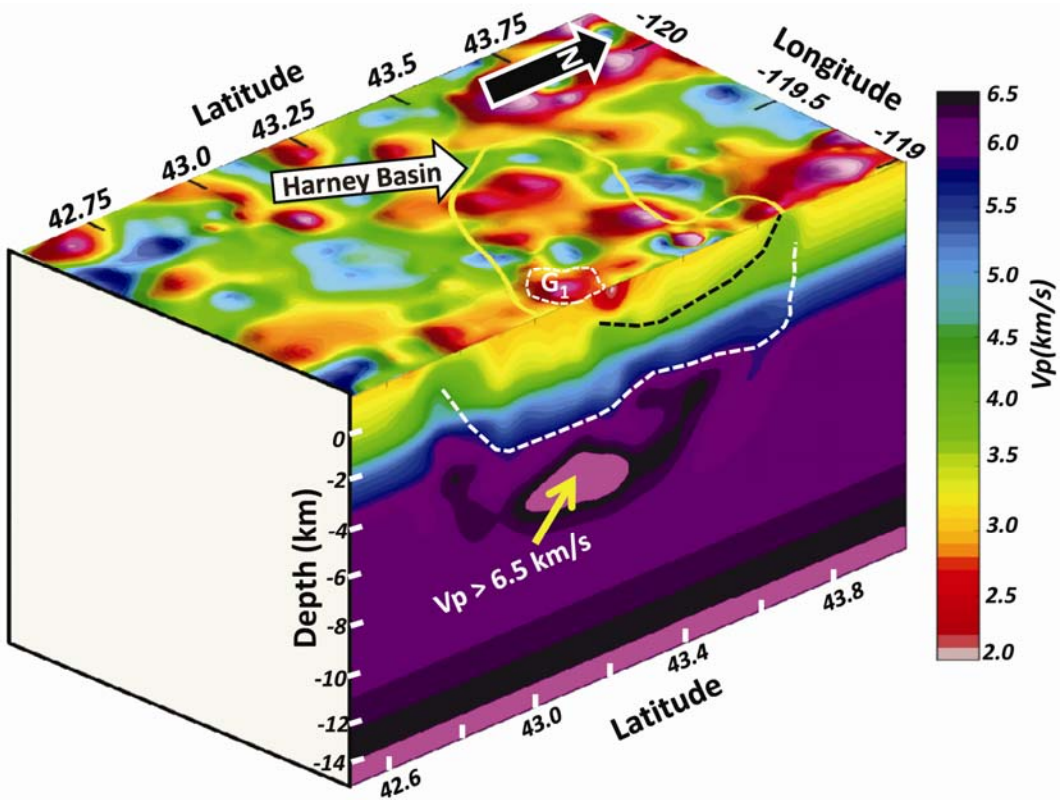

Figure 2.21: A block diagram illustrating the relationship between the major upper crustal structures in the Harney Basin area observed in the 15 km residual Bouguer anomaly map (on the top) with the inverted velocity model along 119^0W longitude.

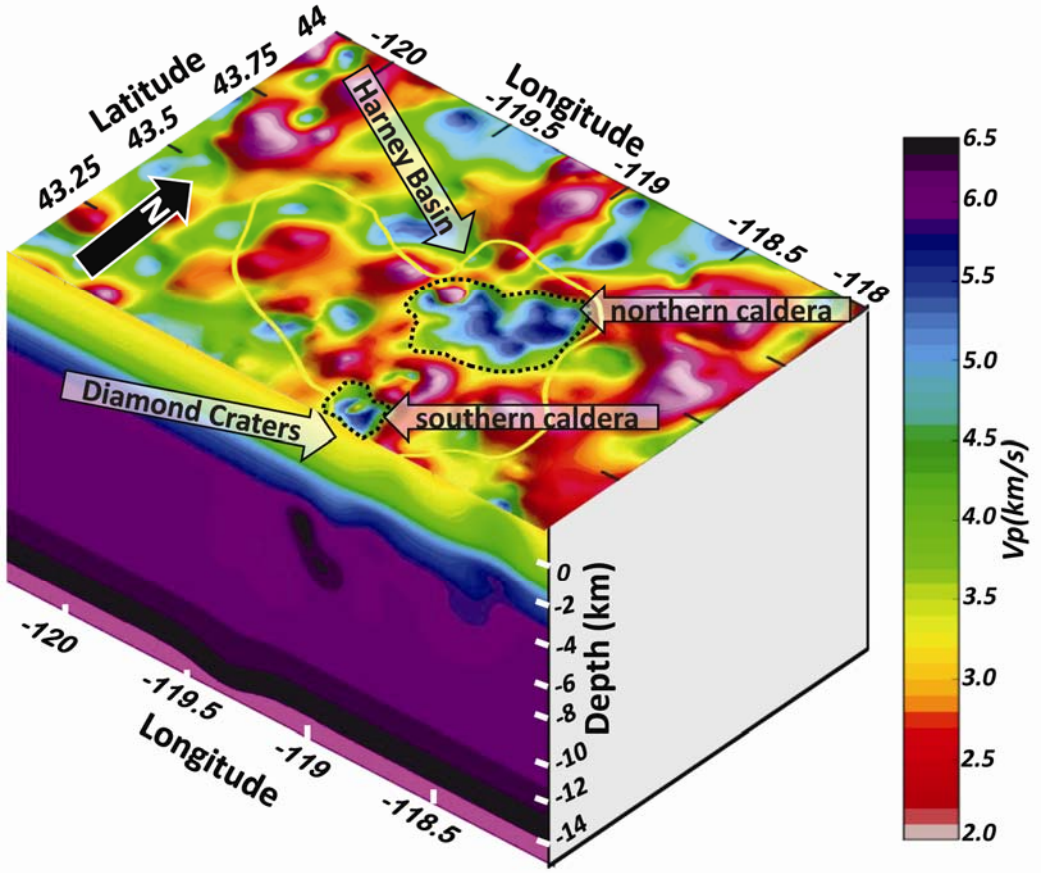

Figure 2.22: A block diagram illustrating the relationship between the major upper crustal structures in the Harney Basin area observed in the 15 km residual Bouguer anomaly map (on the top) with the inverted velocity model along 43.10^{0}N latitude.

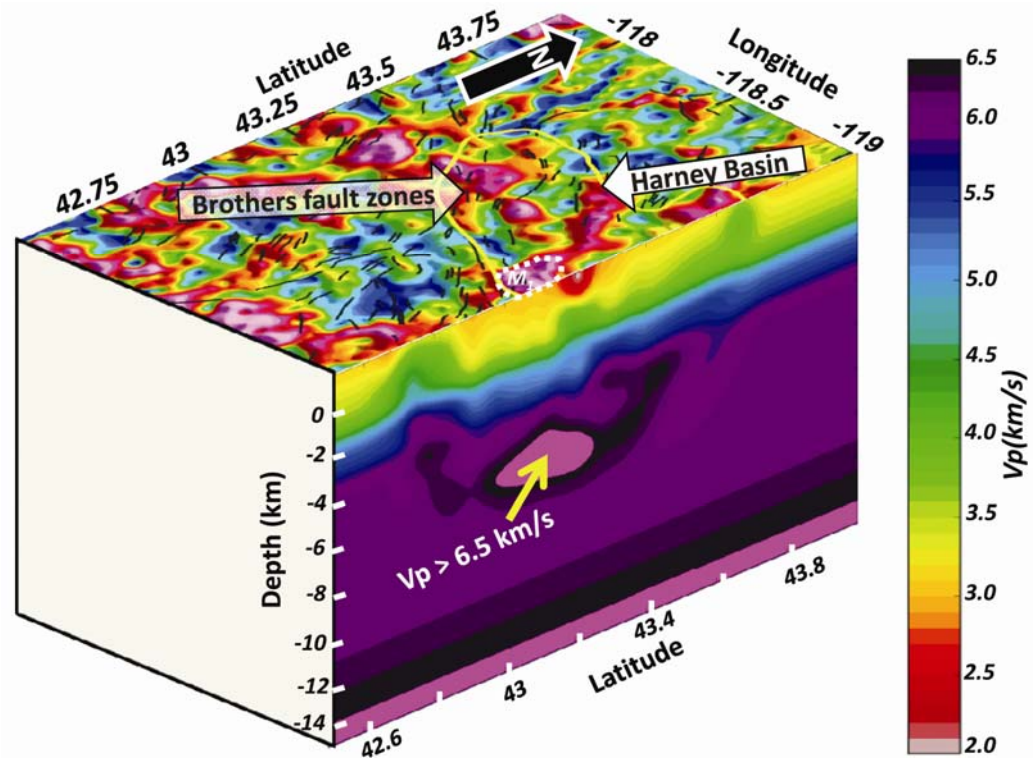

Figure 2.23: A block diagram illustrating relationship between the major upper crustal structures in the Harney Basin area observed in the reduced-to-pole total magnetic intensity map (on the top) with the inverted velocity model along 119^0W longitude.

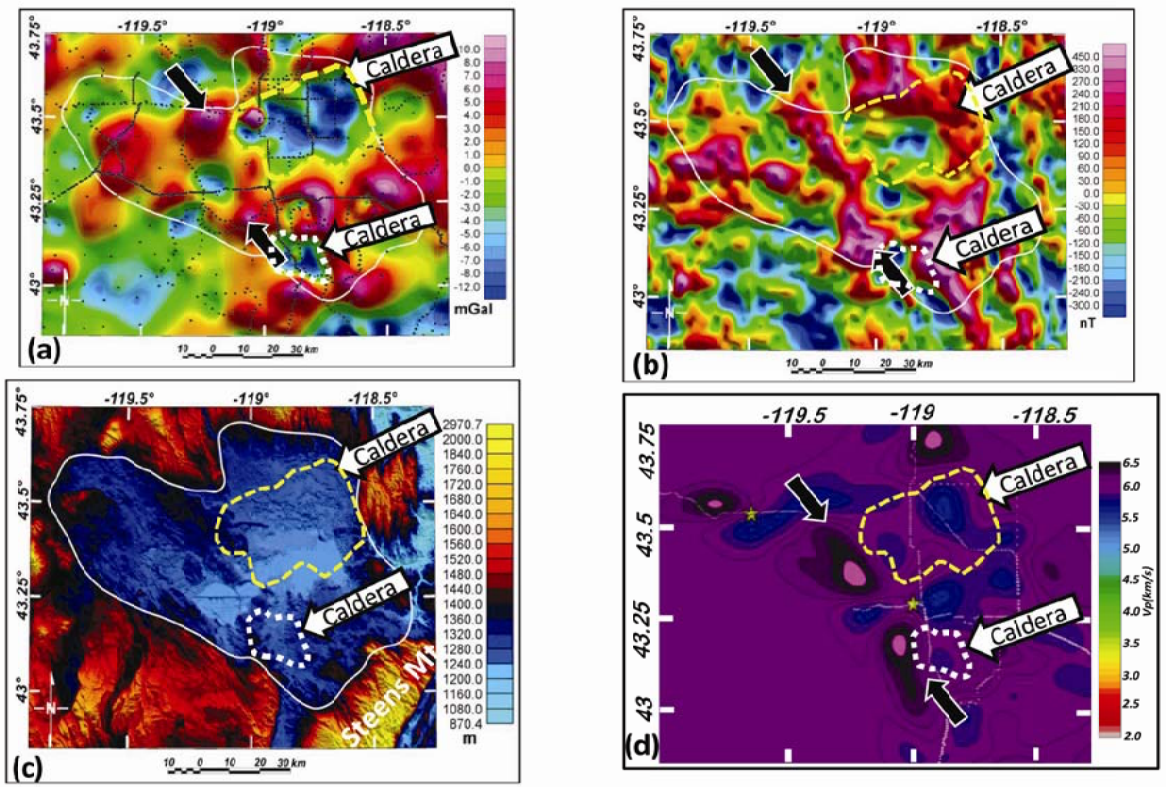

Figure 2.24: Harney Basin features in multiple datasets. Figures (a), (b), (c), and (d) shows residual CBA map after 15 km upward continuation, reduced-to-pole TMI map, the 10 m resolution digital elevation model, and seismic velocity model at 4 km depth from mean sea level respectively. All of these maps suggest the presence of caldera features (dashed white and yellow lines) in the basin. A NW-SE trending high gravity, magnetic, and seismic velocity feature (shown by black arrows) in Figures (a), (b), and (d) indicates mafic dikes are present in the subsurface.

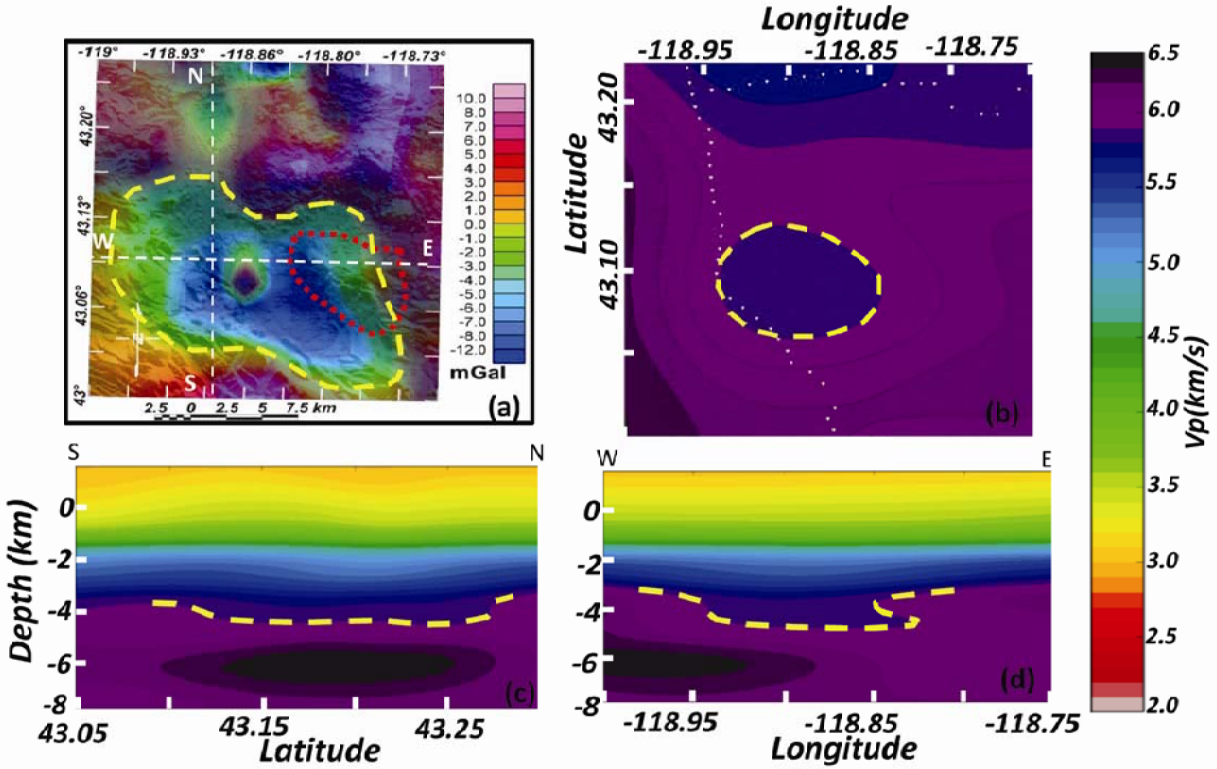

Figure 2.25: Integrated geophysical interpretation of the Diamond Craters area. Figure (a) is residual Bouguer anomaly map draped on the 10 m DEM in the area. Figure (b) is horizontal velocity slice at 4 km depth from msl. Figure (c) is a longitudinal slice along 118.9^0W. Figure (d) is a latitudinal slice at 43.1^0N. The dotted red line in (a) is the location of Diamond Craters based on the DEM map. Yellow dotted lines indicate the southern caldera feature delineated based on the residual gravity and DEM maps and supported by seismic velocity slices shown in Figures (b), (c), and (d).

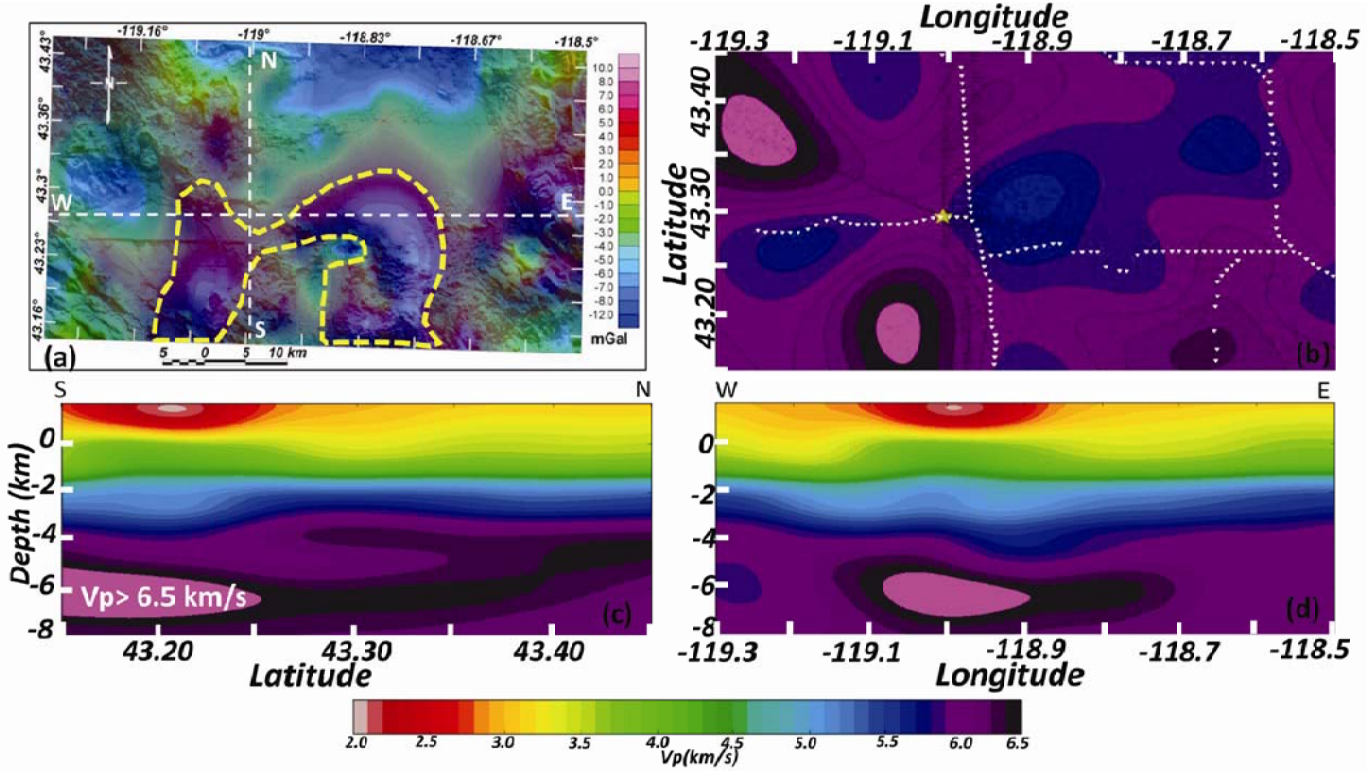

Figure 2.26: Integrated geophysical interpretation of the central lake area. Figure (a) is residual Bouguer anomaly map draped on the 10 m DEM in the area. Figure (b) is horizontal velocity slice at 4 km depth from msl. Figure (c) is a longitudinal slice along 119^0W. Figure (d) is a latitudinal slice at 43.25^0N. The dotted yellow line in figure (a) is the gravity high in the Harney Lake, Mud Lake and Malheur Lake area. High velocity (> 6.5 km/s) upper crust lies beneath these lakes at about 5-6 km depth from msl.

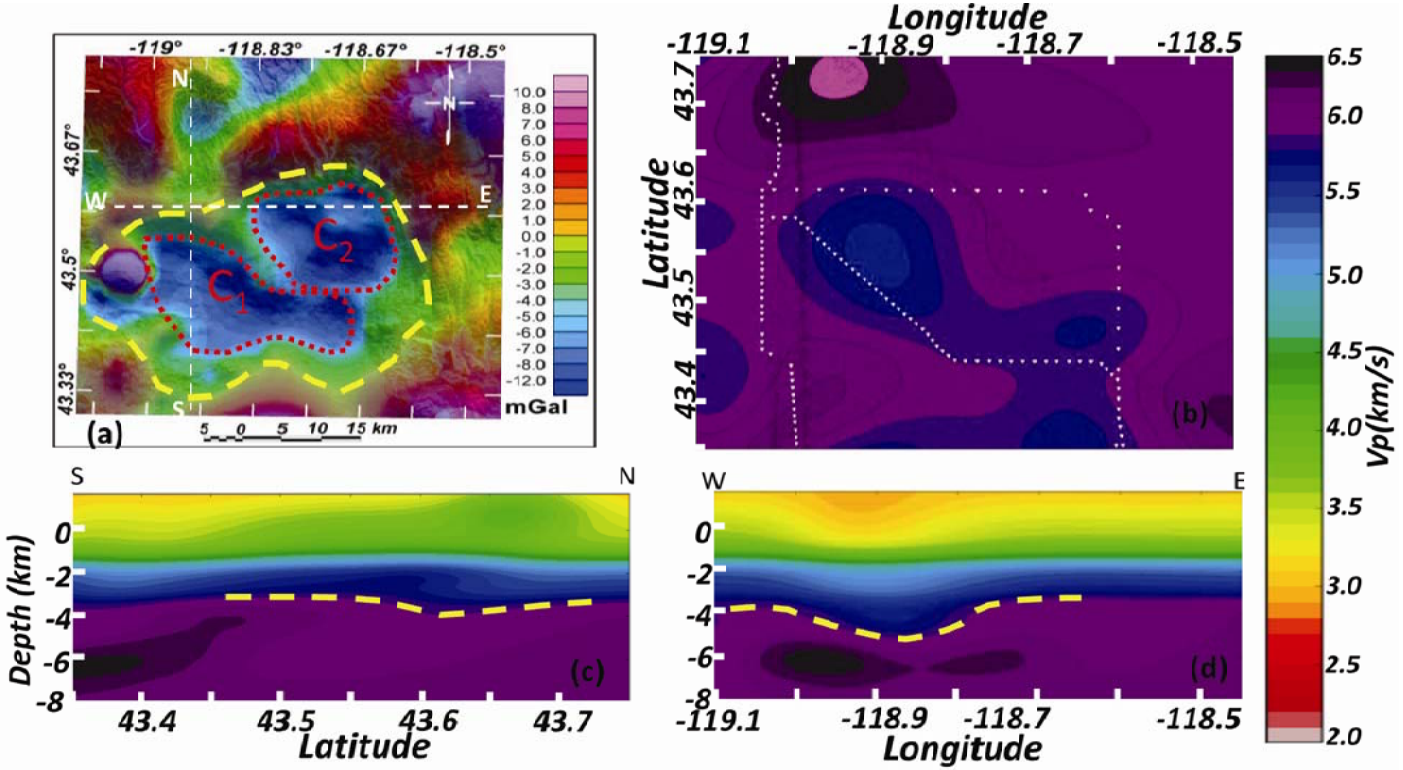

Figure 2.27: Integrated geophysical interpretation of the northern caldera. Figure (a) is residual Bouguer anomaly map draped on the 10 m DEM in the area. Figure (a) is residual Bouguer anomaly map draped on the 10 m DEM in the area. Figure (b) is horizontal velocity slice at 4 km depth from msl. Figure (c) is a longitudinal slice along 118.9^0W. Figure (d) is a latitudinal slice at 43.55^0N latitude. The dotted yellow line in figure (a) is the northern caldera features delineated based on the residual gravity and DEM map and supported by seismic velocity slices shown in Figures (b), (c), and (d).

References

Anderson, R.E., 1989, Tectonic evolution of the Intermontane System; Basin and Range, Colorado Plateau, and High Lava Plains, Geophysical framework of the continental United States: Geological Society of America, Memoir 172, p. 163-176.

Armstrong, R.L., Leeman, W.P., and Malde, H.E., 1975, K-Ar dating, Quaternary and Neogene rocks of the Snake River Plain, Idaho, Am. J. Sci., v. 275, 225– 251.

Armstrong, R.L., Haubeneck, T.W., and Hales, P.O., 1977, Rb-Sr and K-Ar geochronometry of Mesozoic granitic rocks and their Sr isotopic composition, Oregon, Washington, and Idaho, Geological Society of America Bulletin, v.88, p. 397-411.

Baldwin, E.M., 1976, Geology of Oregon (Revised): Kendall/Hunt Publishing Company, Dubuque, Iowa, 147 p.

Benford, B., Crowley, J., Schmitz, M., Northrup, C.J., and Tikoff, B., 2010, Mesozoic magmatism and deformation in the northern Owyhee Mountains, Idaho: Implications for a long-zone variations for the western Idaho shear zone: Lithosphere, v. 2, p. 93-118.

Brikke, N.E.A., 2010, 3D Seismic Traveltime Tomography of the Central South Island, New Zealand, MS thesis, Victoria University of Wellington, Wellington, New Zealand, 131 p.

Brocher, T.M., 2005, Empirical relations between elastic wave speeds and density in the Earth's crust: Bulletin of the Seismological Society of America, v. 95, p. 2081-2092.

Brueseke, M.E., Heizler, M.T., Hart, W.K., and Mertzman, S.A., 2007, Distribution and geochronology of Oregon Plateau (U.S.A.) flood basalt volcanism: the Steens

Basalt revisited: J. Volcan. Geotherm. Res., v. 161, p. 187-214, doi:10.1016/j.jvolgeores.2006.12.004.

Camp, V.E., Ross, M.E., and Hanson, W.E., 2003, Genesis of flood basalts and Basin and Range volcanic rocks from Steens Mountain to the Malheur River Gorge, Oregon: Geological Society of America Bulletin, v. 115, p. 105-128.

Camp, V.E., and Ross, M.E., 2004, Mantle dynamics and genesis of mafic magmatism in the intermontane Pacific Northwest: J. Geophys. Res., v. 109, B08204, doi: 10.1029/2003JB002838.

Carlson, R.W., and Hart, W.K., 1987, Crustal genesis on the Oregon Plateau, J. Geophys. Res.: v. 92, p. 6191-6206.

Catchings, R.D. and Mooney, W.D., 1988, Crustal structure of east central Oregon: relation between Newberry Volcano and regional crustal structure, J. Geophys. Res.: v. 93, p. 10,081-10,094.

Christiansen, R.L., and Yeats, R.S., 1992, Post-Laramide geology of the U.S. Cordilleran region, in Burchfiel, B.C., Lipman, P.W., and Zoback, M.L., eds., The Cordilleran Orogen: Conterminous U.S.: Geological Society of America, The Geology of North America, v. G-3, p. 261-406.

Christiansen, R.L., and McKee, E.H., 1978, Late Cenozoic volcanic and tectonic evolution of the Great Basin and Columbia Intermontane regions, in Smith, R.B., and Eaton, G.P., eds., Cenozoic tectonics and regional geophysics of the western Cordillera: Geological Society of America Memoir 152, p. 283 – 311.

Cole, J.W., Milner, D.M., and Spinks, K.D., 2005, Calderas and caldera structures: a review: Earth-Science Reviews, v. 69, p. 1-26.

Cox, C., 2011, A controlled source seismic and gravity study of the High Lava Plains (HLP): MS Thesis, University of Oklahoma, 110 p.

De Kool, M., Rawlinson, N., and Sambridge, M., 2006, A practical grid-based method for tracking multiple refraction and reflection phases in three-dimensional heterogeneous media: Geophysical Journal International, v. 167, p. 253-270.

Draper, D.S., 1991, Late Cenozoic bimodal magmatism in the northern Basin and Range Province of southeastern Oregon: Journal of Volcanology and Geothermal Research, v. 47, p. 299 – 328.

Druken, K.A., Long, M.D., and Kincaid, C., 2011, Patterns in seismic anisotropy driven by rollback subduction beneath the High Lava Plains: Geophysical Research Letters, v. 38, L13310, doi:10.1029/2011GL047541 .

Eagar, K.C., Fouch, M. J., and James, D.E., 2010, Receiver function imaging of upper mantle complexity beneath the Pacific Northwest, United States: Earth Planet. Sci. Lett., v. 297, p. 141–153, doi:10.1016/j.epsl.2010.06.015.

Eagar, K.C., Fouch, M.J., James, D.E., & Carlson, R.W, 2011, Crustal structure beneath the High Lava Plains of eastern Oregon and surrounding regions from receiver function analysis: J. Geophys. Res., v. 116, p. 1978–2012.

Eaton, G.P., 1984, The Miocene Great Basin of western North America as an extending back-arc region: Tectonophysics, v. 102, p. 275-295.

Ford, M.T., Grunder, A.L., & Duncan, R.A., 2013, Bimodal volcanism of the high lava plains and Northwestern Basin and Range of Oregon: The distribution and tectonic implications of age-progressive rhyolites. Geochemistry, Geophysics, Geosystems, accepted article., DOI 10.1002/ggge.20175.

Greene, R.C., 1973, Petrology of the welded tuff of Devine Canyon, southeastern Oregon., Geological Survey professional paper 979, US Government Printing Office.,Washington, 36 p.

Hart, W.K., 1985, Chemical and isotopic evidence for mixing between depleted and enriched mantle, northwestern U.S.A.: Geochim. Cosmochim. Acta., v. 49, p. 131-144.

Hart, W.K., Aronson, J. L., and Mertzman, S.A., 1984, Areal distribution and age of low-K, high-alumina olivine tholeiite magmatism in the northwestern Great Basin: Geological Society of America Bulletin, v. 95, p. 186-195.

Hooper, P.R., 1997, The Columbia River flood basalt province: Current status, in Large Igneous Provinces, Continental, Oceanic, and Planetary Flood Volcanism, Geophys. Monogr. Ser., edited by J. J. Mahoney and M. F. Coffin, v. 100, p 1–27.

Hooper, P.R., Binger, G.B., and Lees, K.R., 2002, Constraints on the relative an absolute ages of the Steens and Columbia River basalts and their relationship to extension-related calc-alkaline volcanism in eastern Oregon: Geological Society of America Bulletin, v. 114, p. 43–50.

Holom, D.I., and Oldow, J.S., 2007, Gravity reduction spreadsheet to calculate the Bouguer anomaly using standardized methods and constants: Geosphere, v. 3, p. 86-90.

Jordan, B.T., 2002, Basaltic volcanism and tectonics of the High Lava Plains, southeastern Oregon, PhD Dissertation, Oregon State University, 218 p..

Jordan, B.T., Grunder, A.L, Duncan, R.A., Deino, A.L., 2004, Geochronology of age-progressive volcanism of the Oregon High Lava Plains: Implications for the plume interpretation of Yellowstone. J. Geophys. Res., v. 109, B10202.

Kane, M.F., Mabey, D.R., and Brace, R.L., 1976, A gravity and magnetic investigation of the Long Valley caldera, Mono County, California: J. Geophys. Res., v. 81, p.754-762.

Keller, G.R., Hildenbrand, T.G., Kucks, R., Webring, M., Briesacher, A., Rujawitz, K., Hittleman, A.M., Roman, D. J., Winester, D., Aldouri, R., Seeley, J., Rasillo, J., Torres, T., Hinze, W.J., Gates, A., Kreinovich, V., and Salayandia, L., 2006, A community effort to construct a gravity database for the United States and an associated web portal, in A. K. Sinha, Editor, Geoinformatics: Data to Knowledge, Geological Society of America, Boulder, Colorado, p. 21-34.

Lerch, D.W., Klemperer, S.L., Glen, J.M.G., Ponce, D.A., Miller, E.L., and Colgan, J.P., 2007, Crustal structure of the northwestern Basin and Range Province and its transition to unextended volcanic plateaus: Geochem. Geophys. Geosyst., v. 8(2), Q02011, doi:10.1029/2006GC001429.

Lerch, D.W., Miller, E., McWilliams, M., and Colgan, J., 2008, Tectonic and magmatic evolution of the northwestern Basin and Range and its transition to unextended volcanic plateaus: Black Rock Range, Nevada: Geological Society of America Bulletin, v. 120, p. 300–311.

Lipman, P.W., Prostka, H.J., and Christiansen, R.L., 1971, Evolving subduction zones in the western United States, as interpreted from igneous rocks: Science, v. 174, p. 821-825.

MacLeod, N.S., Walker, G.W., and McKee, E.H., 1975, Geothermal significance of eastward increase in age of Upper Cenozoic rhyolitic domes in southeastern Oregon: U.S. Geological Survey Open-File Report 75-348, 21 p.

Meigs, A., Scarberry, K., Grunder, A., Carlson, R., Ford, M.T., Fouch, M., Grove, T., Hart, W.K., Iademarco, M., Jordan, B., Milliard, J., Streck, M.J., Trench, D., and Weldon, R., 2009, Geological and geophysical perspectives on the magmatic and tectonic development, High Lava Plains and northwest Basin and Range, in O'Connor, J.E., Dorsey, R.J., and Madin, I.P., eds., Volcanoes to Vineyards: Geologic Field Trips through the Dynamic Landscape of the Pacific Northwest: Geological Society of America, Field Guide, v. 15, p. 435–470, doi: 10.1130/2009.fl d015(21).

Okure, M.S., 2009, Potential field and seismic geophysical investigations of the American Northwest: Case studies of the observed field anomalies and

application of new seismic attributes methods for data interpretation: PhD Dissertation, University of Oklahoma, 250 p.

Parker, D.J., 1974, Petrology of selected volcanic rocks of the Harney Basin, Oregon, PhD Dissertation, Oregon State University, 227 p.

Peterson, N.V., and Groh, E.A., 1964, Diamond Craters, Oregon: The Ore Bin, v. 26, p. 17-34.

Piper, A.M., Robinson, T.W., Jr., and Park, C.F., Jr., 1939, Geology and ground water resources of the Harney Basin, Oregon: United States Geological Survey Water-Supply Paper 841, 189 p.

Pierce, K.L., and Morgan, L.A., 1992, The track of the Yellowstone hotspot: Volcanism, faulting, and uplift, in Link, P.K., et al., eds., Regional geology of eastern Idaho and western Wyoming: Geological Society of America, Memoir 179, p. 1-53.

Rawlinson, N., de Kool, M. and Sambridge, M., 2006, Seismic wavefront tracking in 3-D heterogeneous media: applications with multiple data classes: Explor. Geophys., 37, p. 322-330.

Rawlinson, N., 2007, Fast Marching Tomography package: Instruction manual, Research School of Earth Sciences, Australian National University, Canberra, ACT 0200, http://rses.anu.edu.au/~nick/fmtomo/instructions.pdf.

Rawlinson, N., and Urvoy, M., 2006, Simultaneous inversion of active and passive source datasets for 3-D seismic structure with application to Tasmania: Geophysical Research Letters, v. 33, L2313.

Rawlinson, N., Tkalčić, H., and Reading, A.M., 2010, Structure of the Tasmanian lithosphere from 3D seismic tomography: Australian Journal of Earth Sciences, v. 57, p. 381-394.

Roche, O., Druitt, T.H., and Merle, O., 2000, Experimental study of caldera formation. Journal of Geophysical Research: Solid Earth (1978–2012), 105(B1), p. 395-416.

Rockett, C.V., 2011, Seismic tomographic imaging reveals possible lithospheric erosion beneath Trans-Pecos Texas and southeastern New Mexico, MS thesis, Baylor University, Waco, Texas, 75 p.

Roth, J.B., Fouch, M.J., James, D.E., and Carlson, R.W., 2008, Three-dimensional seismic velocity structure of the northwestern United States: Geophys. Res. Lett., v. 35, L15304, doi:10.1029/2008GL03466.

Russell, I.C., 1984, A geological reconnaissance in southern Oregon: United States Geological Survey, Annual Report 4, p. 431–464.

Russell, J.K., and Nicholls, J., 1987, Early crystallization history of alkali olivine basalts, Diamond Craters, Oregon: Geochimica et Cosmochimica Acta, v. 51(1), p. 143-154.

Sewell, R. J., Tang, D. L., and Campbell, S. D. G., 2012, Volcanic-plutonic connections in a tilted nested caldera complex in Hong Kong: Geochemistry, Geophysics, Geosystems, v. 13(1), Q01006, doi:10.1029/2011GC003856.

Sheppard, R.A., 1994, Zeolitic diagenesis of tuffs in Miocene lacustrine rocks near Harney Lake, Harney County, Oregon: U.S. Geological Survey, Bulletin 2108, 29 p.

Smith, R. L., and Luedke, R.G., 1984, Potentially active volcanic lineaments and loci in western conterminous United States. In, Explosive Volcanism: Inception, Evolution, and Hazards. edited by J. R. Boyd: National Academy Press, Washington, D.C., p. 47–66.

Song, M., Xie, H., Zhang, Y., Hou, W., Xu, J., and Xu, Y., 1997, P-wave velocities of alkaline olivine basalt at high pressure and temperature and its controlling factors: Chinese Science Bulletin, v. 42, p.761-764.

Streck, M.J., and Grunder, A.L., 1995, Crystallization and welding variations in a widespread ignimbrite sheet; the Rattlesnake Tuff, eastern Oregon, USA, Bulletin of Volcanology, 57(3), p. 151-169.

_____, 2008, Phenocryst-poor rhyolites of bimodal, tholeiitic provinces: the Rattlesnake Tuff and implications for mush extraction models. Bulletin of Volcanology, 70(3), p. 385-401.

_____, 2012, Temporal and crustal effects on differentiation of tholeiite to calcalkaline and ferrotrachytic suites, High Lava Plains, Oregon, USA, Geochem. Geophys. Geosyst., 13, Q0AN02, doi:10.1029/2012GC004237.

Walker, G.W., 1970, Cenozoic ash-flow tufts of Oregon, Oregon Department of Geology and Mineral Industries, report, 32, p. 97-115.

Walker, G.W., 1974, Some implications of Late Cenozoic volcanism to geothermal potential in the High Lava Plains of south-central Oregon, The Ore. Bin, v. 36, p. 109–119.

Walker, G.W., 1979, Revisions to the Cenozoic stratigraphy of the Harney Basin, southeastern Oregon: United States Geological Survey, Bulletin, 1475, p. 1– 35.

Walker, G.W., and Nolf, B., 1981, High Lava Plains, Brothers fault zone to Harney Basin, Oregon, in, Johnson, D.A., and Donnelly-Nolan, J., eds., Guides to some volcanic terranes in Washington, Idaho, Oregon, and northern California: U.S. Geological Survey, Circular 838, p. 105-111.

West, J.D., Fouch, M.J., Roth, J.B., and Elkins-Tanton, L.T., 2009, Vertical mantle flow associated with a lithospheric drip beneath the Great Basin: Nature Geoscience, v. 2, p. 439-444.

Zelt, C.A., and Smith, R.B., 1992, Seismic traveltime inversion for 2-D crustal velocity structure: Geophysics Journal International, v. 108, p. 16-34, doi: 10.1111/ j.1365-246X.1992.tb0083.

Chapter 3: Crustal scale integrated geophysical study of the Snake River Plain, Idaho

Abstract: The scientific discussion on the structural complexities and evolution of the Snake River Plain and the role of extension in its formation has been going on for decades. Similarly, high gravity and magnetic anomalies of the Snake River Plains and their causes are still subjects of many studies. Recent passive and active source seismic studies have specifically focused on the lithospheric and deep mantle structure of the Eastern Snake River Plain and High Lava Plains. However, crustal scale studies of the Western Snake River Plain are limited. In this study, we employed gravity and magnetic data in the area and integrated the results with seismic, geospatial data, and receiver function results to address these issues. We also identified the major differences and similarities in the structure and tectonics of the Western and Eastern Snake River Plain based on gravity and magnetic anomalies. With the help of processed receiver function results, 2D seismic refraction and reflection data, interpreted well logs, and geospatial data, we generated 2D gravity models across the Western Snake River Plain. The mid crustal mafic intrusion is possibly the main reason for the high gravity anomaly in the Western Snake River plain. Alternate gravity model along a profile shows underplating as one of the reasons for the high gravity anomaly at the Western Snake River Plain.

Keywords: *gravity, magnetics, tectonics, crustal structures, integrated modeling*

Introduction

Many scientific questions about the geological structure and tectonic evolution of the Northwestern United States remain unanswered. The Snake River Plain (SRP) is an integral part of the Pacific Northwest and is surrounded by many tectonic units such as; the High Lava Plains (HLP), Idaho Batholith (IB), Basin and Range Province (BRP), Yellowstone (YS), Columbia Plateau (CP), Owyhee Plateau (OwP), and Northern Rocky Mountains (NRM) (Fig. 1). The presence of these tectonic units, effects of flatly subducting Farallon Plate from the west (Schmandt and Humphreys, 2011), long-lived vast Cenozoic volcanic activity in the area, and moving Yellowstone hotspot track make the tectonic evolution of the SRP and its relation to the surrounding units interesting and even more puzzling.

The SRP is relatively low-lying topography, which shows high negative Bouguer anomaly at its center. We used a pre-existing gravity and magnetic database compiled through a community effort. These data are freely available online to download at the Pan American Center for Earth and Environmental Studies (PACES) (http://research.utep.edu/Default.aspx?tabid=37229). We also used more than 1000 recently collected gravity points in the HLP area and merged the data with pre-existing PACES gravity data.

In the regional context of the SRP, the Complete Bouguer Anomaly (CBA) varies by ~210 mGal across its axis. Total Magnetic Intensity (TMI) data were also analyzed. TMI values range over 600 nT with much more complex and erratic magnetic signatures that arise from the shallow flood basalts deposits within the region. We used some wavelength filters to separate regional and residual anomalies such as upward

continuation and bandpass filters for gravity data and reduction-to-pole for the magnetic data. We also applied gradient filters to delineate the boundaries of the gravity and magnetic anomalies such as, tilt derivative, horizontal gradient magnitude, and total horizontal derivative filters. These filters helped us to identify the major structural components and tectonic units in the area. The bounding normal faults of the WSRP are well observed. In addition, we also analyzed the processed receiver function data Gilbert (2012) in the area and generated the crustal thickness map that show slightly thicker crust beneath the WSRP.

We generated an integrated forward gravity model of the subsurface structures across the WSRP and OIG, starting from the OwP on the southwest to the IB on the northeast (Figs. 3.7b, 3.12). This profile passes close to some of the deepest well logs at the center of WSRP (Wood and Clemens, 2002) and is sub-parallel to shallow seismic reflection profiles (Liberty, 1998). These data were used to constrain the upper 5 km of the model along the profile. Another integrated gravity model across the WSRP was generated starting at the northern BRP and ending at the IB (Figs. 3.7b, 3.13, 3.14). This line is sub-parallel to the deep seismic refraction profile by Hill and Pakiser (1967) and reprocessed by Prodehl (1970). The interpreted seismic section along the line is the key constraint for the gravity model for this profile. In both of these models, we modeled high-density, mid-upper crustal mafic intrusive body as a prime source for the anomalous gravity high of the WSRP. We also present an alternate model for the second profile, where we show that the underplating along with a mid crustal mafic sill could partly be the source of gravity high anomaly across the WSRP.

Geological and tectonic settings

The SRP is an arcuate feature, which lies in the southern Idaho. It is filled with large volume of volcanic material, which involves the emplacement of large amounts of mafic magma in the crust. The interaction of the magma is believed to be a major cause for rhyolite and ignimbrite eruption in the SRP (Leeman et al., 2008). The SRP can be divided into Western and Eastern sections according to the internal structures, bounding surfaces, and rock types present in the basins that underlie the plain.

The Western Snake River Plain (WSRP) is a fault-bounded, complex Neogene graben or continental structure trending northwest (e.g. Wood, 1994; Cavanagh, 2000; Wood and Clemens, 2002), which meets the southwest trending Eastern Snake River Plain (ESRP) near Twin Falls, Idaho. It is ~70 km wide and ~300 km long basin that reaches the depth of ~4 km (Wood and Clemens, 2002). The timing of the formation of WSRP has been debated for many years. Mabey (1982) and Malde (1991) suggested that the WSRP formed along with the ESRP at ~17-16 Ma being associated with the large-scale extension of the Basin and Range Province. According to Wood and Clemens (2002), the WSRP basin formation began only after 11 Ma. The silicic volcanism in the WSRP took place at ~12-10 Ma, which was followed by basaltic volcanism in between ~9-7 Ma and later at ~2-0.1 Ma (McCurry et al., 1997). However, the occasional basaltic volcanism continued until several thousand years ago, which are interlayered with sediments.

The ESRP is a ~700 km long, ~100 km wide, and ~5-6 km deep time transgressive, large structural downwarp basin with a number of Quaternary volcanoes that marks the Yellowstone hotspot track (Smith and Braile, 1994; McQuarrie and

Rodgers, 1998; Hughes et al., 1999; Pierce et al., 2002; McCurry and Rodgers, 2009). The ESRP is characterized by accumulation of a thick volcanic succession, crustal flexures on its southern margin, faults in the northwest margins, and significant subsidence along the basin axis (Sparlin et al., 1982). The ESRP has experienced a similar kinematic history to that of northern Basin and Range Province (Rodgers et al., 2002). The rock layers dip towards the axis of the basin (Shervais et al., 2005). The ESRP was formed due to movement of the North American plate over a relatively stationary mantle plume, which lies beneath Yellowstone (YS) caldera now. There is an abundance of Neogene and Quaternary silicic centers and mafic volcanoes observed within the ESRP (e.g. Armstrong et al., 1975; Pierce and Morgan, 1990; Smith and Braile, 1994). The ESRP is also interpreted to be formed due to the interplay of magmatism and the northern Basin and Range extension (e.g. Parsons et al., 1998; McQuarrie and Rodgers, 1998).

The Atlanta lobe of the Cretaceous Idaho Batholith (IB) forms the north side of the WSRP (e.g. Beranek et. al., 2006; Foster et. al., 2001) The IB was formed due to partial melting of the subducting Farallon Plate beneath the continental crust in the Late Cretaceous (Hyndman, 1983). The IB consists of strongly folded metamorphosed granitic-gneiss, granite, tonalite, and quartz diorite. Within the IB, there are a number of volcanic intrusions and mafic dikes.

The Oregon-Idaho Graben (OIG) separates the WSRP from the HLP and OwP to the west. The OIG consists of a series of north trending grabens bounded by faults with average displacements of greater than 1 km. The grabens are filled with tholeiitic basalt sills and dikes, and recent sediments. The basin is also filled with bimodal

volcanic materials (Ferns et al., 1993). The OIG is ~16-10 Ma old and lies within the Middle Miocene back arc rift system that extends from southern Nevada to southeastern Washington (e.g. Cumming et al., 1994; and 2000).

The Basin and Range Province (BRP) lies to the south of the SRP and is an alternating series of north south trending normal fault bounded valleys and mountains that formed during the Cenozoic. The BRP is characterized by comparatively thin crust, widespread seismicity, and extensional fault blocks due to continental rifting (e.g. Thomson et al., 1989; Dewey et al., 1989). BRP consists of Precambrian and Paleozoic rocks often intruded by Cenozoic volcanoes, intrusive rocks, and metamorphic core complex.

The HLP is a Miocene-Pleistocene aged, complex intra-plate bimodal volcanic province, which lies in the west of WSRP (Druken et al., 2011). It is an uplifted plateau covered by rhyolite and basalt and has experienced multiple flood basalt volcanisms (Brueseke et al., 2007), ignimbrite flare-ups (Lipman et al., 1971), and BRP related extension (Camp et. al, 2003). Some hypotheses suggest that the HLP is linked to the Yellowstone mantle plume and the Snake River volcanic system, whereas others suggest that HLP was formed due to upwelling of residual flood basaltic magma (Humphreys et al., 2000). Some others suggest that the HLP could have been developed due to propagating shear zones or due to back arc upwelling in response to the changing subduction geometry in the Pacific Northwest (Christiansen et al., 2002).

Pervious crustal seismic studies

There are limited crustal scale seismic studies across the SRP area, some of which date back as early as 1962. Hill and Pakiser (1967) conducted reversed seismic refraction experiments with five shots from Eureka, Nevada to Boise, Idaho cutting across the WSRP. They interpreted thin (~32 km) crust in the northern BRP, which abruptly changes to ~43 km thick beneath the WSRP and proposed a high velocity mid crustal layer at about 10 km depth beneath the WSRP. This profile was later reprocessed by Prodehl (1970, 1979) showing similar results. The Yellowstone-ESRP seismic profiling experiment was conducted in 1978 to image the crustal structures of Yellowstone region. The profiles ran along as well as cut across the ESRP and used 15 shots covering a distance of 300 km (e.g. Braile et al., 1982; Smith et al., 1982; Sparlin et al., 1982). They found the crust of the ESRP is highly anomalous due to presence of thick volcanic layers, and a high velocity layer (>6.5 km/s) at the intermediate crustal depth. The crustal thickness in the area is ~42 km. Besides these two major crustal scale experiments, the 2008 HLP seismic experiment covers a smaller part of the Owyhee Plateau (OwP), which is close to the WSRP. The crustal thickness in the OwP area is ~38 km and the mid crustal high velocity layer was also imaged (Cox, 2011). Seismic imaging of the Western Idaho- Eastern Oregon (IDOR) experiment was conducted in 2012. The profile cut across the northwest boundary of the WSRP. The results are not available yet, but the key objectives were to find the velocity structure of the entire crust, Moho, and uppermost mantle (http://www.geophys.geos.vt.edu/hole/idor/). The locations of these profiles are shown in Figure 1.

Gravity and magnetic data filtering

In addition to the PACES database for gravity mapping, we also used more than 1000 recently collected gravity data points in the Harney Basin area that lies in the western part of the study area. We gridded the complete Bouguer anomaly (CBA) values of the area with 2 km grid spacing using the Geosoft® Oasis Montaj package. The CBA map of the study area is shown in Figure 3.2(a). A grid spacing of 5 km was used for the magnetic data (Fig 3.5a).

For the detailed analysis, we applied various wavelength filters, such as upward continuation, bandpass, reduction-to-pole, and pseudogravity filters. These filters help to separate the regional anomalies from the residual one. We also applied some edge detecting filters such as tilt derivative and total horizontal derivative (horizontal gradient magnitude) filters to gravity and magnetic data. These filters were useful to delineate the boundaries of major tectonic units and mapping major faults and dikes in the study area. The details of these filters are explained in the following paragraphs.

Upward continuation filter is a low pass filter and helps to separate the regional low pass long wavelength anomalies from residual short wavelength anomalies. Upward continuation transforms the potential field measured on one surface to the other surface as if it was measured on that surface farther from the source (Blakely, 1996). The higher the upward continuation height is used, the smother the anomalies are. A simple upward continuation filter in a Fourier domain is given by (Blakely, 1996):

$$\varphi(X, Y, \Delta Z) = -\frac{1}{2\pi}\frac{\partial \varphi}{\partial \Delta z r} \quad \ldots\ldots\ldots\ldots\ldots\ldots (1)$$

where, $r = \sqrt{x^2 + y^2 + \Delta z^2}$

A residual Bouguer anomaly map after subtracting 40 km upward continuation filter is shown in Figure 3.2b, where major tectonic units in the study area are identified. Figure 3.8 shows the upward continued filtered maps as well as corresponding residual Bouguer maps after subtracting the upward continued grid from the CBA grid.

The bandpass filters are used to separate out residual anomalies from the regional ones. A band of wavelength is selected in such a way that it enhances the anomalies of our interest. One should be very careful in choosing the parameters for wavelength filters properly as the wrong choice could produce maps with artificial ringing effects. Figure 3.4a shows a 10-300 km Butterworth bandpass filtered gravity map, where we observed the gravity anomaly of the SRP as well as other major tectonic units. The reduction-to-pole filter is applied to the magnetic data only. It removes the distortion and asymmetry in the maps caused by Earth's magnetic field and helps to make the actual inclination vertical (e.g. Silva, 1986; Blakely, 1996). This filter is also known as residual filters because it removes the regional effect of the Earth's magnetic field from the magnetic data. Reduced-to-pole total magnetic intensity (TMI) map of the area is shown in Figure 3.5a. Pseudogravity filter is applied to magnetic data, which converts the magnetic anomaly to gravity anomaly in such a way that the mass with magnetic susceptibility would be replaced by the same mass with density (Blakely, 1996). This filter amplifies broader wavelength anomalies while suppressing the shorter wavelength features. Figure 3.5d shows the result obtained after applying pseudogravity filter to reduced-to-pole TMI grid (Fig. 3.5a). This filter largely amplified the SRP anomaly and helped to delineate the ESRP and WSRP related signatures easily.

Total horizontal derivative (THD) filters are edge-detecting filters based on gradient method and is given by (Verduzco et al., 2004)

$$THD = \sqrt{\left(\frac{\partial A}{\partial X}\right)^2 + \left(\frac{\partial A}{\partial Y}\right)^2} \quad \ldots\ldots\ldots\ldots\ldots\ldots\ldots\ldots\ldots\ldots (2)$$

where, A is gravity or the magnetic anomalies from the grid. This filter takes only positive values in account, amplifies the signal, and helps to delineate the boundaries properly. This filter is also known as horizontal gradient magnitude (HMG) filter. Figures 3.5c and 3.9b are examples of THD filters applied to reduced-to-pole TMI maps. In both cases, we can easily see the boundary of SRP and the extending northern Nevada dikes form the BRP area.

Similarly, tilt derivative (TD) is another gradient filter that was applied to the gravity and magnetic data and is given by (Verduzco et al., 2004):

$$TD = tan^{-1}\left(\frac{VD}{THD}\right) \ldots\ldots\ldots\ldots\ldots\ldots\ldots\ldots\ldots\ldots (3)$$

where, *VD* is the vertical derivative of the gravity or magnetic anomalies and is given by$VD = \left(\frac{\partial A}{\partial z}\right)$. Tilt derivatives are very useful to map faults and dikes like linear anomalies. Figures 3.4b is an example of the use of tilt derivative applied to the CBA grid. The results of application of the tilt derivative to the magnetic data are shown in Figures 3.5b and 3.9a, where the boundary of the SRP is enhanced.

Receiver function analysis for crustal thickness mapping

Receiver functions usually are analyzed from the teleseismic waves generated during the earthquake events around the world recorded by broadband seismic stations

(e.g. Ligorría and Ammon, 1999; Langston & Hammer, 2001). In order to produce a receiver function, the horizontal component of the seismogram is deconvolved with the vertical. It produces a time series function that displays P to S converted phases (Burdick and Langston, 1977; Ligorría and Ammon, 1999). After stacking these phases, the time domain data is inverted into the depth domain using widely accepted earth velocity models. When more receiver functions are used from different events at a same station, better crustal properties are estimated. Using the state-of-art statistical tools and measures, crustal thickness (Moho depth) and other crustal properties such as Vp/Vs ratio and Poisson's ratio beneath the seismic station are determined.

US Geological Survey and EarthScope project deployed more than 400 broadband seismometers in the area between the years of 2006 to 2008. EarthScope Automated Receiver functions (EARS) automatically processes and analyzes these seismic data and produces the results. These results provide average estimated crustal thickness, Vp/Vs ratio, and Poisson's ratio beneath these seismic stations. These data are available online for download and analysis (http://ears.iris.washington.edu/).

However, automated results are not always accurate and reliable. If there are other seismic velocity discontinuities strong enough to produce converted P-S phases, the EARS can easily produce false maxima thus creating confusing results specifically in determining the crustal thickness. These discontinuities can be present in form of mafic mid- lower crustal intrusive sills or underplating also known as 7.xx layers (e.g. Rumpfhuber et al., 2009; Shen et al., 2013). These kinds of sub-surface features have been previously reported in the study area (e.g. Brott et al., 1981; Braile et al., 1982; Smith et al., 1982; Sparlin et al., 1982; Shervais et al., 2006; DeNosaquo et al., 2009).

To overcome such issues, we used a secondary database for crustal thickness mapping and analysis. Gilbert (2012) manually analyzed the available teleseismic data from the EarthScope USArray and some other local seismic networks for the western US. About 485 stations in the study area were processed and analyzed. The USArray were ~70 km apart while deployed. In order to combine the receiver function records, Gilbert (2012) stacked the data and binned with binning radius depending upon the density of the stations. He chose 45 km bin spacing in horizontal directions and 1 km in vertical directions. The Moho depths were identified for each station and were compared with the adjacent stations to see the differences. This process helped to validate the results as well as estimate the errors with the help of the bootstrap resampling approach. Gilbert's (2012) receiver function database for the western US is available at http://dx.doi.org/10.1130/GES00720.S1. We downloaded the data and created the crustal thickness map of the study area. The result is shown in Figure 3.10, where the crustal thickness map shows thin crust (~30 km) in the BRP area with the SRP showing relatively thicker crust (~42 km).

Results and discussions

We analyzed the gravity and magnetic data as well as other geospatial database. In addition to it, we also used the receiver function data for mapping crustal thickness. The integrated gravity models across the WSRP were generated with help of the interpreted seismic sections, shallow well logs, digital elevation maps, geological maps, and fault databases. The results are shown in Figures 2 through 14 and are discussed in the following sections.

Gravity and magnetic maps

The CBA map of the study area is shown in Figure 3.2a. The gravity anomaly across the SRP varies by ~210 mGal. The Yellowstone caldera and IB show negative gravity anomalies where as the BRP shows alternating series of gravity highs and lows. For detailed analysis, we generated a residual Bouguer anomaly (RBA) map (Fig. 3.2b) of the area after applying 40 km upward continuation filter. The anomaly in the area varies by ~70 mGal with the SRP showing high positive RBA values. Other major tectonic units such as Columbia River Plateau, accreted Blue Mountains, highly extended BRP, the Northern Rocky Mountains, Idaho Batholith, Yellowstone Caldera, and High lava Plains are easily identified based on the gravity signatures. We took a gravity profile A-A' (Fig. 3.2b) along the SRP/YS and show the result in Figure 3.3. We observed the ESRP gravity anomaly is lower and broader in comparison to that of WSRP, which is higher and narrower. The differences can be observed in both the CBA profile (Fig 3.3a) and RBA profile (Fig. 3.3b). The YS caldera possesses the lowest gravity anomaly in the profile. We applied a 10-300 km Butterworth bandpass filter to the CBA grid and showed the result in Figure 3.4a. The long wavelength features have been removed. It also sharpened the SRP anomaly shown by dotted white polygon. The bandpass filter also amplified the anomalies related to the BRP, Owyhee Plateau, and the High Lava Plains. The tilt derivative map of the area is shown in Figure 3.4b where the dikes of the northern Nevada rift system are mapped (black dotted lines). The boundaries of the SRP are readily identified. The normal faults extending north from the northern BRP (white dashed lines) that cut across the ESRP are also mapped. This filter also amplified the SRP boundary.

We show a series of filtered magnetic maps of the study area in Figure 3.5. Figure 3.5a is a reduced-to-pole total magnetic intensity (TMI) map of the area. The SRP shows weakly organized magnetic anomalies with sporadic signatures within the basin indicating multiple sources of the magnetic signature. The anomalies vary by ~600 nT in the area. The SRP related magnetic anomaly is shown by white ellipses. The dikes of northern Nevada rift (NNR) system are mapped and shown by dashed white lines. We applied Tilt derivative, horizontal gradient magnitude (HGM) and pseudogravity filters to the reduced-to-pole TMI map and show the results in Figures 3.5b, c, and d respectively. The tilt derivative map shows the enhanced boundaries of the WSRP and ESRP. It also amplifies the NNR related dikes. The HGM and pseudogravity filter enhanced and amplified the SRP related anomalies. The sporadic TMI anomaly of the SRP (Fig 3.5a) is more organized and enhanced (Figs. c and d).

We further focused our analysis in the Western Snake River Plain (WSRP) area. Figure 3.6a and b show the CBA and reduced-to-pole TMI map of the WSRP respectively. Major tectonic units and geographic provinces in the area are identified (Fig 3.5a). The magnetic anomaly of the WRSP is shown by the black polygon. The NW boundary of the WSRP is observed better than in the gravity map. Figure 3.7a is the CBA map of the WSRP area with the gravity contour on it. The WRSP shows a series of en echelon gravity high anomaly in its center. The anomaly across the WSRP varies by ~120 mGal, whereas the Idaho Batholith (IB) shows the lowest gravity value in the area. Figure 3.7b is a 40 km upward continued RBA map of the WSRP. The residual gravity values in the area range by ~70 mGal. The Quaternary faults (white dashed lines) show the WRSP anomaly is bounded by normal faults. B-B' and C-C' are

two profiles along which the gravity models are generated. These models will be discussed in the later section and are shown in Figures 3.12 through 3.14. We generated a series of upward continued maps of the WRSP area with upward continuation heights of 10, 20, and 40 km (Figs 3.8a, b, c). Their corresponding residual gravity maps are shown in Figure 3.8d, e, and f. These maps show that the central and eastern WSRP anomalies are related to either narrower or shallower bodies (Figs. a through f) whereas the anomaly in the NW corner of the WSRP is either deep seated or broader (Figs. c and f). We show the filtered tilt derivative map and the HGM map of the reduced-to-pole TMI grid on the WSRP in Figure 3.9a and b respectively. In both cases, these filters highlighted the WSRP boundaries as shown by the dotted black polygons. The WSRP anomalies looks more organized in both cased in comparison to the RTP TMI map (Fig. 3.6b). The tilt derivative filter helped to delineate the dikes of NNR (Fig. 3.9a).

In order to delineate the NW boundary of the WSRP, we further zoomed in into the area. Figure 3.10a and b show 10 km and 40 km upward continued RBA maps respectively. Here the WRSP anomaly is narrow and linear as shown by dashed black polygons. At the NW corner of WSRP, we observed a broader elliptical anomaly as shown by yellow dashed ellipses. We interpret this anomaly to be related to the Columbia River Basalt rather than the WSRP. We also show the Oregon-Idaho Graben (OIG) by a set of black arrows. The OIG separates the WSRP from the Owyhee Plateau and the HLP (Figs. 3.10a and b).

With the help of filtered gravity and magnetic maps, we have interpreted major tectonic units and geographic provinces in the study area. The WSRP anomaly and its boundary are identified.

Receiver function and crustal thickness

We gridded Gilbert's processed and interpreted receiver function data (Gilbert, 2012) to generate a crustal thickness map of the area and show the result on Figure 3.11a. White contours represent Moho depth in the area. The Basin and Range Province has shallow crust with thicknesses varying from ~29-34 km in the BRP area. The WSRP area has crustal thickness of ~40-43 km with the thickness generally increasing toward the southeast. A NE-SW trending linear region of shallow crust (shown by dashed red line) is observed to the west of the WSRP and to the north of the BRP. The crust is ~34-35 km thick in this linear trend. This feature is sub-parallel to the plate boundary and is probably related to the subducting Farallon Plate effect. In order to compare the physical location of this feature (red dashed line), we overlaid the depth contours on a 10 m resolution DEM map of the area (Fig. 3.11b). The linear shallower crustal feature coincides with the Steen's Mountain scarp in the SW portion of the study area. This indicates that there is no deep crustal root present under Steen's Mountain and that Steen's Mountain is isostatically undercompensated. Steens Mountain is located in a broad gravity low (Fig. 3.6) and is associated with only a small positive gravity anomaly even though it is composed of massive basalt flows (Fig. 3.6). The region of thin crust should be a broad gravity high, but the lack of a gravity high suggests that an upper mantle feature must be offsetting the local effects of crustal thinning.

Integrated gravity models across the WSRP

Two profiles across the WSRP were chosen (Fig. 3.7b) to generate integrated gravity models. Different data sources were used as constraints to generate these

models. The key constraint for the gravity model is based on the Eureka- Boise seismic refraction profile (Hill and Pakiser, 1967). The data was reprocessed and interpreted by Prodehl (1970, 1979). The seismic velocities from the profile were converted into density values using the relation between P-wave velocity (*Vp*) and density (ρ) postulated by the Nafe-Drake curve and given by Brocher (2005):

$$\rho(g/cm^3) = 1.6612V_P - 0.4721V_p^2 + 0.0671V_p^3 - 0.0043V_p^4 + 0.0000106V_p^5 \ldots\ldots (4)$$

In addition, we used interpreted logs from geothermal wells, an exploratory well (J.N. James #1) (Wood and Clemens, 2002), and interpreted shallow reflection seismic data (Liberty, 1998) to constraint the upper 5 km of the model specifically around the WSRP and Boise area. Digital surface geological maps and fault maps from USGS were also used to model faults and geological units close to the surface. Crustal thickness estimates from receiver function analysis (Gilbert, 2012) played an important role to decide the Moho depth. The data from Yellowstone-ESRP seismic experiment (Sparlin et al., 1982) were also useful source for the modeling purpose.

The gravity model along profile B-B' is shown in figure 3.12. Major tectonic units are modeled namely the OwP, OIG, WSRP, and IB. The observed and calculated gravity values along the modeled profile match very well with an estimated error of about ± 1.81%. The crustal thickness increases from ~35 km beneath the OwP to ~43 km beneath the IB. A 2.72 g/cm^3 mid crustal layer is modeled beneath the OwP and IB at the depth of 10-20 km but there exist a high-density (2.92 g/cm^3) 8-10 km thick mafic intrusive body in the mid-crust beneath the WSRP. This body is probably the source of

the mafic material in the upper crust. The OIG, filled with bimodal igneous rocks was also modeled that separates the WSRP from the OwP.

Similarly, the gravity model along profile C-C' is shown in Figure 3.13. This profile starts northern BRP cut across the WSRP and end in the IB. The Moho beneath the BRP area is ~31 km and jumps to ~41 km beneath the WSRP as suggested by Hill and Pakiser, (1967) and Gilbert, (2012). We modeled a high density (2.92 g/cm^3) mid to upper crustal mafic intrusive body similar to that of profile B-B'. The mismatch error between the observed and calculated gravity value in this model is ±1.51.

The WSRP area contains a series of normal faults, which are associated with graben and half graben structures. These grabens are filled with inter-layered sediments and flood basalt flows. These faults are terminated by the high-density mafic intrusion (Figs. 3.12 and 3.13). In the center of WSRP, a horst block is also observed. The density of these sedimentary interlayerings and the flood basalt in these blocks ranges from 2.34-2.78 g/cm^3. The Idaho Batholith is made up of ~8-10 km thick granite, granodiorite body with density of 2.65 g/cm^3, which is often intruded by mafic volcanics (Figs. 3.12 and 3.13). The presence of this high-density body may be interpreted as mafic layer that rose from the upper mantle through the fractures crust and solidified in the mid crust (e.g. Sparlin et al., 1982; Shervais et al., 2005). The mid crust of the SRP has been interpreted as high density, high velocity body by previous researchers also. Mabey (1976) and Prodehl (1979) proposed a similar model with high density mid crustal body for the WSRP whereas Sparlin et al. (1982) and Shervais et al., (2005) have proposed similar models for the ESRP. For both of these models we showed the gravity high of the WSRP is contributed by the mid crustal layer.

We proposed an alternate model along profile C-C' and showed the result in Figure 3.14. Instead of using a high-density massive mafic intrusive body in the mid crust, we modeled an underplating layer with a density of 3.10 g/cm^3 right above the Moho and used a mid crustal dike with density of 2.92 g/cm^3. Most of the other layers and their densities are similar to that of Figure 3.13. The mismatch error between the observed and calculated gravity value in this model is ±1.70. This alternate model showed that the gravity high of the WSRP is partially related to the underplating and partially to the mid crustal mafic dike. Similar model has been purposed for the ESRP by Shervais et al. (2005).

Conclusions

We employed freely available potential field data in an integrated analysis to estimate and understand the complex crustal structure of the SRP. Basic wavelength filters and derivative filters enhanced the anomalies and helped to identify the key tectonic units and geographic provinces. The boundaries of these tectonic units were identified being based on the gravity and magnetic signatures on the filtered maps. The gravity profiling along the SRP, shows that the anomalies of the WSRP and ESRP are slightly different. The WSRP anomalies are narrower and higher indicating possible shallower source while the ESRP anomaly are broader and lower, indicating relatively deeper sources. With the help of derivative filters, we mapped major dikes such as Northern Nevada dikes. Some of the normal faults that extend north from the BRP were mapped across the ESRP area as well. We were also able to delineate the boundary of the WSRP with help of filtered maps. The crustal thickness map of the area showed that the WSRP has slightly thicker crust in comparison to the surrounding units. The NNE-

SSW trending slightly thinner crust aligns sub-parallel to the plate boundary. We interpret this feature as possible underplating due to the subduction of the Farallon plate.

The gravity models show that the WSRP is a fault bounded graben structure. These faults are terminated by a high density mid crustal mafic intrusive body. The grabens are filled with interlayers of basalt and sediments. We interpret this mafic body as a sill/dike that was formed due to the partial melt rising from the upper mantle through the fractured crust. Our alternate gravity model suggests that an underplating layer may exist beneath the WSRP. In either case, the mid crustal high density mafic body is evident regardless to its size. This indicates that even though the ESRP and WSRP look different in their topographic signatures and shallow geological structures, there is not much significant difference in terms of the crustal scale features. The crustal modification is essential but to decide its depth and size, higher resolution geophysical data are required.

Acknowledgements

We would like to acknowledge Pan American Center for Environmental Studies (PACES) and US Geological Survey for excellent data management and data availability. We cordially thank Dr. Hersh Gilbert for providing with the processed receiver function data. We would also like to thank Dr. Kevin Crain and Stephen Holloway for all sorts of technical supports. Our special thanks go to Dr. Spencer Wood and Lee Liberty from Boise State University for their help and support during the field visits.

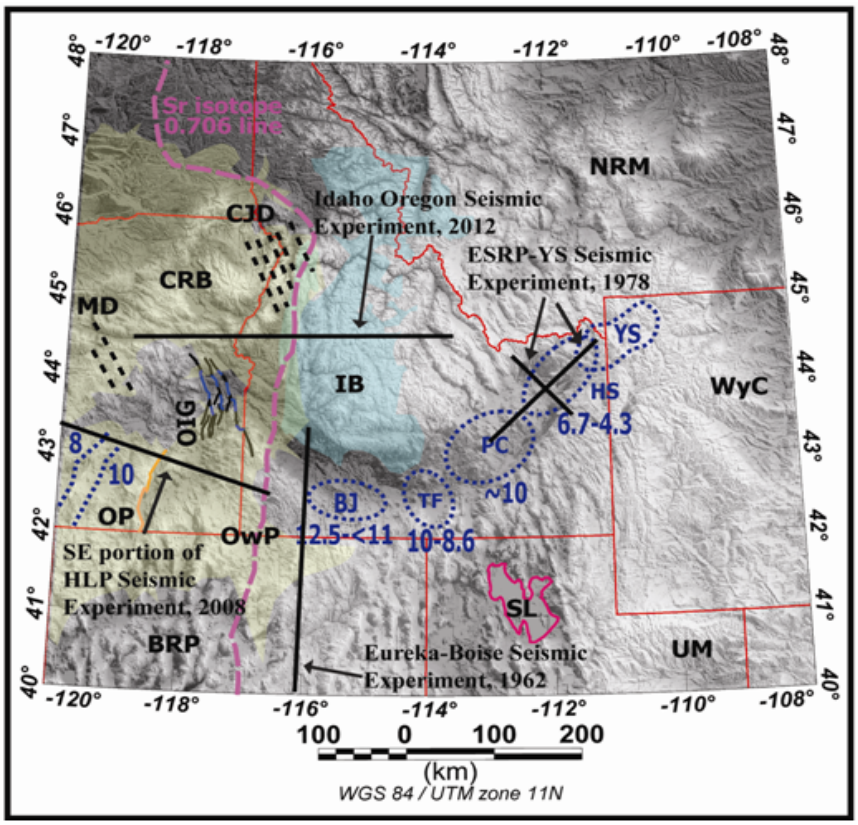

OP: Oregon Plateau	OIG: Oregon-Idaho Graben
MD: Monument Dike Swarm	CJD: Chief Joseph Dike Swarm
SL: Salt Lake	BJ: Bruneau Jarbridge Caldera
TF: Twin Falls Caldera	PC: Picabo Caldera
HS: Heise Volcanic Field	YS: Yellowstone Caldera
NRM: Northern Rocky Mountain	WyC: Wyoming Craton
BRP: Basin and Range Province	IB: Idaho Batholith
CRB: Columbia River Basalt	OwP: Owyhee Plateau
UM: Uinta Mountain	

Figure 3.1: Index map of the study area showing major tectonic units and geographic provinces. Major volcanic centers of the Snake River plain/Yellowstone track are shown in blue eclipses with their successive ages. Sr 0.706 line separates the Cratonal North America from the subducting Pacific Plate. The geospatial information is based on the previous works by Wagner et al. (2010) and Eager et al. (2011). Major crustal scale seismic studies and their location are also shown by black lines.

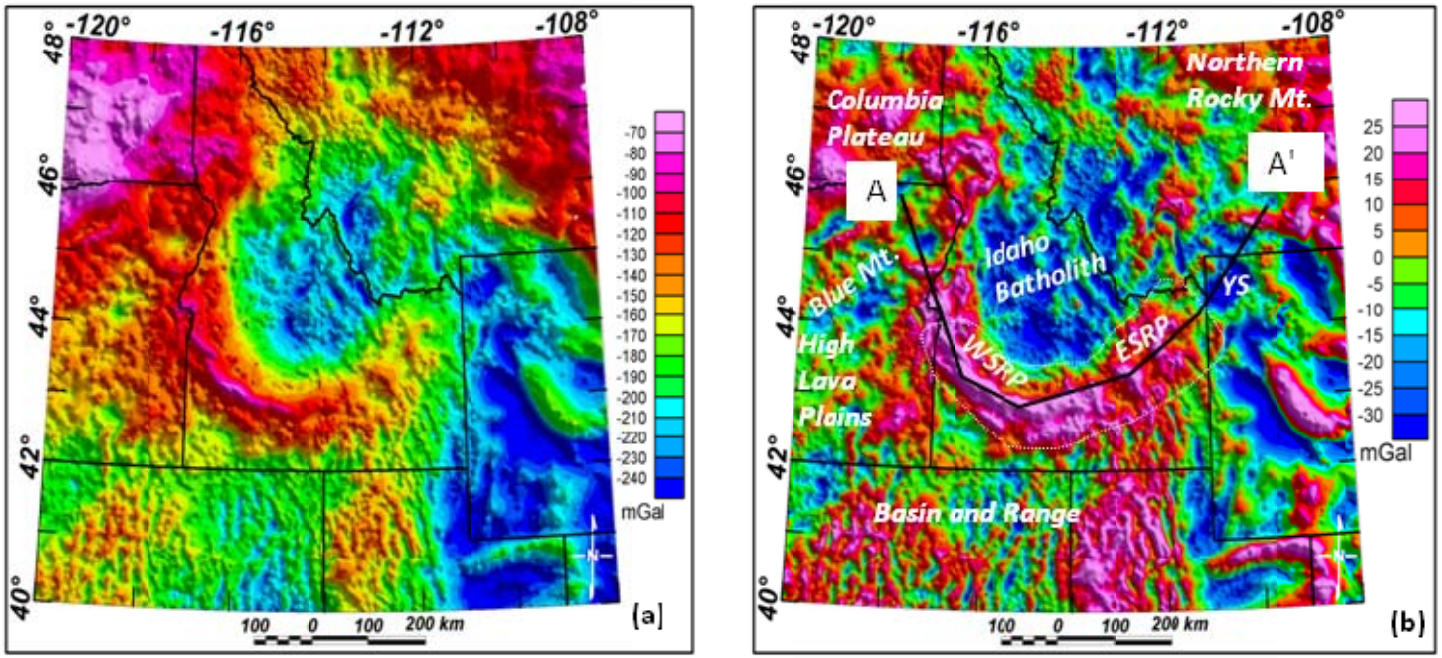

Figure 3.2: Bouguer anomaly maps of the study area: (a) complete Bouguer anomaly (CBA) and (b) residual Bouguer anomaly (RBA) map after applying 40 km upward continuation filter to the CBA grid. Major tectonic units and geographical provinces are identified in the RBA map. YS, WSRP, and ESRP stand for Yellowstone, Western Snake River Plain, and Eastern Snake River Plain respectively.

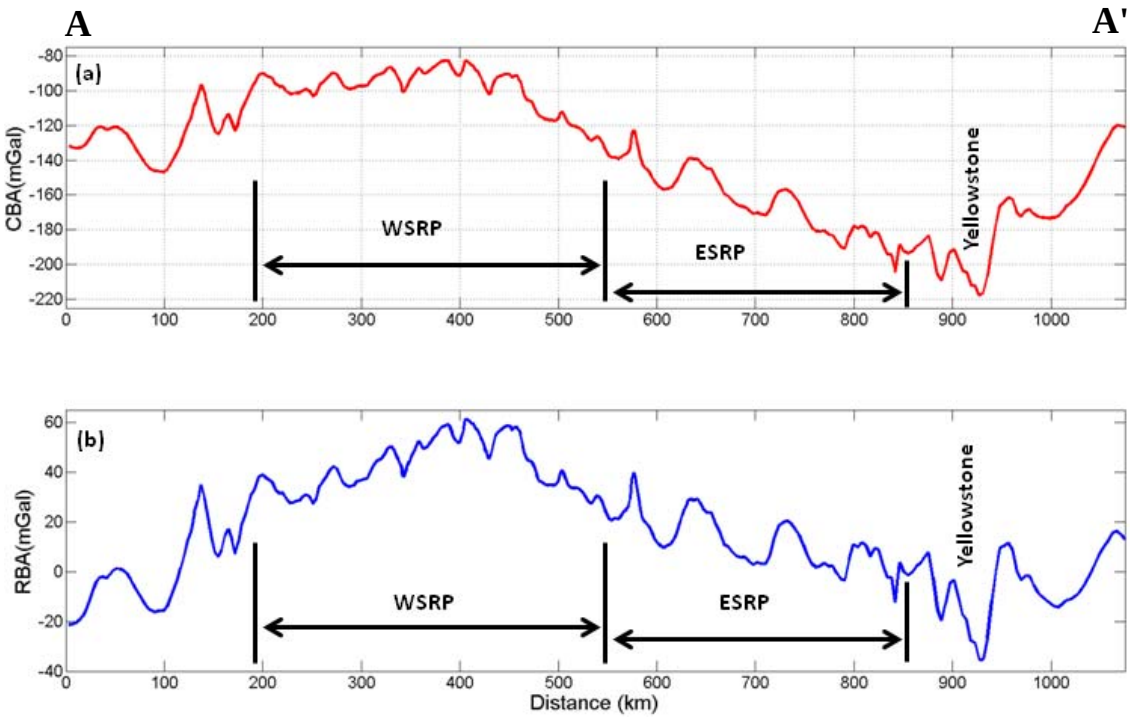

Figure 3.3: Bouguer anomaly profiles along the axial Snake River Plain along A-A' in Figure 3.2b: (a) complete Bouguer anomaly (CBA) and (b) residual Bouguer anomaly (RBA) after applying 40 km upward continuation filter. The ESRP and WSRP show some difference in gravity anomaly.

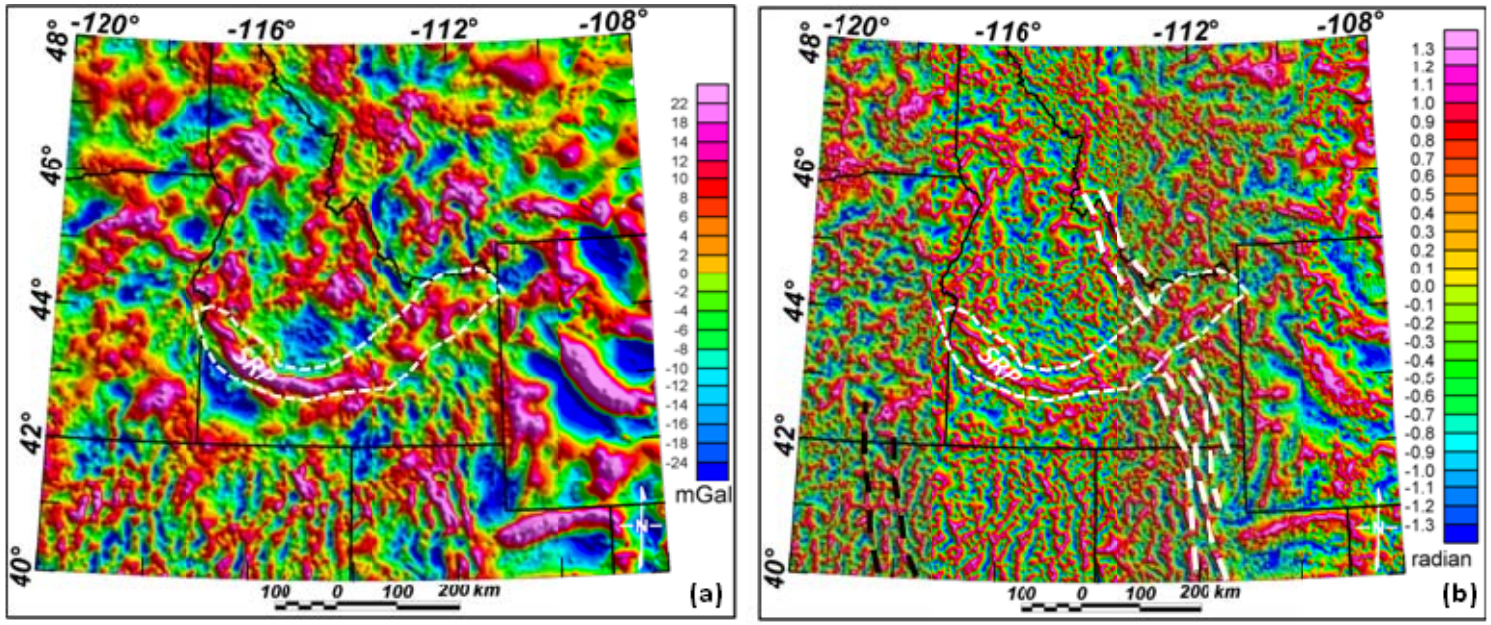

Figure 3.4: Filtered Bouguer anomaly maps of the study area: (a) 10–300 km Butterworth bandpass filter applied to complete Bouguer anomaly (CBA) map and (b) tilt derivative map applied to the CBA grid. The northwest boundary of the WSRP is terminated by the southern part of the Columbia River Basalt. The dikes from the northern Nevada rift system are shown. The Normal faults, that extend from the northern Basin and Range province cross across the eastern Snake River Plain shown my black lines in Figure (b).

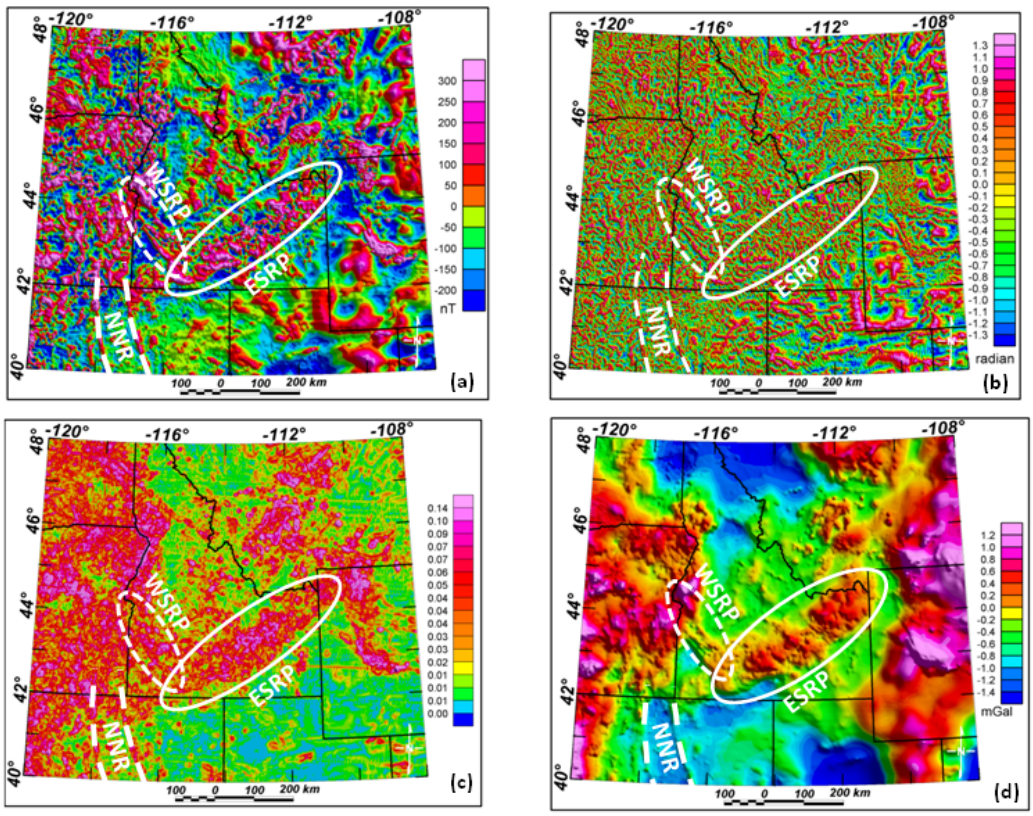

Figure 3.5: Filtered magnetic maps of the study area: (a) Residual total magnetic intensity (TMI) map after reduction to pole, (b) tilt derivative map applied to the reduced-to-pole TMI, (c) horizontal gradient magnitude (HGM) map of the reduced-to-pole TMI, and (d) pseudogravity map of the reduced-to-pole TMI. The WSRP anomaly is linear and confined in comparison to that of the ESRP, which is broad and sporadic. The Northern Nevada rift system (NNR) is shown.

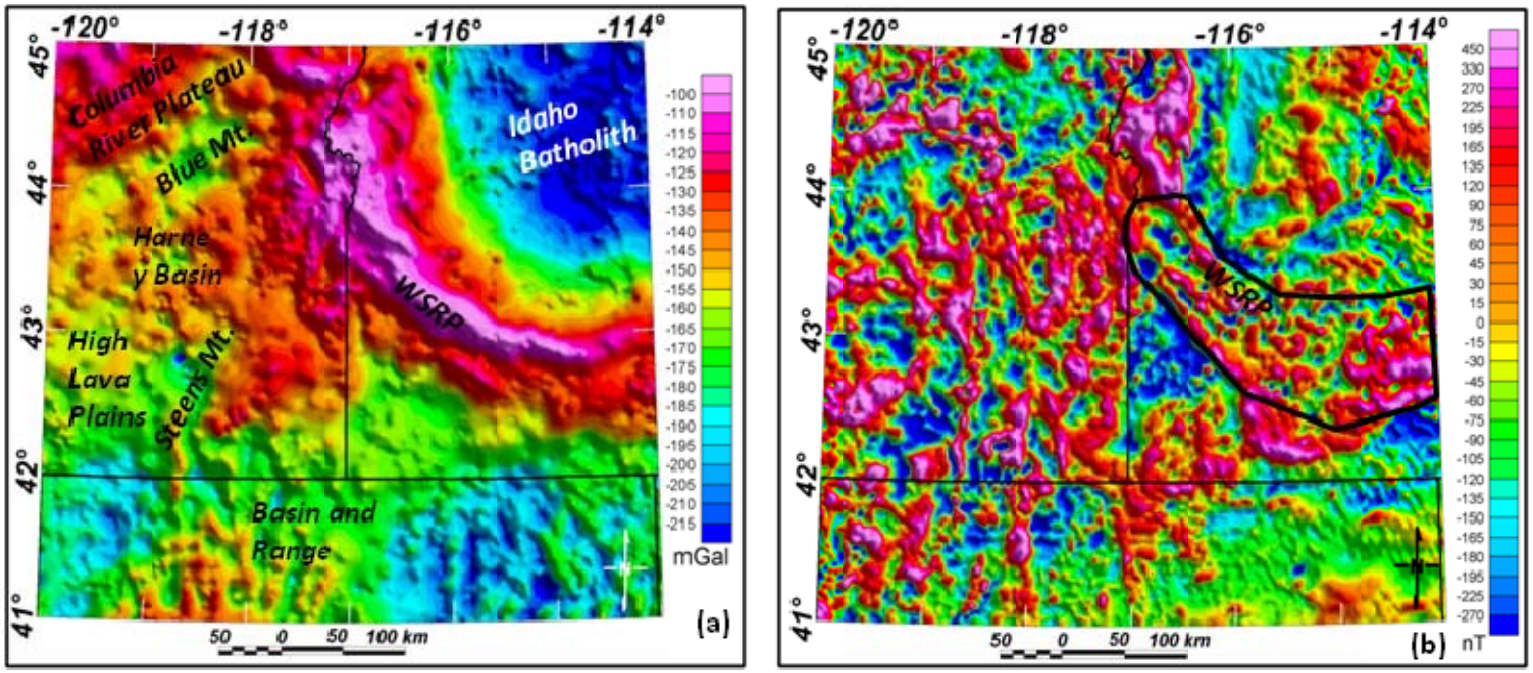

Figure 3.6: Gravity and magnetic maps of the Western Snake River Plain. (a) The CBA map of the area with major tectonic units and geographic features mapped. (b) the reduced-to-pole TMI map, where the WSRP is shown by black polygon.

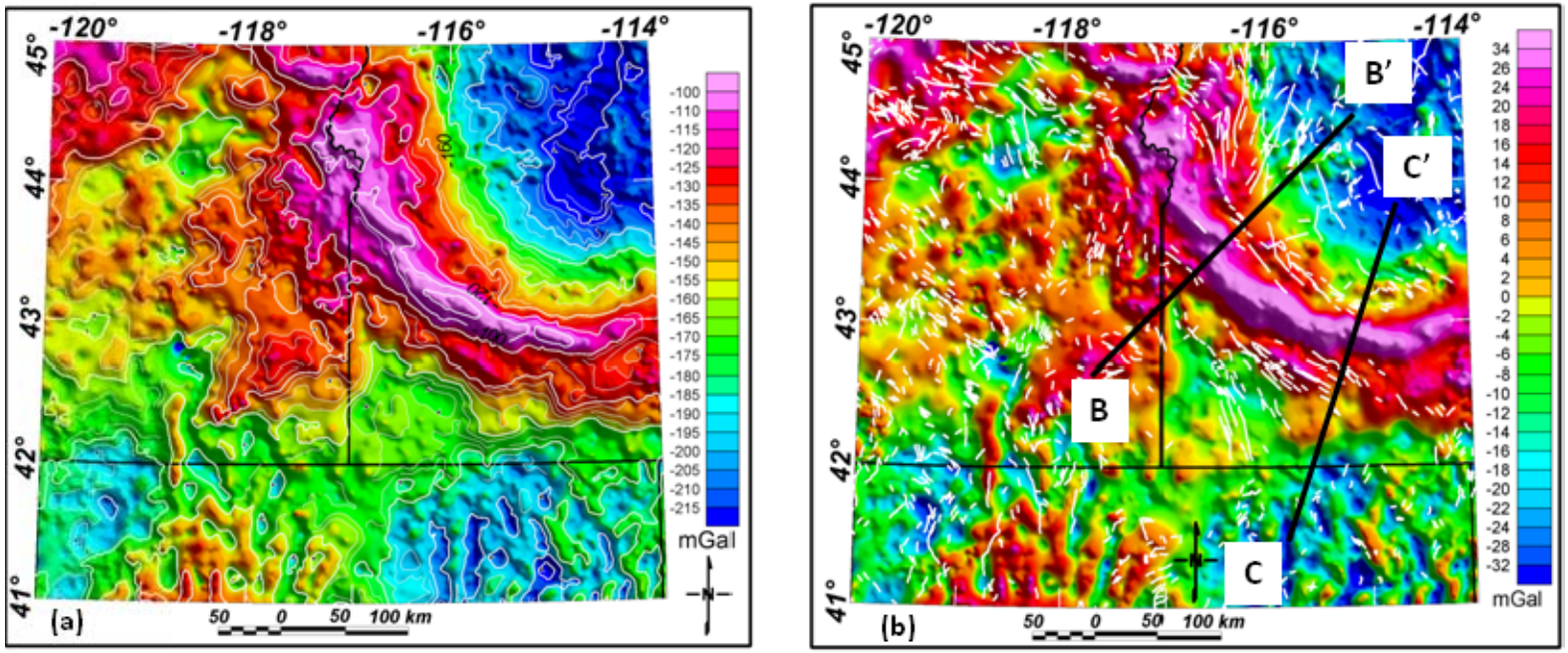

Figure 3.7: Gravity maps of the Western Snake River Plain. (a) The CBA map of the area with gravity contour on it and (b) 40 km upward continues residual Bouguer anomaly map on the WSRP area. B-B′ and C-C′ are two profiles along which the gravity model are made and shown in Figures 3.12, 3.13, and 3.14.

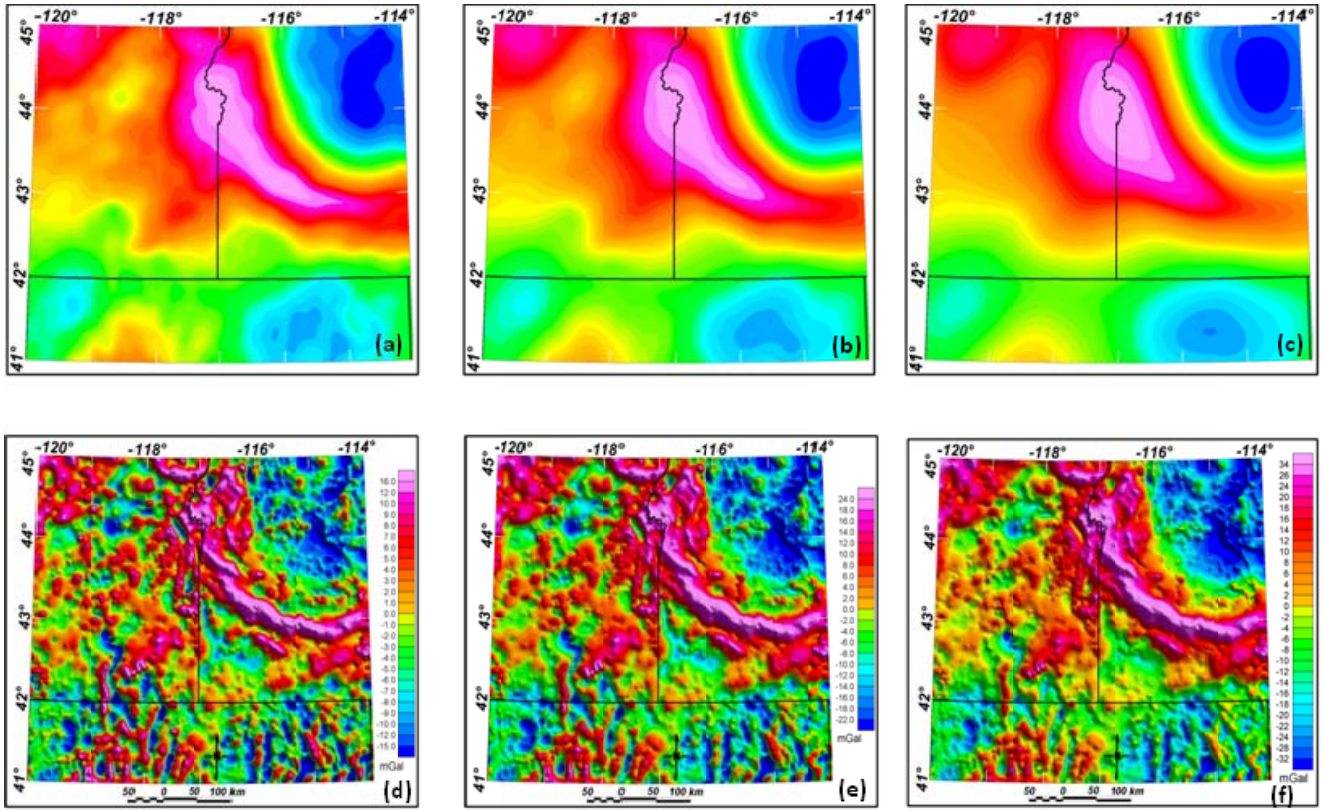

Figure 3.8: Filtered gravity maps of the WSRP. Figures (a), (b), and (c) are 10 km, 20 km and 40 km upward continuation filters applied to CBA map (Fig. 3.6a). Figures (d), (e), and (f) are 10 km, 20 km, 40 km residual Bouguer anomaly map of the study area after subtracting grid (a), (b), and (c) from CBA grid.

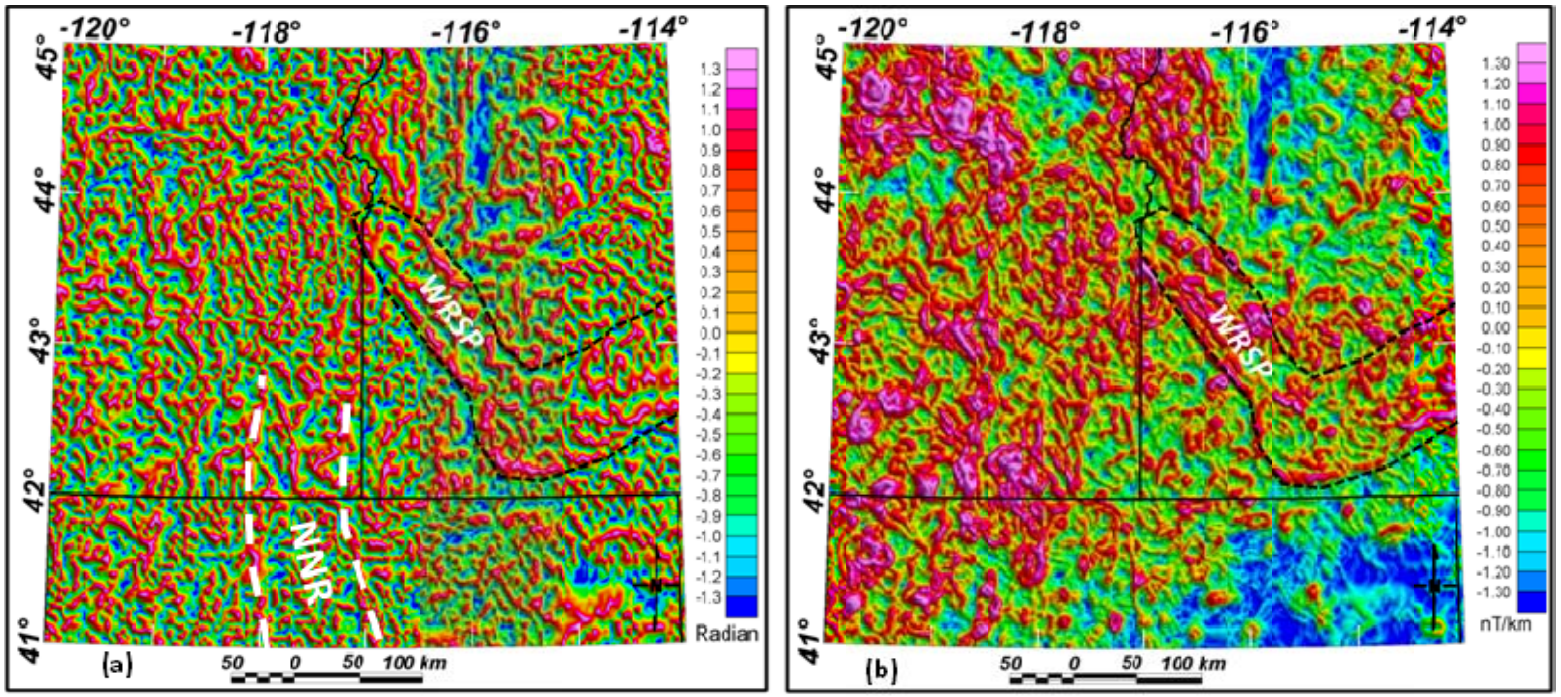

Figure 3.9: Filtered magnetic map of the WSRP area. (a) tilt derivative map of the reduced-to-pole TMI grid and (b) horizontal gradient magnitude map of the reduced-to-pole TMI grid. The boundary of the Western Snake River Plain (WSRP) is well defined by comparatively organized magnetic anomaly than that of surrounding regions in both cases.

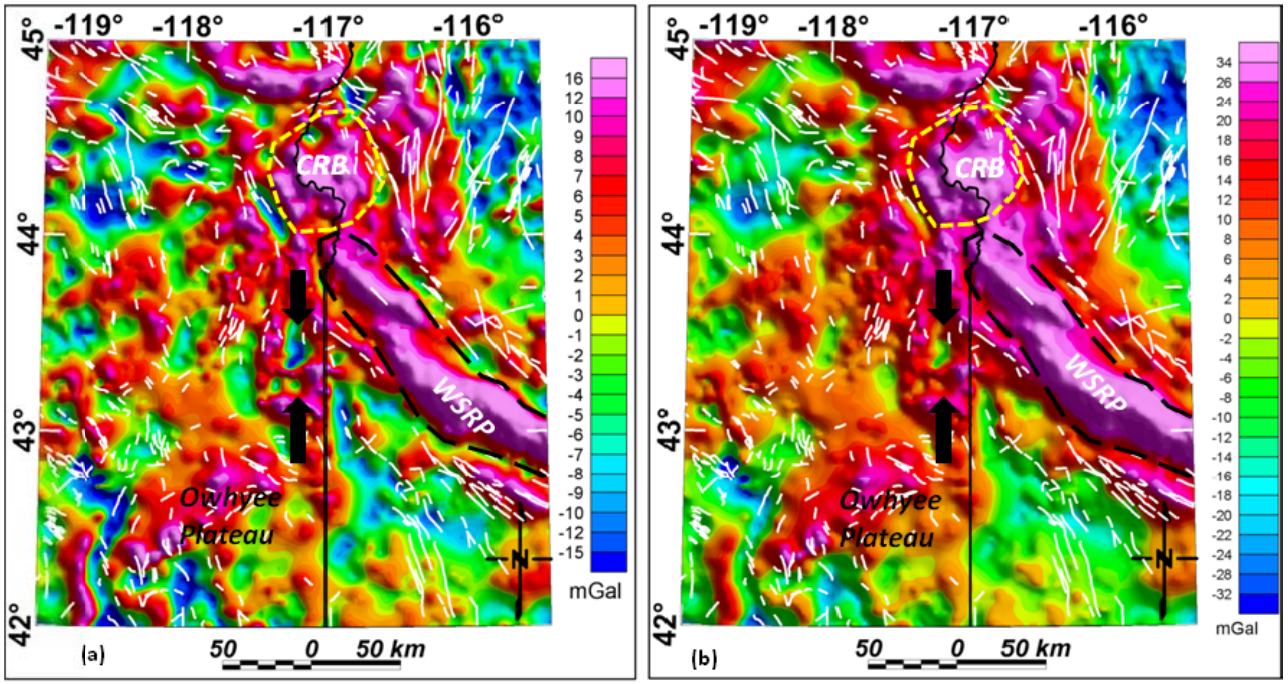

Figure 3.10: Gravity maps around the northwestern edge of the Snake River Plain. (a) 10 km upward continued residual Bouguer anomaly map and (b) 40 km upward continued residual Bouguer anomaly. The central gravity high related to the WSRP is shown by dashed black polygons on both Figures. Anomaly in dashed yellow polygons show boarder elliptical shape in comparison to narrower linear anomaly of the WSRP. White dashed lines are mapped Quaternary faults in the area. Oregon- Idaho Graben is shown by a pair of black arrows.

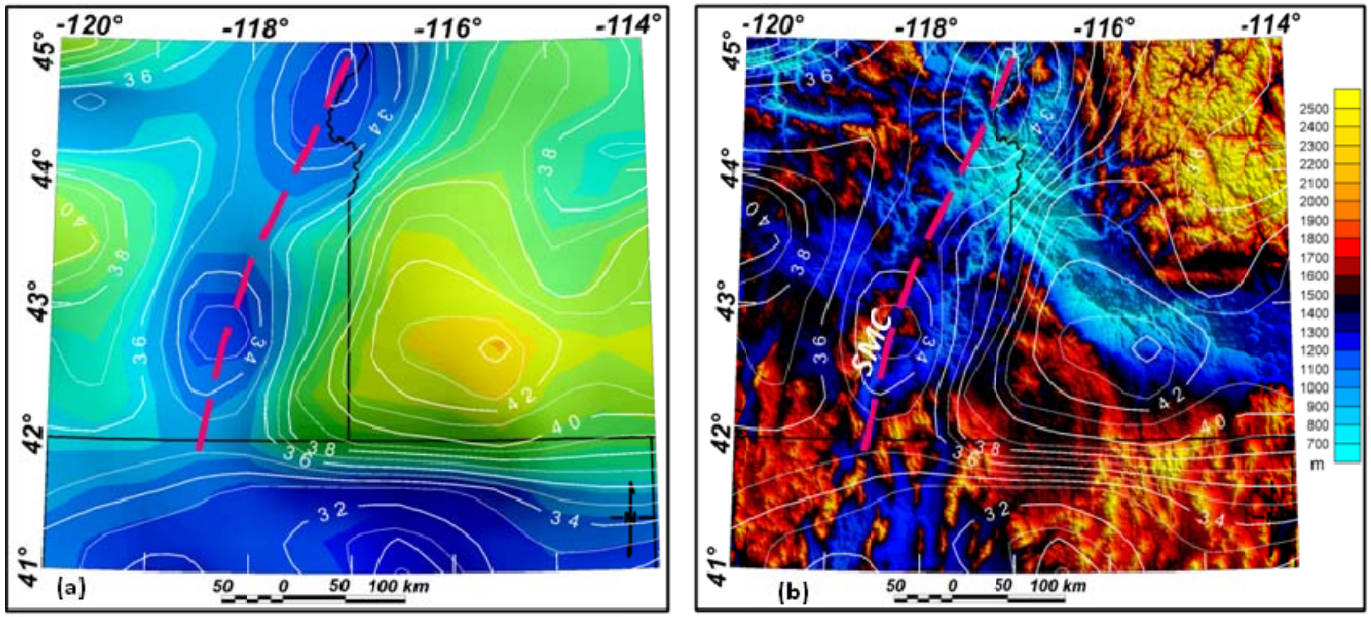

Figure 3.11: Crustal thickness map of the WSRP area shown in Figure (a) after using processed receiver function data by Gilbert (2012). White contours represent Moho depth in the area. The Basin and range province have shallow crust as expected with crustal thickness increasing toward NE. The WSRP area has crustal thickness of ~40-43 km. A NE-SW trending linear shallow crust (dashed red line) is observed probably related to possible underplating. The contours are dropped in a 10 m resolution DEM map of the area and are shown in Figure (b). The NE-SW trending shallower crustal coincide with the Steen's Mountain Scarp (SMC) in the SW area.

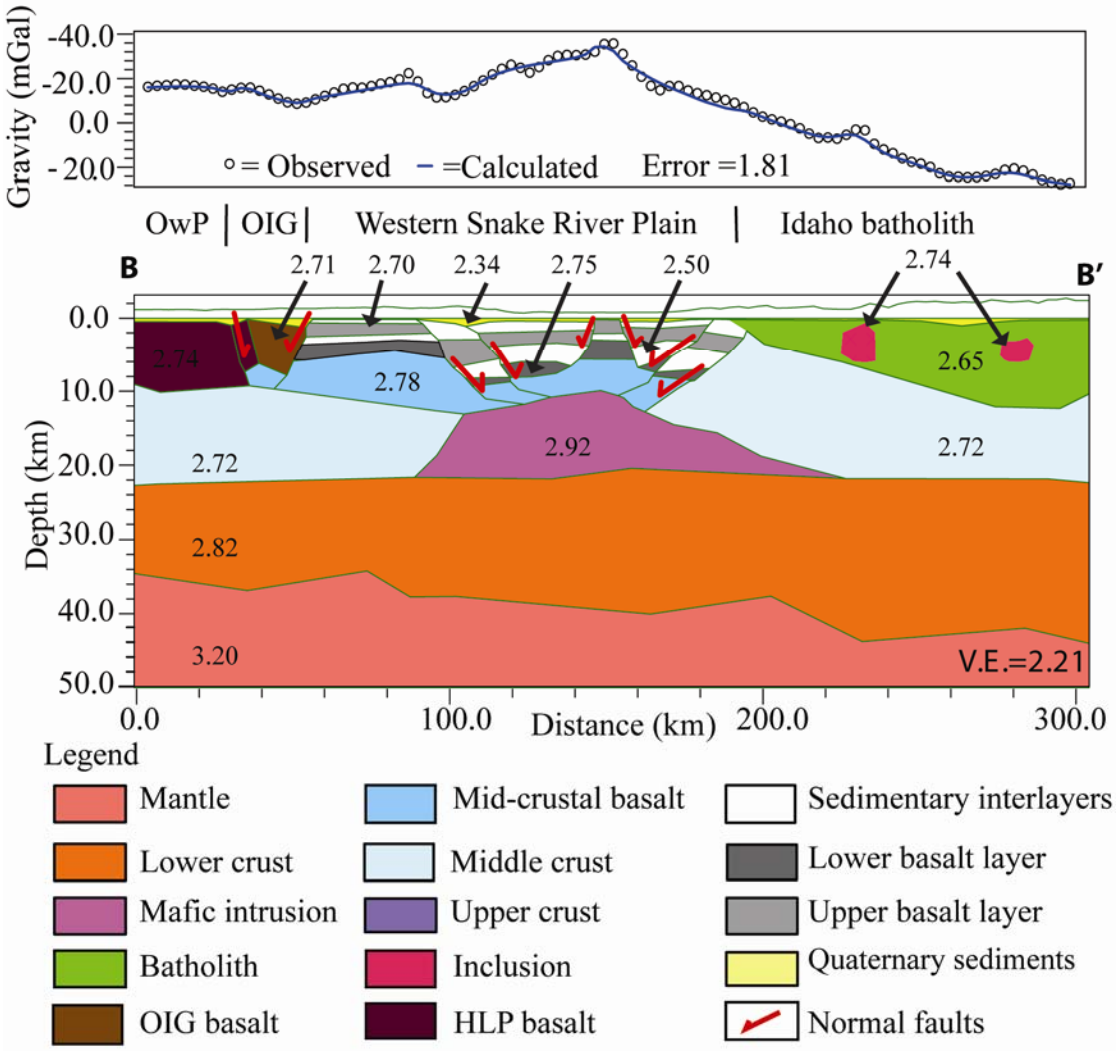

Figure 3.12: Gravity model across the Western Snake River Plain from Owyhee Plateau (OwP) through Oregon-Idaho Graben (OIG) to the Idaho batholith along B-B′(Fig. 3.7b) based on gridded 40 km upward continued residual Bouguer anomaly. Mid to upper crustal mafic intrusive body is modeled as a major source for high gravity anomaly across the Snake River Plain. The density values are in g/cm^3.

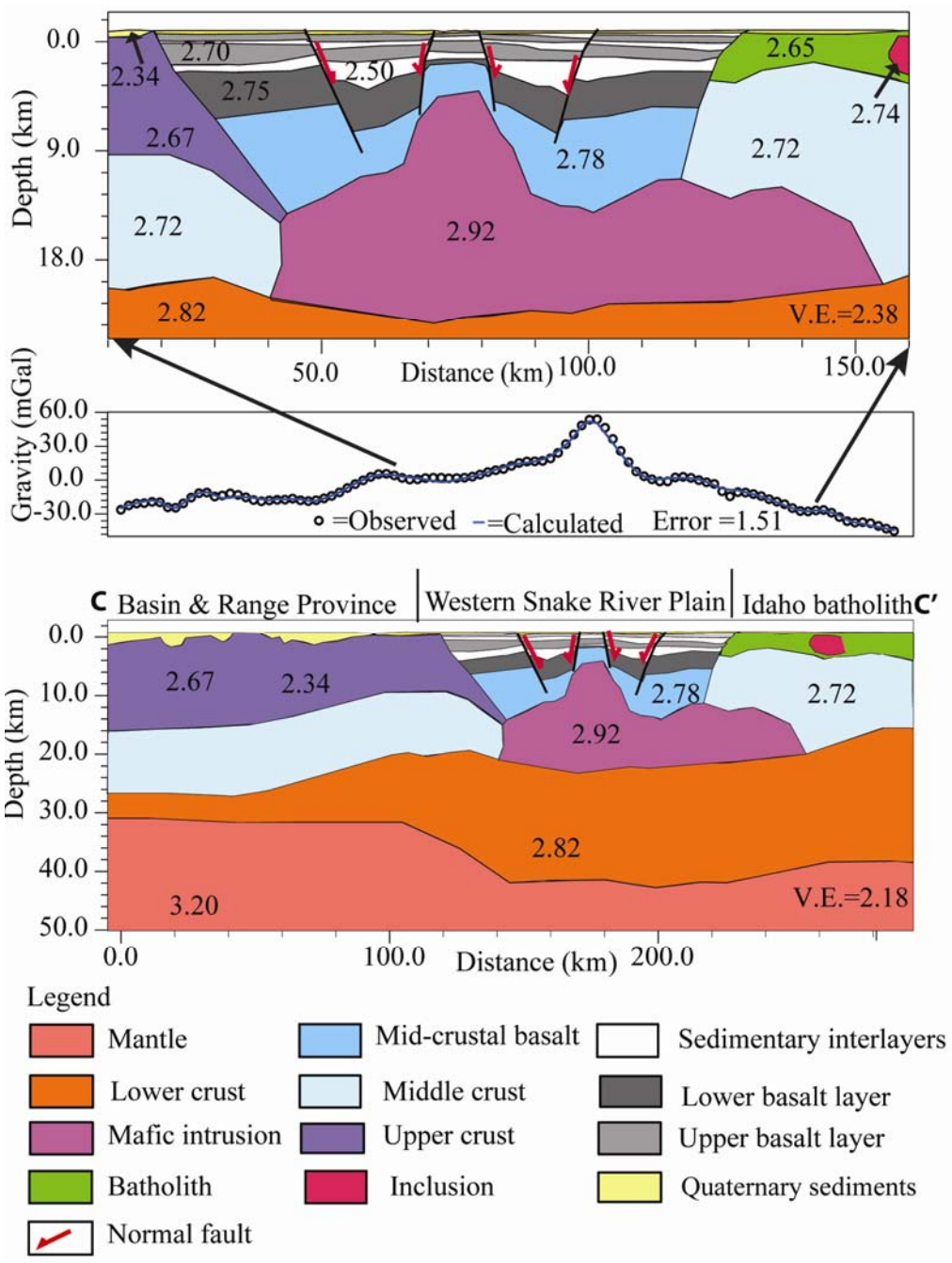

Figure 3.13: Gravity model across the Western Snake River Plain sub-parallel to Hill and Pakiser (1967) seismic refraction line along C-C′ (Fig. 3.7b) based on gridded 40 km upward continued residual Bouguer anomaly. Mid to upper crustal mafic intrusive body is modeled as a major source for high gravity anomaly across the Snake River Plain. The density values are in g/cm^3.

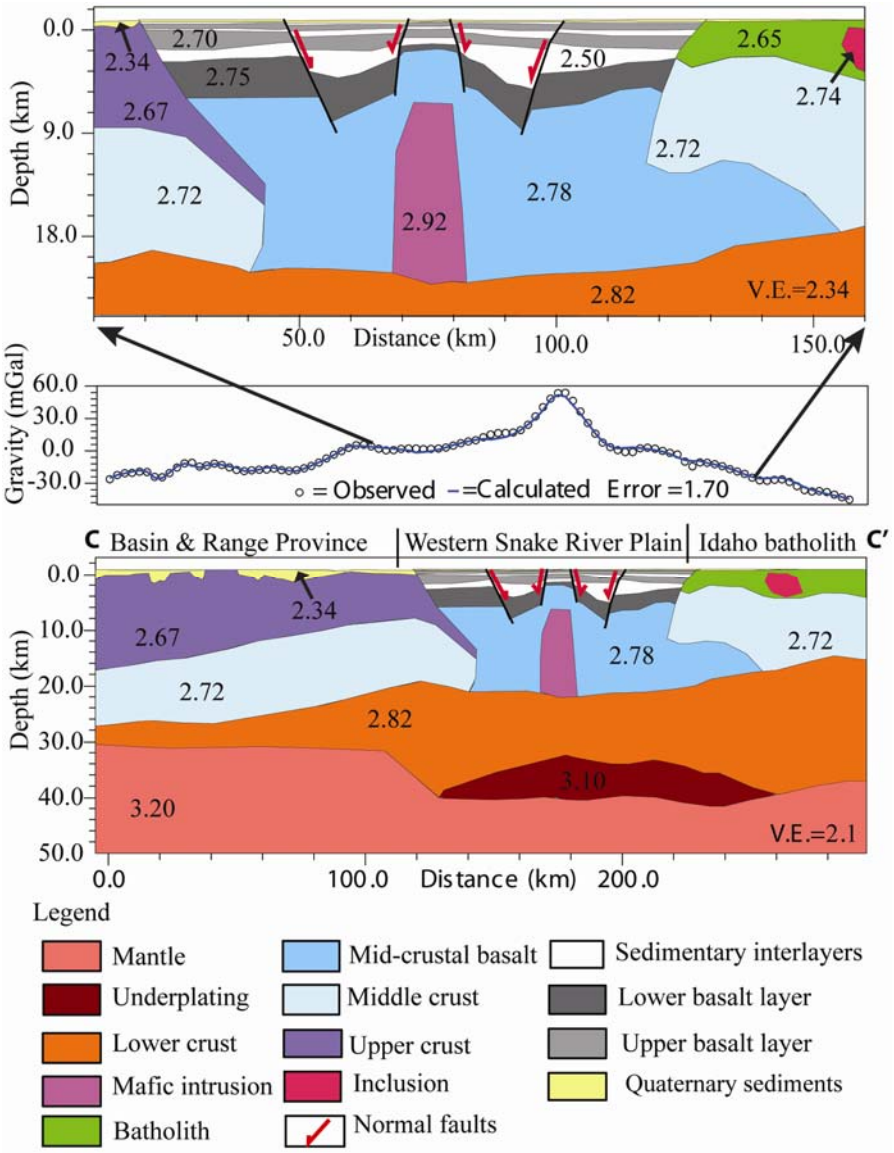

Figure 3.14: Gravity model across the Western Snake River Plain sub-parallel to Hill and Pakiser (1967) seismic refraction line along C-C′ (Fig. 3.7b) based on gridded 40 km upward continued residual Bouguer anomaly. In addition to mid to upper crustal mafic intrusive dike, we modeled some underplating that can produce high gravity anomaly across the Snake River Plain. The gravity high is partially related to the possible underplating and partially to the mid to upper crustal mafic intrusion. The density values are in g/cm^3.

References

Armstrong, R.L., Leeman, W.P., and Malde, H.E., 1975, K-Ar dating, Quaternary and Neogene volcanic rocks of the Snake River Plain, Idaho: American Journal of Science, v. 275, p. 225-251.

Beranek, L.P., Link, P.K., and Fanning, C.M., 2006, Miocene to Holocene landscape evolution of the western Snake River Plain region, Idaho: Using the SHRIMP detrital zircon provenance record to track eastward migration of the Yellowstone hotspot. Geological Society of America Bulletin, 118(9-10), p. 1027-1050.

Blakely, R. J., 1996, Potential theory in gravity and magnetic applications: Cambridge University Press, 441p.

Braile, L.W., Smith, R.B., Ansorge, J., Baker, M.R., Sparlin, M.A., Prodehl, C., Schilly, M.M., Healy, J.H., Mueller, S., and Olsen, K.H., 1982, The Yellowstone-Snake River Plain seismic profiling experiment: Crustal structure of the Eastern Snake River Plain, Journal of Geophysical Research: Solid Earth (1978–2012), 87(B4), p. 2597-2609.

Brocher, T.M., 2005, Empirical relations between elastic wave speeds and density in the Earth's crust, Bulletin of the Seismological Society of America, v. 95, no. 6, p. 2081-2092.

Brott, C.A., Blackwell, D.D., and Ziagos, J.P., 1981, Thermal and tectonic implications of heat flow in the Eastern Snake River Plain, Idaho, Journal of Geophysical Research: Solid Earth (1978–2012), 86(B12), p. 11709-11734.

Burdick, L.J., and Langston, C.A., 1977, Modeling crustal structure through the use of converted phases in teleseismic body-wave forms, Bulletin of the Seismological Society of America, 67(3), p. 677-691.

Brueseke, M.E., Heizler, M.T., Hart, W.K., and Mertzman, S.A., 2007, Distribution and geochronology of Oregon Plateau (U.S.A.) flood basalt volcanism: the Steens

Basalt revisited, Journal of Volcanology and Geothermal Research, v. 161, p. 187-214, doi:10.1016/j.jvolgeores.2006.12.004.

Camp, V.E., Ross, M.E., and Hanson, W.E., 2003, Genesis of flood basalts and Basin and Range volcanic rocks from Steens Mountain to the Malheur River Gorge, Oregon. Geo. Soc. Am. Bull., v. 115(1), p. 105-128.

Cavanagh, B.C., 2000, Western Snake River Plain, Idaho, fluvial-lacustrine sediments: Exhumation estimates from mudstone compaction, unconformity identification by buried soil carbonate, hydraulic conductivity estimates from well cuttings, MS thesis, Boise State University, Boise, 96 p.

Christiansen, R.L., Foulger, G.R., and Evans, J.R., 2002, Upper-mantle origin of the Yellowstone hotspot, Geological Society of America Bulletin, 114(10), p. 1245-1256.

Cox, C., 2011, A controlled source seismic and gravity study of the High Lava Plains (HLP), Master's Thesis, University of Oklahoma, 110 p.

Cummings, M.L., Evans, J.G., and Ferns, M.L., 1994, Stratigraphic and structural evolution of the middle Miocene Oregon-Idaho graben Malheur County, Oregon, in Swanson, D.A., and Haugerud, R.S., eds., Geologic field trips in the Pacific Northwest, Geological Society of America Annual Meeting, Seattle, Washington, v. 1, p. lG-1–lG-20.

Cummings, M.L., Evans, J.G., Ferns, M.L., and Lees, K.R., 2000, Stratigraphic and structural evolution of the middle Miocene synvolcanic Oregon-Idaho Graben, Geological Society of America Bulletin, 112(5), p. 668-682.

Dewey, J.W., Hill, D.P., Ellsworth, W.L., and Engdahl, E.R., 1989, Earthquakes, faults, and the seismotectonic framework of the contiguous United States, in Pakiser, L.C., and Mooney, W.D., eds., Geophysical framework of the continental United States: Geological Society of America Memoir 172.

DeNosaquo, K.R., Smith, R.B., and Lowry, A.R, 2009, Density and lithospheric strength models of the Yellowstone–Snake River Plain volcanic system from gravity and heat flow data, Journal of Volcanology and Geothermal Research, 188(1), p. 108-127.

Druken, K.A., Long, M.D., and Kincaid, C., 2011, Patterns in seismic anisotropy driven by rollback subduction beneath the High Lava Plains, Geophysical Research Letters, v. 38, p. L13310, doi:10.1029/2011GL047541.

Eagar, K.C., Fouch, M.J., James, D.E., and Carlson, R.W., 2011, Crustal structure beneath the High Lava Plains of eastern Oregon and surrounding regions from receiver function analysis, Journal of Geophysical Research: Solid Earth, 116(B2). p. 1978–2012.

Ferns, M.L., Brooks, H.C., Evans, J.G., and Cummings, M.L., 1993, Geologic map of the Vale 30x60 minute quadrangle, Malheur County, Oregon, and Owyhee County, Idaho: Oregon Department of Geology and Mineral Industries Map GMS-77, scale 1:100,000.

Foster, D.A., Schafer, C., Fanning, C.M., and Hyndman, D.W., 2001, Relationships between crustal partial melting, plutonism, orogeny, and exhumation: Idaho-Bitterroot batholith: Tectonophysics, v. 342, p. 313–350, doi: 10.1016/S0040-1951(01)00169-X.

Gilbert, H., 2012, Crustal structure and signatures of recent tectonism as influenced by ancient terranes in the Western United States, Geosphere, 8(1), p. 141-157.

Hill, D.P., and Pakiser, L.C., 1967, Crustal structure between the Nevada test site and Boise, Idaho, from seismic-refraction measurements, Geophysical Monograph Series, v. 10, p. 391-419.

Hughes, S.S., Smith, R.P., Hackett, W.R., and Anderson, S.R., 1999, Mafic volcanism and environmental geology of the eastern Snake River Plain, Idaho, in Hughes, S.S., and Thackray, G.D., eds., Guidebook to the Geology of Eastern Idaho, Idaho Museum of Natural History, p.143-168.

Humphreys, E.D., Dueker, K.G., Schutt, D.L., and Smith, R.B., 2000, Beneath Yellowstone: Evaluating plume and nonplume models using teleseismic images of the upper mantle, *GSA Today*, *10*(12), p. 1-7.

Hyndman, D.W., 1983, The Idaho Batholith and associated plutons, Idaho and Western Montana, in Roddick, J. A., editor, Circum-Pacific Plutonic Terranes, GSA Memoir 159, p. 213-240.

Langston, C.A., and Hammer, J.K., 2001, The vertical component P-wave receiver function: BSSA, 91(6), p. 1805-1819.

Leeman, W.P., Annen, C., and Dufek, J., 2008, Snake River Plain–Yellowstone silicic volcanism: implications for magma genesis and magma fluxes, Geological Society, London, Special Publications, 304(1), p. 235-259.

Liberty, L., 1998, Seismic reflection imaging of a geothermal aquifer in an urban setting, Geophysics, 63(4), p. 1285-1294.

Ligorría, J.P., and Ammon, C.J., 1999, Iterative deconvolution and receiver-function estimation, Bulletin of the Seismological Society of America, 89(5), p.1395-1400.

Lipman, P.W., Prostka, H.J., and Christiansen, R.L., 1971, Evolving subduction zones in the western United States, as interpreted from igneous rocks, Science, v. 174 no. 4011, p.821-825.

Mabey, D.R., 1982, Geophysics and tectonics of the Snake River Plain, Idaho, in Bonnichsen, B., and Breckenridge, R.M., eds., Cenozoic Geology of Idaho: Idaho Geological Survey Bulletin 26, p. 139-154.

Malde, H.E., 1991, Quaternary geology and structural history of the Snake River Plain, Idaho and Oregon, in Morrison, R.B., ed., Quaternary Nonglacial Geology, Conterminous U.S.: Geology of North America, Geological Society of America, v. K-2, p. 251-280.

McCurry, M., Bonnichsen, B., White, C., Godchaux, M.M., and Hughes, S.S., 1997, Bimodal basalt-rhyolite magmatism in the central and western Snake River Plain, Idaho and Oregon, in Link, P.K. and Kowallis, B.J., eds., Proterozoic to Recent Stratigraphy, Tectonics, and Volcanology, Utah, Nevada, Southern Idaho and Central Mexico: Brigham Young University Geology Studies, v. 42, pt. 1, p. 381-422.

McCurry, M., and Rodgers, D.W., 2009, Mass transfer along the Yellowstone hotspot track I: Petrologic constraints on the volume of mantle-derived magma, Journal of Volcanology and Geothermal Research, 188(1), p. 86-98.

McQuarrie, N., and Rodgers, D.W., 1998, Subsidence of a volcanic basin by flexure and lower crustal flow: the eastern Snake River Plain. Tectonics 17 (2), p. 203–220.

Parsons, T., Thompson, G.A., and Smith, R.P. , 1998, More than one way to stretch: a tectonic model for extension along the plume track of the Yellowstone hotspot and adjacent Basin and Range Province, Tectonics, 17(2), p. 221-234.

Pierce, K.L., and Morgan, L.A., 1990, The track of the Yellowstone hot spot: volcanism, faulting, and uplift, in link, P. K., Kuntz, M. A., and Platt, L. B., eds., Regional Geology of Eastern Idaho and Western Wyoming: GSA Memoir v. 179, p. 1-53.

Pierce, K.L., Morgan, L.A., Saltus, R.W., 2002, Yellowstone plume head: postulated tectonic relations to the Vancouver slab, continental boundaries, and climate. In: Bonnichsen, Bill, White, C.M., McCurry, Michael (Eds.), Tectonic and Magmatic Evolution of the Snake River Plain Volcanic Province. Idaho Geological Survey Bulletin, vol. 30, p. 5–33.

Prodehl, C., 1970, Seismic refraction study of crustal structure in the western United States, Geological Society of America Bulletin, 81(9), p. 2629-2646.

Prodehl, C., 1979, Crustal structure of the Western United States: USGS Professional Paper 1034, p. 74.

Rodgers, D.W., Ore, H.T., Bobo, R.T., McQuarrie, N., and Zentner, N., 2002, Extension and subsidence of the Eastern Snake River Plain, Idaho, in Bonnichsen, B., White, C.M., and McCurry, M., eds, Tectonic and Magmatic Evolution of the Snake River Plain Volcanic Province: Idaho Geological Survey Bulletin, 30, p. 121-155.

Rumpfhuber, E.M., Keller, G.R., Sandvol, E., Velasco, A.A., and Wilson, D.C., 2009, Rocky Mountain evolution: Tying Continental Dynamics of the Rocky Mountains and Deep Probe seismic experiments with receiver functions, Journal of Geophysical Research: Solid Earth (1978–2012), 114(B8), B08301.

Schmandt, B., and Humphreys, E., 2011, Seismically imaged relict slab from the 55 Ma Siletzia accretion to the northwest United States, Geology, 39(2), p. 175-178.

Shen, W., Ritzwoller, M.H., and Schulte-Pelkum, V., 2013, A 3D model of the crust and uppermost mantle beneath the Central and Western US by joint inversion of receiver functions and surface wave dispersion, Journal of Geophysical Research, Solid Earth, v. 118 (1), p. 262-276.

Shervais, J.W., Kauffman, J.D., Gillerman, V.S., Othberg, K.L., Vetter, S.K., Hobson, V.R., Zarnetske, M., Cooke, M.F., Mathews, S.H., and Hanan, B.B., 2005, Basaltic volcanism of the Central and Western Snake River Plain: A guide to field relations between Twin Falls and Mountain Home, Idaho, Interior Western United States: GSA Field Guide, 6, 27 p.

Shervais, J.W., Vetter, S.K., and Hanan, B.B., 2006, Layered mafic sill complex beneath the Eastern Snake River Plain: Evidence from cyclic geochemical variations in basalt, Geology, 34(5), p. 365-368.

Silva, J.B., 1986, Reduction to the pole as an inverse problem and its application to low-latitude anomalies, Geophysics, 51(2), p. 369-382.

Smith, R.B., Schilly, M.M., Braile, L.W., Ansorge, J., Lehman, J.L., Baker, M.R., Prodehl, C., Healy, J.H., Mueller, S., and Greensfelder, R.W.,1982, The 1978 Yellowstone-Eastern Snake River Plain seismic profiling experiment: Crustal

structure of the Yellowstone Region and experiment design, Journal of Geophysical Research: Solid Earth (1978–2012), 87(B4), p. 2583-2596.

Smith, R.B., Braile, L.W., 1994, The Yellowstone hot spot, Journal of Volcanology and Geothermal Research, 61, p. 121–187.

Sparlin, M.A., Braile, L.W., and Smith, R.B., 1982, Crustal structure of the eastern Snake River Plain determined from ray trace modeling of seismic refraction data. Journal of Geophysical Research: Solid Earth (1978–2012), 87(B4), p. 2619-2633.

Thompson, G.A., Catchings, R., Goodwin, E., Holbrook, S., Jarchow, C., Mann, C., McCarthy, J., and Okaya, D., 1989, Geophysics of the western Basin and Range province in Pakiser, L.C., and Mooney W.D, eds., Geophysical framework of the continental United States: Geological Society of America Memoir 172.

Verduzco, B., Fairhead, J.D., Green, C.M., and MacKenzie, C., 2004, New insights into magnetic derivatives for structural mapping, The Leading Edge, 23(2), p. 116-119.

Wagner, L., Forsyth, D.W., Fouch, M.J., and James, D.E., 2010., Detailed three-dimensional shear wave velocity structure of the northwestern United States from Rayleigh wave tomography, Earth and Planetary Science Letters, 299(3), p. 273-284.

Wood, S.H., 1994, Seismic expression and geological significance of a lacustrine delta in Neogene deposits of the western Snake River Plain, Idaho. AAPG bulletin, 78(1), p. 102-121.

Wood, S.H., and Clemens, D.M., 2002, Geologic and tectonic history of the western Snake River Plain, Idaho and Oregon, Tectonic and Magmatic Evolution of the Snake River Plain Volcanic Province: Idaho Geological Survey Bulletin, v. 30, p. 69-103.

Conclusions

This dissertation showed that the integrated geophysical methods are capable of identifying various geological features and their possible tectonic evolution. Integrated interpretation has been established as a powerful tool to solve geological problems regardless of their scale and tectonic setting.

3D seismic interpretation from the Fort Worth Basin and seismic attribute analysis provided a high-resolution image of the basement structure in a small area. The gravity and magnetic maps and models in the area provided information in the regional context. Euler deconvolution results were useful to validate the seismic interpretation. With my integrated approach, some of the normal and reverse faults that cut across the Paleozoic sequence were interpreted. The presence of a pop-up block and the possible Reidel shear zones implied complex tectonic deformation in the southeast Fort Worth Basin. Alignment of karst and collapse features with the mapped faults indicates that the deep-seated faults and the collapse features are associated with reservoirs in the Ellenburger Group, Barnett Shale, and the Marble Falls Limestone.

I optimized the seismic data by using 2D seismic lines to generate a 3D seismic tomographic model of upper crustal structure in the Harney Basin. The 2D line geometry, the distribution of sources, and their pairing with the off-line receivers created multiple fan shots for each source. This approach helped to scan the upper crust several times for most of the basin and optimized 3D tomographic results. Two major calderas in the basin were identified using seismic, gravity, and magnetic data. Gravity and magnetic maps, gravity models, and magnetic profiles across the Harney Basin

helped to interpret major structural components in the area. The integrated geophysical approach helped to image the detailed upper crustal features of the Harney Basin area up to a depth of ~8 km.

The gravity and magnetic methods were main tools used to study the subsurface features of the Western Snake River Plain. Various filtered maps, gravity models and profiles were helpful in identifying major tectonic units in the area. The integration of these results with interpreted well logs, shallow reflection seismic, deep refraction seismic, and receiver function results helped to interpret the tectonic evolution of the Western Snake River Plain. The differences and similarities between the Eastern and Western Snake River plains were also analyzed successfully.

Thus, integration of geophysical techniques has produced useful and insightful results in these study areas. Even though one geophysical method may produce good results to some extent, one should consider using various available databases and integrate the results in order to properly address geological problems.